8-2022

Probing the Equation of State of Neutron Stars With Heavy Ion Collisions

Om Bhadra Khanal
Western Michigan University

PROBING THE EQUATION OF STATE OF NEUTRON STARS WITH HEAVY ION COLLISIONS

Om Bhadra Khanal, Ph.D.

Western Michigan University, 2022

The equation of state (EOS) is a fundamental property of nuclear matter, important for studying the structure of systems as diverse as the atomic nucleus and the neutron star. Nuclear reactions, especially heavy-ion collisions in the laboratories, can produce the nuclear matter similar to those contained in neutron stars. The density and the momentum dependence of the EOS of asymmetric nuclear matter, especially the symmetry energy term, is widely unconstrained. Finding appropriate constrains, especially at higher densities of the nuclear matter, requires the development of new devices, new experimental measurements as well as advances in theoretical understanding of nuclear collisions and neutron stars.

The main goal of the study's experiment was to further constrain the density and the momentum dependence of the symmetry energy by looking at various observables like neutron to proton ratios, particle flow and the two-particle correlations in $^{58,64}Ni +^{40,48} Ca$ collisions at E/A=56 MeV/u and 140 MeV/u. That experiment was performed at the National Superconducting Cyclotron Laboratory at Michigan State University. Measuring neutrons was an important goal of that experiment and it was done using the Large Area Neutron Array at NSCL. However, that detector by itself cannot identify neutrons from charged particles. Thus, our group at WMU constructed a charged particle detector that was placed in front of LANA that was used to veto the charged particles hitting

LANA. My research involved building, testing and commissioning of that charged particle detector, called WMU Veto Wall.

In this study I focus mostly on commissioning and calibrating of the WMU Veto Wall. I also demonstrate how our detector improves the neutron identification in LANA. Furthermore, I construct charged particles spectra from the Veto Wall and used them to construct pseudo-neutrons which are like real neutrons.

PROBING THE EQUATION OF STATE OF NEUTRON STARS WITH HEAVY ION COLLISIONS

by

Om Bhadra Khanal

A dissertation submitted to the Graduate College
in partial fulfillment of the requirements
for the degree of Doctor of Philosophy
Physics
Western Michigan University
August 2022

Doctoral Committee:

Zbigniew Chajecki, Ph.D., Chair
Michael A Famiano, Ph.D.
Elena Litvinova, Ph.D.
Alfredo Estrade Vaz, Ph.D.

ACKNOWLEDGMENTS

Above all, I would like to express my sincere gratitude to my supervisor Professor Zbigniew Chajecki for letting me do research with him and also express my heartfelt thanks to him for his guidance, encouragement and continuous support during this research journey. His enthusiasm for research offered challenging opportunities to expand my knowledge and interest.

I would like to acknowledge my research committee members Professor Michael Famiano, Professor Elena Litvinova, Professor Alfredo Estrade Vaz for their valuable comments and suggestions. My special thanks to my current and former research group members Jaclyn Brett, Justin Swaim, Cordero Soto, Jacob Boza for their help in building the Veto Wall. I want to recognized my colleague Chi Kin Tam for his valuable discussions and help with the data analysis.

I am indebted to our collaborators from NSCL−HiRA research group. I would like to express my deep appreciation to Professor ManYee Betty Tsang and Professor William Lynch for sharing their knowledge during my thesis experiment and data analysis. Special thanks to the HiRA group members Kyle Brown, Daniele Dell'Aquila, Sean Sweany, Kuan Zhu, Tommy Tsang, Chi-En Teh for their help during this journey.

I want to thank my fellow graduate students from Physics department for their helpful cooperation and assistance. I would like to express my gratitude to all faculty members of

Physics Department at WMU for their help and encouragements throughout my graduate study.

Finally, I want to thank my family members for their unconditional support all throughout my life and academic career; special words of appreciation to my parents, my sisters, my wife Rachana Poudel Khanal and my son Aarav Bhadra Khanal for their encouragement, endless support and contribution in every aspect along the years. This dissertation is dedicated to them.

Om Bhadra Khanal

TABLE OF CONTENTS

List of Tables

List of Figures

Chapter 1

Introduction

1.1 Neutron Stars

A process of Hydrogen burning out to Helium emitting radiation occurs in all stars. In further extension, Helium burns to Carbon, then to Oxygen, to Silicon and finally ends up in Iron before undergoing Supernova explosion. The Supernova explosions are caused by the core collapse of the participating stars. In a binary system of two closely orbiting stars, when one star exhausts all of its hydrogen it collapses into a white dwarf through the red giant stage. The second star becoming a red giant is accredited by a white dwarf. When the mass of such a white dwarf reaches the Chandrasekhar limit [1], its core collapses and star explodes. This is type I supernova explosion. In Type II supernova explosion, if the mass of star is greater than 20 times the solar mass, black holes are formed. If this mass is in the range of 8-20 times solar mass neutron stars are formed. During the explosion of stars to neutron stars, energy is released in the form of neutrinos. A neutron star is mostly made of neutrons. As one gets inside the neutron star, the density of nuclear matter increases significantly, reaching densities exceeding 2-3 times of saturation densities. The mass of neutron star lies within the limit of 0.1 times solar mass to maximum 2 times solar mass, the upper limit being uncertain due to the lack of knowledge of properties of nuclear matter at high densities. The radius of neutron

star is about 10 km while acceleration due to gravity is about 10^{11} times that of earth [2].

In 1967 at the Mullard Radio Astronomy Observatory, unusual signals were detected by a large radio telescope. These signals were recorded as series of pulses coming from the source within the galaxy. The detection of pulsars in 1967 led to the discovery of neutron star [3]. Pulsars take energy from the rotational kinetic energy of neutron star and gravitational binding energy. During core collapse process, the gravitational binding energy is converted to rotational kinetic energy releasing pulsars and forming neutron stars [2]. Figure 1.1 below shows the anatomy of neutron star. The goal of this work is to understand the Physics of neutron stars. For this an appropriate model is chosen which was Equation of State (EoS).

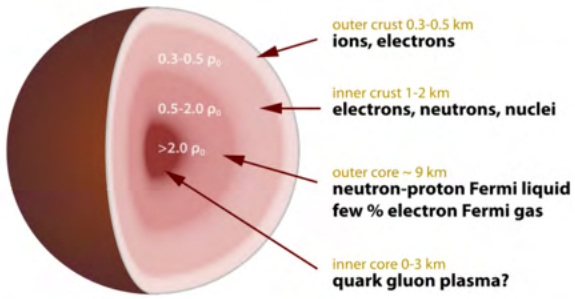

Figure 1.1: Cross section of neutron star showing density of respective crusts and cores [4].

1.2 Equation of State

Equation of State is a model that is used to describe the properties of different physical systems. We all are familiar with Boyle's law and Charles's law of gases which describe the relation between pressure, volume and temperature. These are the simplest examples of Equation of State. In general, if we know the Equation of State and its dependence on state variables such as pressure and temperature then we can determine what is going to happen to the system if one (or more) state variable changes. Thus, knowing the Equation of State of any system is essential to understand the physics of it. A Star is a complex heavenly body. When moving towards stellar region, Equation of State is used to

unfold the stellar properties. Of course, we need more parameters such as energy, density, isospin in Equation of State to study stellar properties so the EoS becomes more complex. To understand the equation of state of nuclear matter, we need to use theoretical models and compare them to the experimental data.

Several models were developed to study the shape and properties of a nucleus. Those models are categorized based on interaction between nucleons. Fermi gas model and optical model are based on non interaction between nucleons where nucleons are free to move inside nuclear radius. Liquid drop model and shell model are based on interactions between the nucleons where each nucleon interacts with neighboring one and does not move beyond the radius of a nucleus [5].

The Liquid drop model describes nucleus as a drop of nuclear fluid (nucleons) which is incompressible in nature. This model was first proposed by George Gamow. Niels Bohr and John Archibald Wheeler further developed the model. The mathematical formulation for calculating binding energy was first given by Carl Friedrich von Weizsäcker using liquid drop model [6] which is widely known as semi empirical mass formula or Weizsäcker formula. For a nucleus with Z protons, N neutrons and A(=N+Z) mass number, mass defect formula is written as

$$M_{A,Z}c^2 = Zm_pc^2 + (A-Z)m_nc^2 - B_{A,Z} \tag{1.1}$$

Here, m_p and m_n are masses of proton and neutron respectively and $B_{A,Z}$ is the binding energy of nucleus which refers to the minimum energy that is required to disassemble a nucleus into its constituent protons and neutrons. In other words, it is the energy required to bind nucleons inside a nucleus. According to semi empirical mass formula, this binding energy is calculated by the following formula:

$$B_{A,Z} = a_vA - a_sA^{\frac{2}{3}} - a_c\frac{Z^2}{A^{\frac{1}{3}}} - a_a\frac{(N-Z)^2}{A} + \delta(A,Z) \tag{1.2}$$

The first term a_v is the volume term. Each nucleon attracts the neighboring nucleons

by a strong nuclear force so the binding energy is proportional to A. However, for some nucleons close to the surface, the number of neighboring nucleons is decreased so the binding energy will decrease by an amount proportional to the number of nucleons on the surface. This is explained by the second term of the above equation which is a surface term. The surface term mechanism is similar to the surface tension in liquid. If a volume is proportional to A and R^3,then $A \propto R^3$ which implies $R \propto A^{(\frac{1}{3})}$. The Surface area is quadratic in R so surface term is proportional to $A^{\frac{2}{3}}$. This term is a correction to the volume term. Since protons are positively charged particles, there is an electrostatic repulsion between the protons which decreases the binding energy. For a pair of protons, the interaction energy due to Coulomb potential is $\frac{Z^2}{R}$, so binding energy changes by an amount of -$\frac{Z^2}{A^{\frac{1}{3}}}$. The next term is an asymmetry term which is quantum in nature. According to Pauli's Exclusion Principle, two identical fermions can not have exactly the same quantum state. Consider we have equal number of protons and neutrons at a given energy level. For a nucleus, energy will be minimum when A = Z. If a neutron gets converted to proton via β decay, the number of protons will increase and number of neutrons will decrease $|N - Z| = 2$ and the energy level of proton is increased by $1\Delta E$. If more neutrons get converted to protons then energy will increase. This increase in energy decreases the binding energy in the order of -$\frac{(N-Z)^2}{A}$. The last term represents the pairing effect is also quantum mechanical in origin. If the number of protons(or neutrons) spinning up is equal to the number of protons (or neutrons) spinning down, nucleus will have lower energy. Even number of protons and neutrons favors stability. Different coefficients of above equation such as a_v, a_s, a_c, a_a can be obtained by fitting to binding energy of various nucleons [7].

Attempts have been made to determine the Equation of State from binding energy. Binding energy consists of volume, surface and coulomb terms which are strongly correlated. It was a major con in determining EoS from binding energy. Nuclear shell and deformation effects are also large. Moreover, different fit parameters are roughly equivalent which give different conclusions on surface symmetry energy. Symmetry energy can

be expressed from the binding energy as shown in [8].

Using equation 1.2, the energy per nucleon can be written as,

$$\epsilon(\delta) = -\frac{B(Z,A)}{A} = -a_v + a_a\delta^2 \tag{1.3}$$

At the vicinity of number of nucleons and volume is infinity but the ratio is fixed at saturation density when neglecting the Coulomb interaction. Since the liquid drop is not in-compressible, a semi-empirical mass formula can not relate the density fluctuation effects on the liquid drop. The Equation of State of nuclear matter depends on the density and asymmetry apart from the temperature and the pressure [9]. Nuclear equation of state can now be written as

$$\epsilon(\rho,\delta) = \epsilon(\rho,\delta=0) + S(\rho)\delta^2, \tag{1.4}$$

where ρ is density and δ is isospin asymmetry which is given by

$$\delta = \frac{\rho_n - \rho_p}{\rho_n + \rho_p} \approx \frac{(N-Z)}{A}, \tag{1.5}$$

where ρ_n and ρ_p are the densities of neutrons and protons. Looking back at equation 1.4, the first term is the term involving an equal number of protons and neutrons which is the equation of state of the symmetric nuclear matter. The second term includes the symmetry energy, $S(\rho)$, an asymmetric term which involves neutron-proton isospin. The symmetry energy will be discussed in details in the following chapter.

1.3 Heavy-Ion Collisions

In order to understand the Equation of State of neutron stars, we must study the nuclear matter at extreme conditions that are relevant to neutron stars. In lab, we can only do this through heavy ions collisions at different densities and asymmetry. In heavy ion collision, nucleons are smashed within a small volume. While the volume of the

interacting region in heavy-ion collisions is hard to measure, we can probe the equation of state of nuclear matter through its density dependence. Density, in fact, is the quantity that drives the physics of neutron stars. A comparison of different characteristics of neutron stars with heavy ion collision is shown in Table 1.1 [10].

Table 1.1: A comparison of density, electron yield and temperature between Neutron Star and Heavy Ions at lab

	neutron star	Heavy Ions
ρ/ρ_0	0.1 to 10	0.1 to 5
Y_e	0.1	0.38 to 0.5
T(MeV)	1	4 to 50

During heavy ion collision, a participant region compresses and expands. In central collisions, colliding system disintegrates into lighter fragments. Figure 1.2 shows the process of central collision where two colliding nuclei strike head-on and disintegrate into various fragments. Head on collision occurs within the participant nucleus while shear

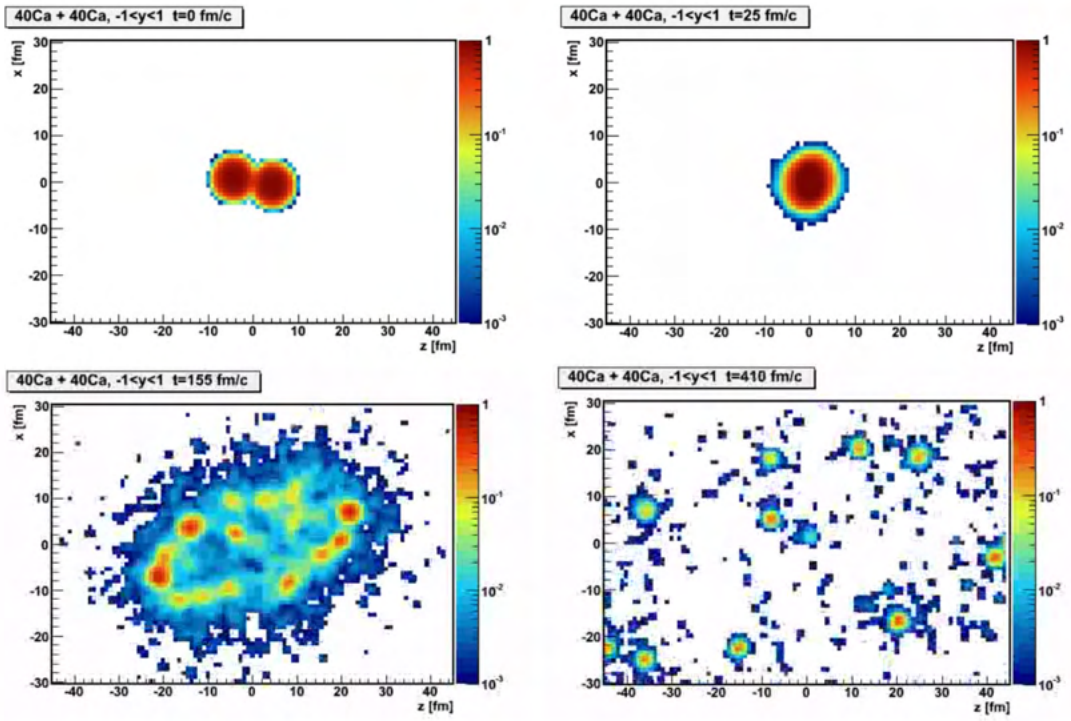

Figure 1.2: Different stages of the collision. Top left panel shows start of head on collision. Top right shows unstable nucleus formed after collision. Bottom left shows emission of immediate fragments. Bottom right shows emission of low velocity fragments [11].

off collision occurs within the spectator nucleus. Various observables from heavy ion collisions can be used to study the symmetry energy and its density and momentum dependence. They are explained in Chapter 2.

1.4 Organization

The brief introduction about neutron stars and the equation of state is presented in Chapter 1. Chapter 2 begins with the introduction to the symmetry energy. In that Chapter, I explain various obervables used to study the density dependence of symmetry energy along with the comparison to theoretical models. Those results provide motivation for the current work. Chapter 3 deals with the experimental details of our experiment. In that chapter I describe the experiment and introduce all the detectors that were used. Chapter 4 is devoted to the Veto Wall detector. That chapter also consists of the description of construction, calibrations and commissioning of the Veto Wall detector. Chapter 5 deals with the data analysis. Results, and future outlooks are explained in Chapter 6.

Chapter 2

Motivation

2.1 Symmetry Energy

Equation 1.4 represents the energy per nucleon of nuclear matter. The first term is equation of state of symmetric nuclear matter and $\delta-$ dependent second term is the symmetry energy. The Figure 2.1 shows the dependence of the energy of symmetric matter on density. It shows that energy of symmetric matter has a stable minimum at

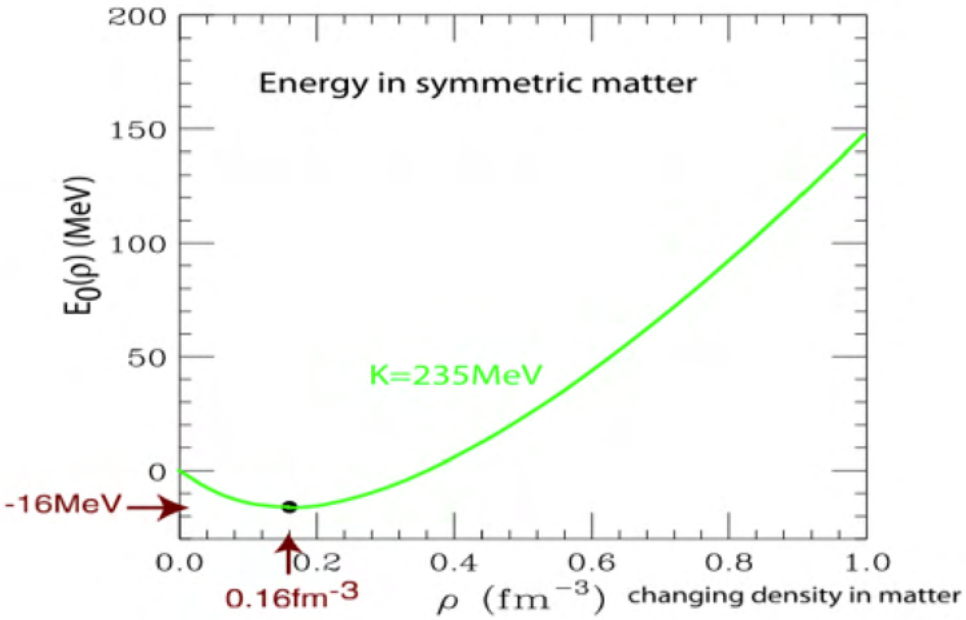

Figure 2.1: Plot showing the density dependence of energy of symmetric matter.

the saturation density. Saturation density is the density at which nucleons just start

to touch each other. At saturation density (0.16 fm^{-3}) the energy is -16 MeV. Taking symmetry energy term of equation of state,

$$(\frac{\partial^2\epsilon(\rho,\delta)}{\partial\delta^2})_{\delta=0} = 2S(\delta) \tag{2.1}$$

$$S(\delta) = \frac{1}{2}(\frac{\partial^2\epsilon(\rho,\delta)}{\partial\delta^2})_{\delta=0} \approx \epsilon(\rho,\delta=1) - \epsilon(\rho,\delta=0) \tag{2.2}$$

This equation shows that symmetry energy is constrained by density dependence for asymmetric nuclear matter. This density dependence of symmetry energy is not well known at larger densities which lacks understanding of the properties of neutron stars. Taylor expansion of equation 2.2 at saturation density gives the following relation:

$$S(\delta) = S_0 + Lx + \frac{1}{2}K_{sym}x^2 \tag{2.3}$$

where x = $\frac{(\rho-\rho_0)}{3\rho}$, S_0 is symmetry energy at saturation density which is offset of equation 2.3, L is a slope of the symmetry energy and K_{sym} is a curvature at the ρ_0. The slope of the symmetry energy is

$$L = 3\rho_0(\frac{\partial S}{\partial\rho})_{\rho_0} \tag{2.4}$$

This slope is related to the symmetry pressure (P_0) at the saturation density as,

$$P_0 = \frac{1}{3}\rho_0 L \tag{2.5}$$

There is no contribution of the symmetric matter energy towards the symmetry pressure [12, 13]. The role of the symmetry pressure is to hold star against gravitational force whereas symmetry energy defines internal structure of neutron stars [14, 15, 16, 17, 18]. Nuclear symmetry energy plays an important role in the density range of 0.1 to 10 times the saturation density, affects the birth of neutron stars and supernova neutrinos [19], in evolution of core collapse supernova [20], astrophysical r-process nucleosynthesis [21, 22, 23, 24], the gravitational wave frequency [25, 26], and gamma-ray bursts

in neutron star mergers [27, 28, 29].

2.2 Theoretical Models

Transport models are widely used to simulate heavy-ion collisions so that experimental constraints on the symmetry energy can be compared with constraints from the simulations. Many versions of transport models are used to generate constraints on the symmetry energy, for example: AMD+JAM [30, 31, 32], IQMD-BNU [33, 34, 35], TuQMD [36, 37], UrQMD [38, 39], pBUU [40, 41], SMASH [42], χBUU [43]. AMD+JAM, IQMD-BNU, TuQMD and UrQMD models are based on quantum molecular dynamics while pBUU, SMASH and χBUU models are based on Boltzmann-Uehling-Ulhenbeck equation. Boltzmann approach is based on an evolution of a single particle phase space density. These models are compared with each other in these references [44, 45, 46].

Molecular dynamics models evolved from classical molecular dynamics and finite size wave packets are collided to create dissipation and fluctuations which are governed by the width of the particles. If anti−symmetrization is not included in the collision of wave packets, the model is called Quantum Molecular Dynamics (QMD) and if anti−symmetrization is included in the collision of wave packets, the model is called Anti−symmetrization Molecular Dynamics (AMD). Amount of fluctuations impacts the evolution of phase transition to form light clusters or fragments. In molecular dynamics model, when wave packets are at the same phase space point, clusters are formed. Classical phase space determines the probability of forming the clusters [13]. The effect of light clusters as new degree of freedom should not be considered while parametrizing symmetry energy. Formation of cluster can change reaction dynamics [47, 48, 49]. Transport codes require mean field, elastic and inelastic in− medium cross sections as inputs in a set of complex system of non−linear differential equations [13]. In AMD, single particle wave functions are the wave packets which can assemble and disassemble nucleons. Time independent AMD describes the structure of neutron rich isotopes such as Be, C, F, Ne and

Mg. Time dependent AMD describes fragmentation in heavy ion collision. AMD model describes clusters and mean field and can be applied to static and dynamic problems. More details on AMD model can be found here [50].

2.3 Effective Mass

In collisions, the motion of nucleon is influenced by the potentials from all other nucleons. This influencing potential is termed as mean field which introduces the momentum dependence. To study the motion of nucleons through momentum-dependent mean field, Brueckner introduced nucleon effective mass [51]. Neutrons and protons feel different momentum dependent potential and act with different effective mass m_n* (neutron effective mass) and m_p* (proton effective mass). This different effective mass of neutron and proton gives effective mass splitting between nucleons. If $m_n* < m_p*$, high momentum neutrons experience more repulsive potential than high momentum protons which increases the emission of high momentum neutrons. If $m_n* > m_p*$, this decrease the emission of high momentum neutrons. High momentum region has greater sensitivity to effective mass.

2.4 Study of Symmetry Energy with Different Observable

As discussed in previous chapter, various observables in heavy ions collisions can be sensitive to symmetry energy. Such observables are neutron-proton spectra and flow, isospin diffusion, spectral pion ratio, correlations. Pion ratio is used in high density region due to an energy threshold in pion production. Isospin diffusion is used in low density region, while neutron-proton spectra and flow are used in any densities. Each of these observables are used to constraint symmetry energy. In this section I will go through different observables that shows sensitivity to the symmetry energy and compare the

experimental results to the predictions from different transport models.

2.4.1 Pion Production

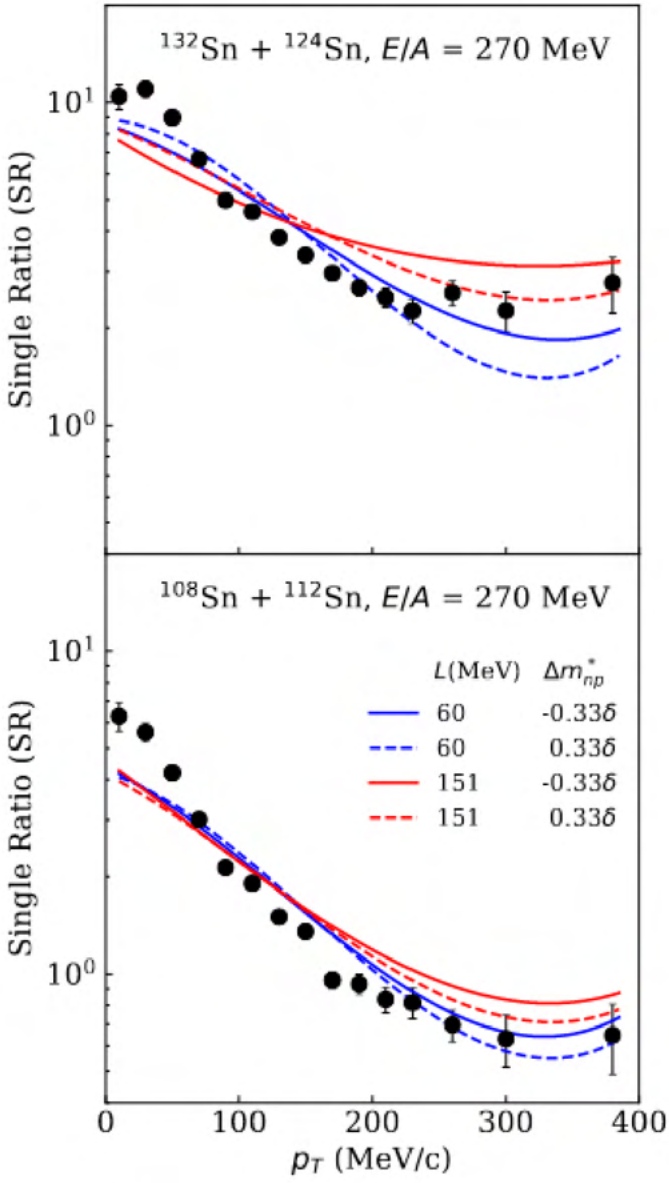

Figure 2.2: Single ratio of pions for asymmetric system (top) and symmetric system (bottom). Red and blue curves are calculations from dcqmd for different L and $\Delta m^*_{n,p}$ [52].

In order to constrain symmetry energy through pions produced during heavy ion collisions, SπRIT experiment was performed in 2016. That experiment used a special detector named SπRIT TPC , (SAMURAI Pion-Reconstruction and Ion-Tracker (SπRIT) Time

Projection Chamber (TPC)) [53] and charged particles including pions were detected to study the symmetry energy.

Figure 2.2 shows the ratio of the yield of pions π^-/π^+ versus the transverse momentum (momentum perpendicular to the beam line), p_T, for different systems. Theoretical calculations were done at different values of L and effective mass, $\Delta m^*{}_{n,p}$. At $p_T < 50$ MeV/c, theoretical calculations underpredict the data while at 150 MeV/c they overpredict the data. The rise of the single ratio at low value of P_T is due to the opposite coulomb forces experienced by π^+ and π^-. In the figure we can see that the neutron rich system is more sensitive to the effective mass at high p_T. This difference in sensitivity is due to the Coulomb and pion potential. Since, the single ratio has some sensitivity to the Coulomb interaction, we use double ratio, which is the ratio of single ratios from neutron−rich system to proton−rich system, to increase the sensitivity as the effect due to coulomb cancels out in double ratio. Figure 2.3 shows double ratio of pions yield. The consistent region in this plot is L= 49 to 105 which fits the experimental data. In that work, symmetry energy at supra saturation densities (density above the saturation density) were constrained from charged pions spectra with p_T >200 MeV/c and the symmetry energy constraints were obtained as 42<L<117 MeV and 32.5<S_0<38.1 MeV [52].

2.4.2 Neutron-Proton Spectral Ratios

The emission of neutrons and protons during the collision is governed by the neutron and proton mean field potential. Neutrons have repulsive potential while protons have attractive potential. These potentials depend on nuclear force, neutron number(δ) and density (ρ). In collision of neutron-rich nuclei, both δ and ρ are correlated with mean fields of neutron and proton, which are isospin dependent. Thus, they affect the dynamics of the reaction by changing the neutron and proton spectra significantly. The effect of potential on protons and neutrons for different nuclear forces and isospin is shown in Figure 2.4 [54].The potential for neutrons and protons have opposite sign and different dependence of density as shown in Figure 2.4.

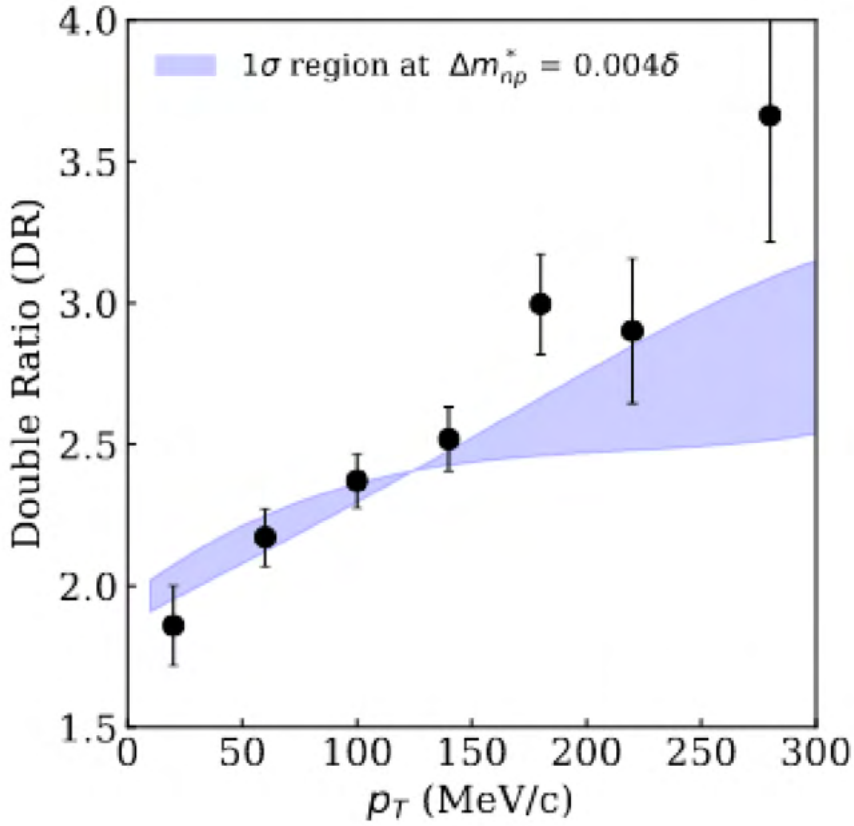

Figure 2.3: Double ratio of pions in terms of transverse momentum. Shaded region is dcqmd predictions with in 68 % confidence level with most probable values of L and $\Delta m^*{}_{n,p}$ [52].

Neutron and proton spectra are the observable of heavy-ion collisions. Those spectra are used to construct the single ratio of neutron to proton to constraint the symmetry energy at higher densities. There are some difficulties in determining neutron−proton spectral ratios. These difficulties are due to i) neutrons and protons being detected by different detectors having different efficiency ii) protons being positively charged are affected by the Coulomb potential. Such difficulties are overcome by determining the double ratio of the spectra of neutrons and protons from two different systems; one being neutron rich and the other being neutron deficient.

$$DR_{n/p} = \frac{(n/p)_{n-rich}}{(n/p)_{n-deficient}} \tag{2.6}$$

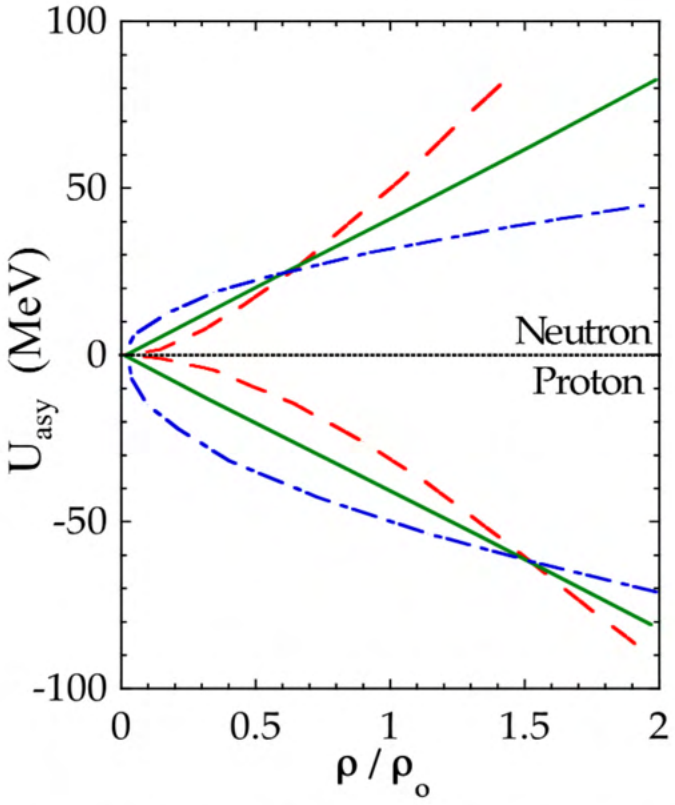

Figure 2.4: Symmetric field dependence for proton and neutron on different nuclear forces and isospin. These different patterns lines represent different force and isospin [54].

In Figure 2.5 different lines represent soft and stiff symmetry energy curves. Stiff curve suggests that the pressure increases strongly with density which makes nucleon harder to compress while soft curve suggests smaller increase in pressure with density; nucleon can be easily compressed. If the density dependence of the symmetry energy is positive at high density (for stiff curves), neutrons are expelled out of the system and if it is negative (for soft curves), symmetry energy attracts neutrons towards the system. Shaded region in Figure 2.5 represents the experimental constraints. At low density, most curves pass through the shaded region, while at high density they differ significantly. Soft curves are weakly dependent of density and stiff curves are strongly dependent of density. The density dependence of the symmetry energy can be studied by measuring the spectra of neutrons and charged particles in reference [55]. Figure 2.6 shows single and double ratios of neutrons to protons in the center of mass frame. Transport model simulations have

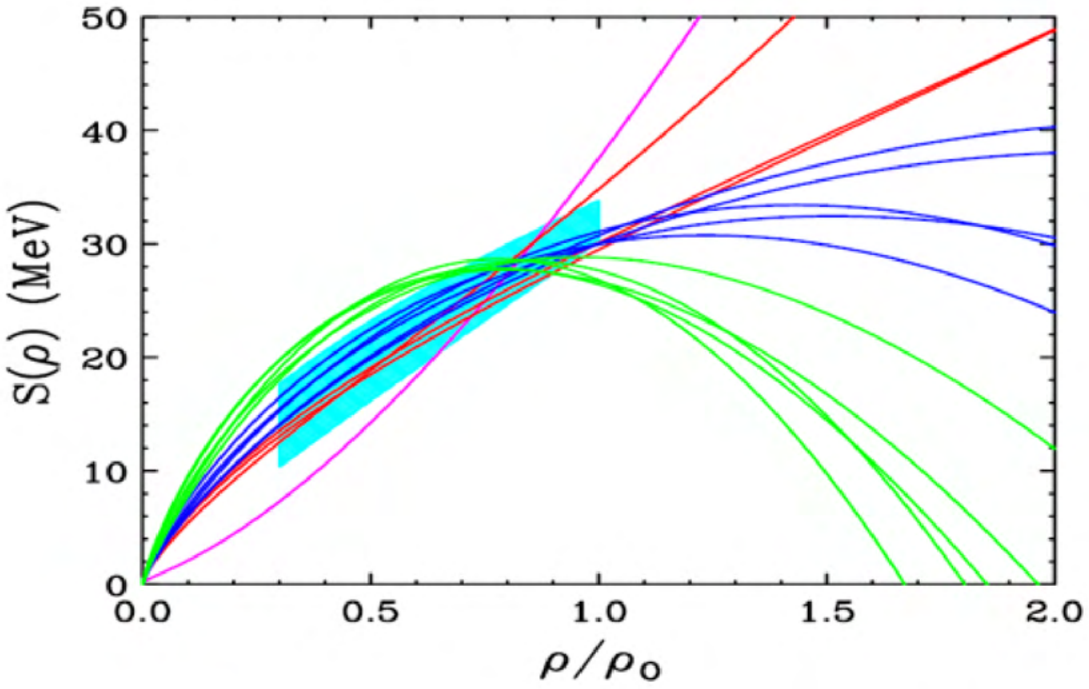

Figure 2.5: Density dependence of symmetry energy [56, 57].

difficulty reproducing the relative abundances of light isotopes produced in the collisions as the system expands and disassembles. Thus, the coalescence invariant (CI) neutron and proton spectra are determined by combining free nucleons with those bound in the light isotopes with $1 < A < 5$ [55]. In Figure 2.6 open blue circles in single ratio panels are

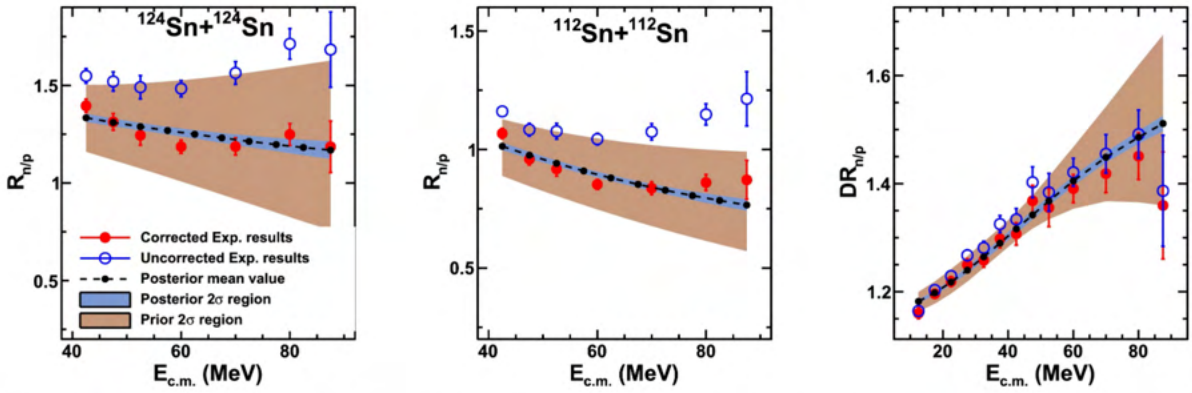

Figure 2.6: Single (left panel and middle panel) and double (right panel) ratio of neutrons to protons [58].

uncorrected ratios of CI neutron to CI protons spectra for $^{124}Sn + ^{124}Sn$ (left panel) and $^{112}Sn + ^{112}Sn$ (center panel). Solid red points represent corresponding efficiency corrected ratios. Right panel shows the double ratio of ratios shown in the left and center panel.

That figure shows that the efficiency-corrected double ratios are consistently lower than uncorrected double ratios within experimental uncertainties. The residual difference in double ratio is due to mixture of different isotopes within detection efficiency. The brown shaded area corresponds to the prior 2σ region of the 49 sets of ImQMD calculations while blue area corresponds to the posterior 2σ [58].

2.4.3 Isospin Diffusion

A peripheral heavy ion collisions with different neutron−proton asymmetry lead to drift and diffusion of neutrons and protons through low density connecting region of interacting particles [59]. Density gradients between the low density neck region and interacting projectile-target partners at saturation density drive drift while different neutron−proton asymmetries of interacting projectile-target partners drive diffusion. These partners exchange neutrons and protons to reach a uniform distribution of neutrons and protons [59, 60]. Collisions of ^{112}Sn and ^{124}Sn beam with ^{112}Sn and ^{124}Sn targets at beam energy 30 MeV/A and 50 MeV/A were studied at MSU [61]. Peripheral collisions were selected by proper gates on charged particles multiplicity with impact parameter b/b_{max} in a range of 0.8 to 1.0 using the sharp cutoff approximation [62]. Neck fragments contributions were minimized by a suitable selection of projectile rapidity which is $y/y_{beam} \geq 0.7$ where y is rapidity of the particle and y_{beam} is rapidity of the beam. The symmetric collisions ^{112}Sn on ^{112}Sn and ^{124}Sn on ^{124}Sn lack isospin difference so these collisions are used to construct diffusion free baseline values for measured and predicted observables. While the asymmetric collisions of ^{112}Sn on ^{124}Sn and ^{124}Sn on ^{112}Sn have large isospin differences needed to study the isospin diffusion. Isotopic yield $Y_j(N, Z)$ of measured particles is an experimental observable for reaction j. The ratio of isotopic yields from two systems gives $R_{21} = Y_2(N, Z)/Y_1(N, Z)$ and is defined as ,

$$R_{21}(N, Z) = C \exp(\alpha N + \beta Z), \tag{2.7}$$

where α and β are isoscaling parameters and C is an overall normalization constant [63].

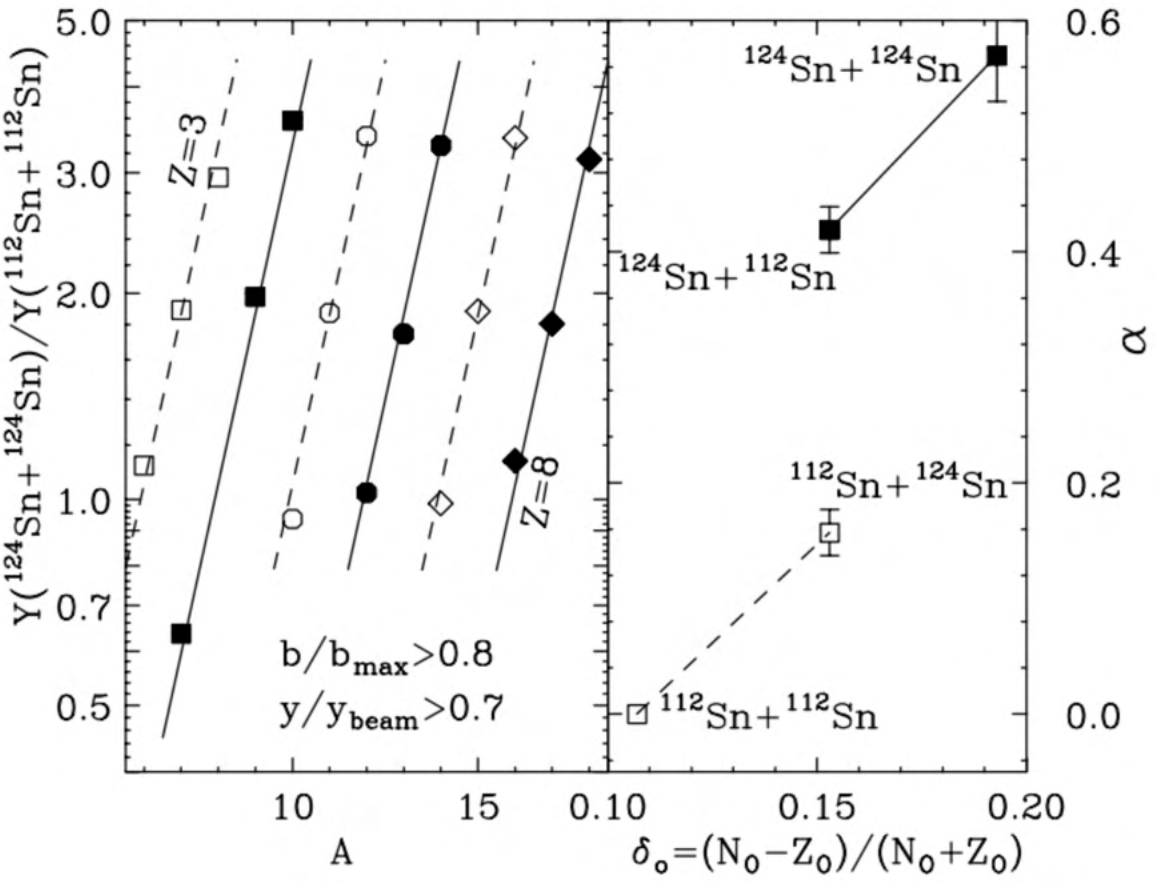

Figure 2.7: Isotropic yields for symmetric systems [64].

Left panel of Figure 2.7 shows the experimental values for $R_{21}(N,Z) = Y_{124+124}(N,Z)/Y_{112+112}(N,$ and fits with equation 2.7. The solid lines and points represent Z = 4,6,8 while dash lines and open points represent Z = 3,5,7 isotopes. Right panel shows best fit values for α as a function of $\delta_0 = (N_0 - Z_0)/(N_0 + Z_0)$, N_0 and Z_0 are total numbers of neutrons and protons. Solid points represent ^{124}Sn as projectile while open points represent ^{112}Sn as projectile. In general, isoscaling parameter α increases with overall isopin asymmetry δ_0 [64]. Isospin transport ratio R_i is defined as [65],

$$R_i = \frac{2x - x_{124+124} - x_{112+112}}{x_{124+124} - x_{112+112}} \tag{2.8}$$

x is an isospin sensitive observable. R_i is normalized to +1 for ^{124}Sn and -1 for ^{112}Sn. In

absent of isospin diffusion, the symmetric and asymmetric collision give the same preequilibrium emission from projectile. R_i removes sensitivity to preequilibrium emission by focusing on the differences in isospin observables between mixed and symmetric systems. This increases sensitivity to the diffusion. As projectile and target of asymmetric system differ in number of neutrons, neutron isoscaling parameter α is used as x in Equation 2.8 and $|R_i(\alpha)| \approx 0.5$ [64]. Figure 2.8 shows the measured and calculated values of R_i.

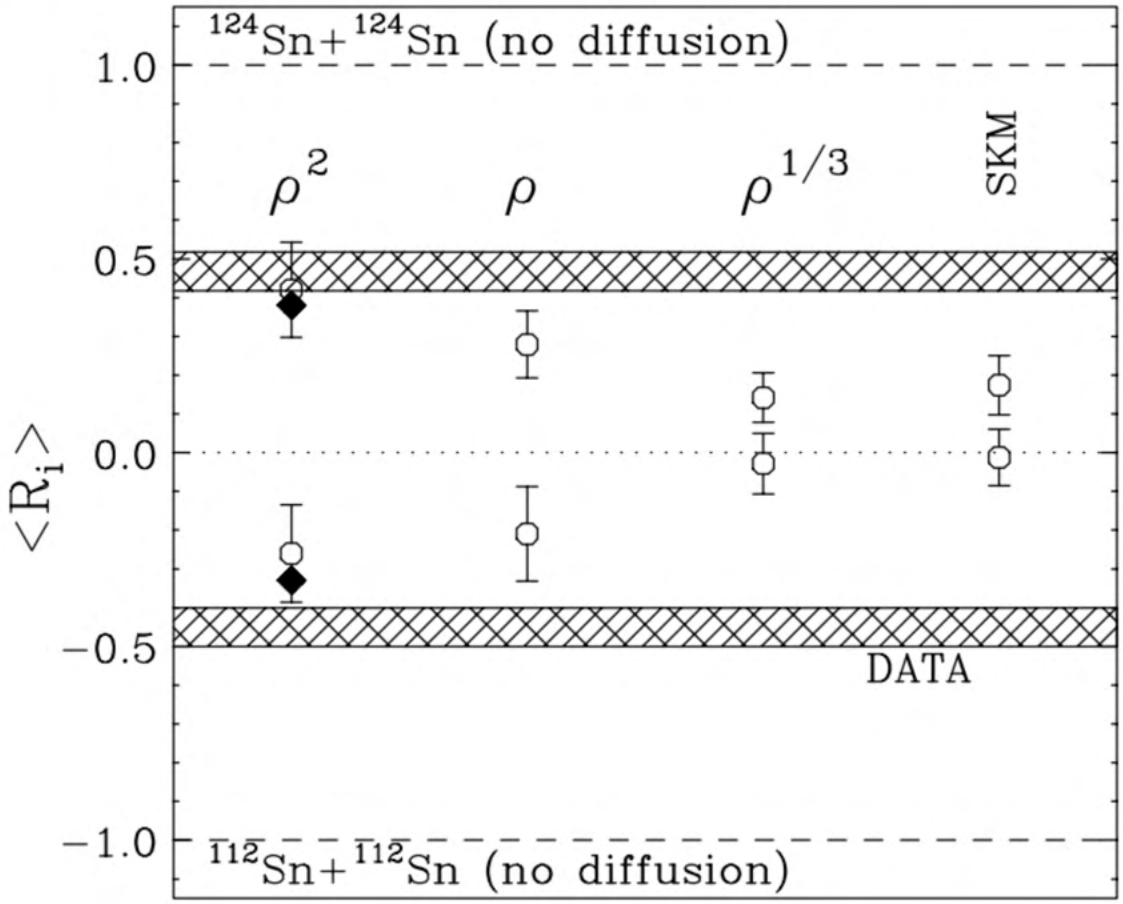

Figure 2.8: Experimental and calculated isotropic ratio at different density dependence [64].

Shaded bars represent measured values while points represent calculated values at different density dependence of symmetry energy per nucleon. Softness increases as we move from left to right. The experimental values of R_i are closer to the predicted values at $E_{sym,int}/A = C_{sym}(\rho/\rho_0)^2$. This conclusion is based on $<\delta>$ being asymptotic that is measured particles are produced after 100 fm/c [64].

2.4.4 Elliptic Flow

Nucleon elliptical flow $v_2(y, p_T)$ is another observable that can be used to study the symmetry energy.v_2 is given by the second coefficient from a Fourier expansion of the azimuthal distribution.

$$N(\phi, y, p_T) = v_0(1 + v_1 cos(\phi) + 2v_2 cos(2\phi)) \tag{2.9}$$

$$v_2 = < \frac{{p_x}^2 - {p_y}^2}{{p_T}^2} > \tag{2.10}$$

where ${p_T}^2 = \sqrt{{p_x}^2 + {p_y}^2}$ is the transverse momentum [66, 40]. Angular bracket denotes an average of all considered particles of the events. Fig. 2.9 shows the elliptic flow of

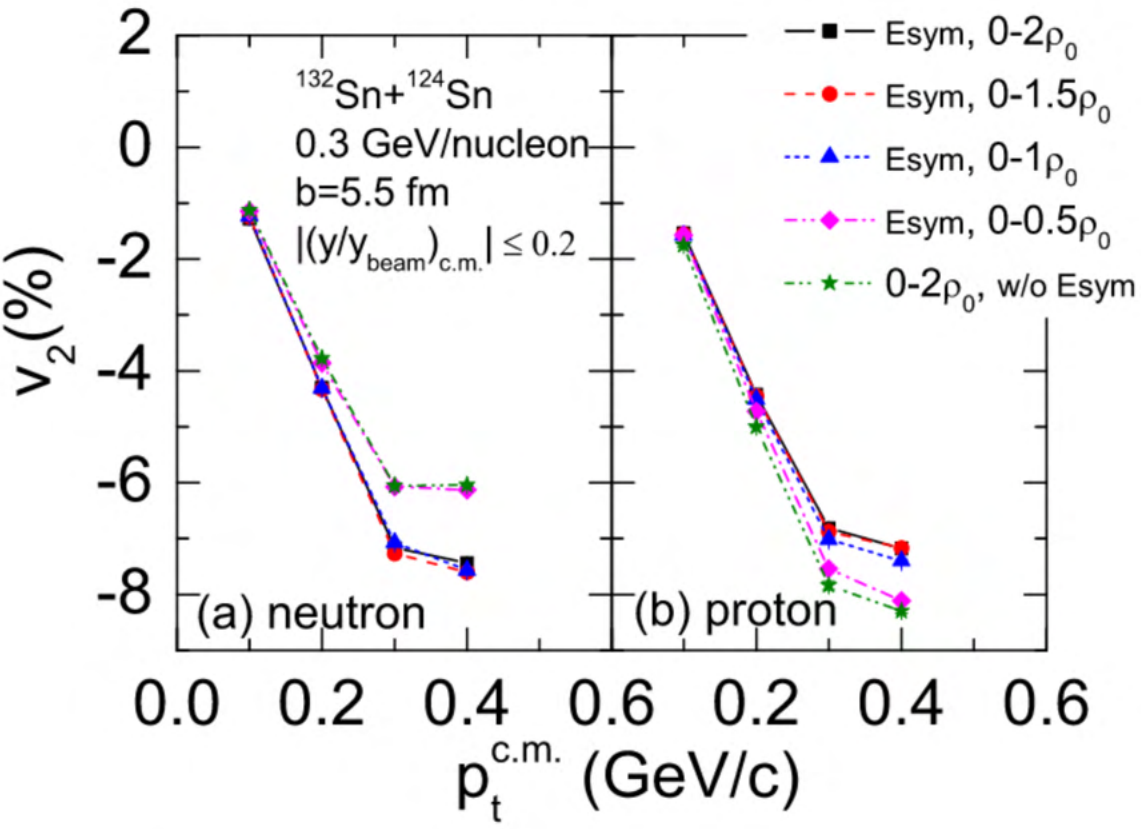

Figure 2.9: Neutron and proton elliptic flow as a function of transverse momentum at 0.3 GeV/A energy for ^{132}Sn + ^{124}Sn reactions using isospin-dependent Boltzmann-Uehling-Uhlenbeck (BUU) transport model [67].

neutrons and protons as a function of transverse momentum p_T for reaction $^{132}Sn + ^{124}Sn$ at 0.3 GeV per nucleon incident energy and 5.5 impact parameter. Fig. 2.9 shows that when symmetry energy in density regions of 0 to ρ_0, 0 to $1.5\rho_0$ and 0 to $2\rho_0$ are added for neutrons, the effect of symmetry energy is the same. Neutron elliptic flow without adding the symmetry energy has almost the same effect to the one when adding symmetry energy in the density region of 0 to $0.5\rho_0$. The effect of symmetry energy is only distinguishable in the region of $0.5\rho_0$ to $1\rho_0$. So at energy 0.3 GeV/A elliptic flow only probes the density dependence of symmetry energy in the region $0.5\rho_0$ to $1\rho_0$. Similar case with protons is shown in Figure 2.9 (b). In order to probe the symmetry energy at high density, the beam energy is increased to 0.6 GeV/A. In Figure 2.10 (a) at density

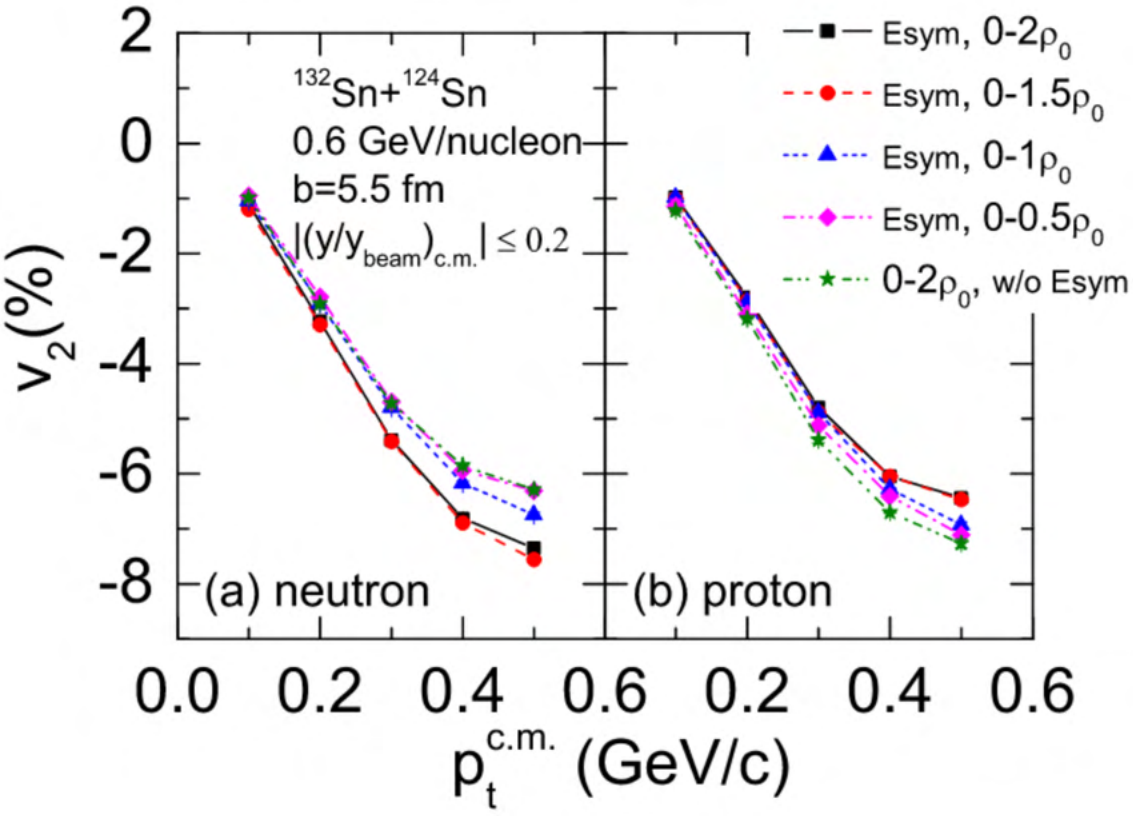

Figure 2.10: Neutron and proton elliptic flow as a function of transverse momentum at 0.6 GeV/A energy for $^{132}Sn + ^{124}Sn$ reactions using isospin-dependent Boltzmann-Uehling-Uhlenbeck (BUU) transport model [67].

region of ρ_0 to $1.5\rho_0$, effect of symmetry energy is larger for neutron elliptic flow. In the

same region, the effect of symmetry energy on proton elliptic flow is stronger as seen in Figure 2.10 (b). Neutron elliptic flow can probe symmetry energy from low density to high density regions by changing the energy of the beam [67].

2.5 Previous Experiment

In November 2009, an experiment was conducted at NSCL in order to study the density dependence of the symmetry energy with emitted neutrons and protons. The experimental details can be found in reference [68]. The objectives of the experiment were to get a single and double ratio of neutron to proton at higher degree of accuracy at different energies so that researchers can use it to constraint the isospin dependence of effective mass. Figure 2.11 shows one such ratio from from similar experiment from

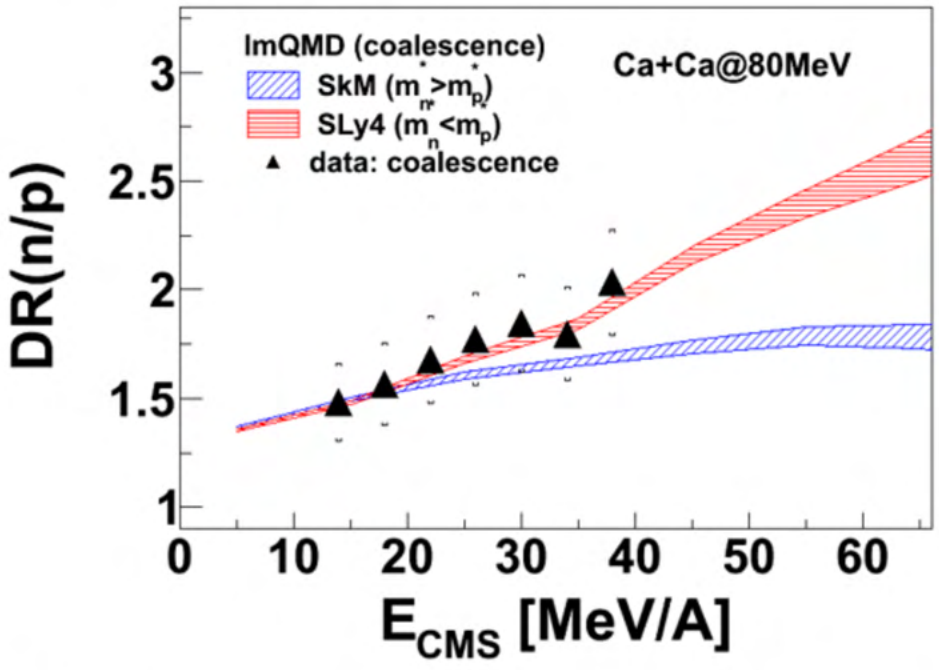

Figure 2.11: Double ratio of coalescence neutron to proton for $^{40,48}Ca + ^{40,48}Ca$ collisions at 80 MeV/u [55].

collision of Ca on Ca at 80 MeV/A. The neutrons and protons used in that double ratio were coalescence neutrons and protons. Those coalescence nucleons were obtained by breaking the lighter fragments into their constituent nucleons and adding them to free

nucleons. In Figure 2.11, black triangles are the experimental data while red and blue regions are the theoretical calculations from the ImQMD model for different effective masses. Figure 2.11 shows that within the error bars the experimental data agree with the both calculations. Also, we can see that the data are limited to 40 MeV/A in center of mass frame. This is because only tritons up to 40 MeV/A are detected in that experiment which restricted the construction of coalescence nucleons to 40 MeV/A. Similarly with the available detectors, energy of the beam and target, that experiment was able to detect protons up to the center of mass energy of 100MeV/u [55]. In order to understand the data at high energy and compare with the theoretical models, detect high energy charged particles, theoretical simulations for ^{40,48}Ca on ^{40,48}Ca at 35 MeV/A and 120 MeV/A were done [69].

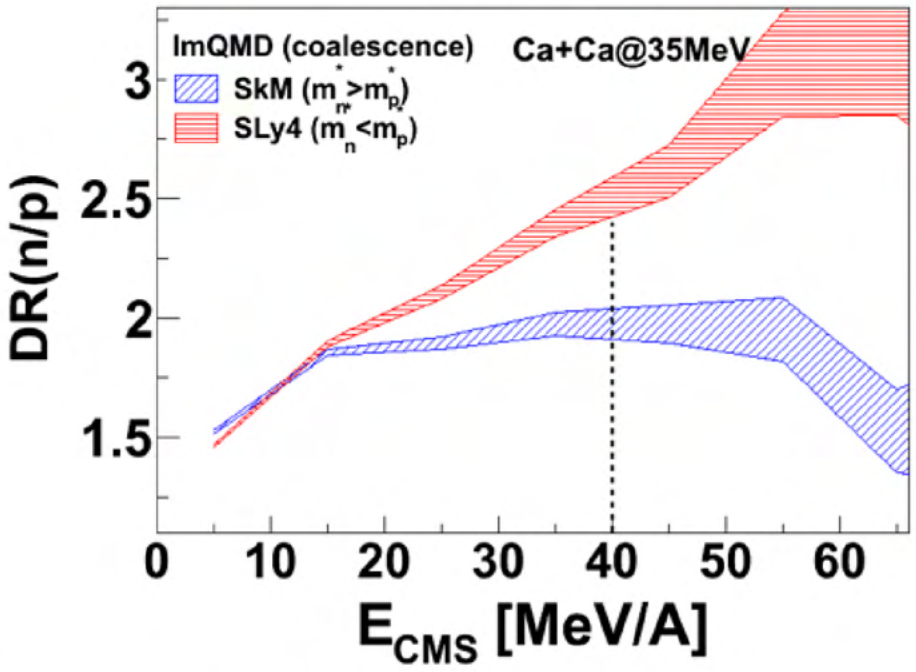

Figure 2.12: Coalescence neutron to proton double ratio from theoretical calculations using ImQMD for ^{40,48}Ca on ^{40,48}Ca at 35 MeV/A [69].

Figure 2.13 shows an effective mass splitting in between 40 MeV/A and 80 MeV/A but we lack the data to compare with theoretical simulations. So our recent experiment was planned in order to measure the data in that region. Our experiment aimed at high energy beam, different asymmetry combinations of beam−target and new and updated

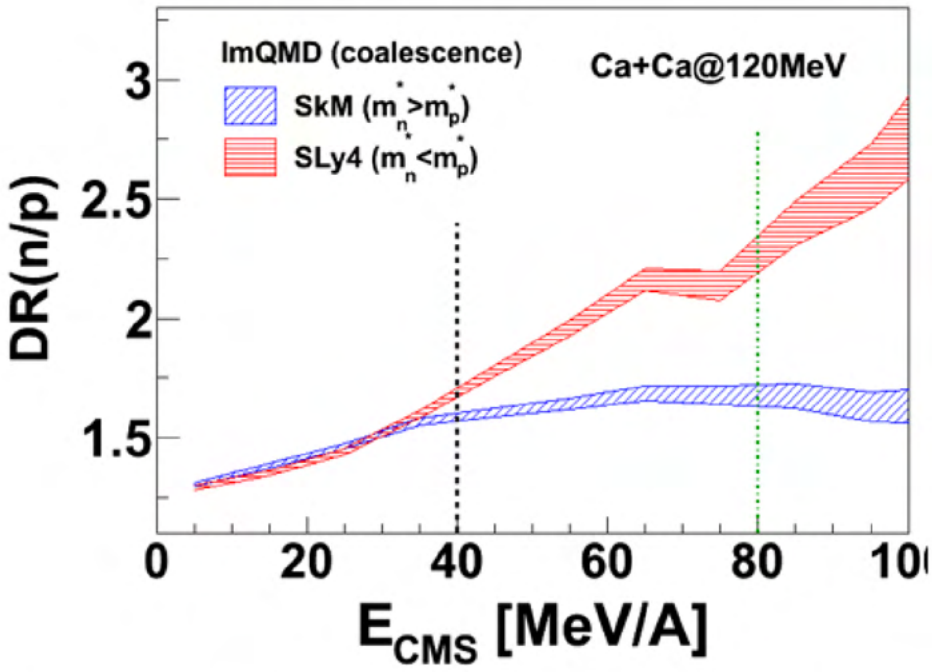

Figure 2.13: Coalescence neutron to proton double ratio from theoretical calculations using ImQMD for ^{40,48}Ca on ^{40,48}Ca at 120 MeV/A [69].

old detectors. Details about the detectors are provided in the following chapter.

Chapter 3

Experimental Details

3.1 Background

An experiment, e16042, entitled "Commissioning of the Large Charged Particle Veto Wall" was conducted in December 2017 at the National Superconductor Cyclotron Laboratory. The purpose of that experiment was to commission the charged particle Veto Wall which here will be referred as the WMU Veto Wall. It was an essential detector for experiments e14030 and e15190 at NSCL. The WMU Veto Wall was designed, constructed at WMU and installed at NSCL for the experiments described in this dissertation. The primary purpose of the WMU Veto Wall is to measure charged particles. Large Area Neutron Array (LANA) is the detector used to detect neutrons. LANA is made of organic scintillating materials. Neutron detection in the LANA relies on detection of recoiled protons produced when neutrons scatter them off scintillating materials. Thus, LANA also detects charged particles. The WMU Veto Wall was placed in front of the LANA. Charged particles signal from the WMU Veto Wall and their corresponding signals in the LANA suggest that charged particles are coming from the reaction center and we can reject such signals in neutron detector. Then we can only accept the signals coming from recoil protons in order to detect neutrons effectively. More information on e16042 experiment can be found here [70]. Detailed description of the WMU Veto Wall

construction and calibration is done in the following chapters.

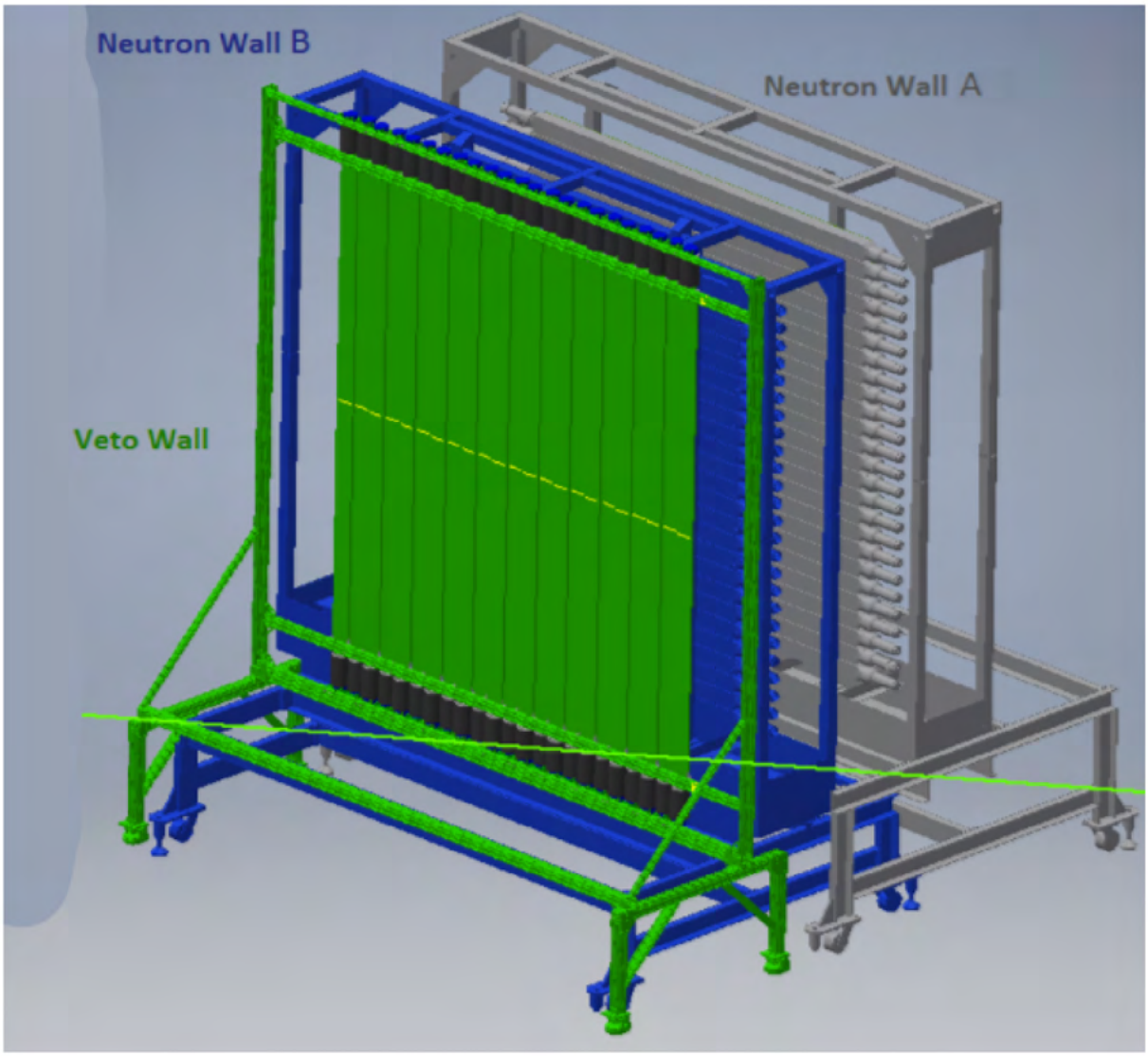

Figure 3.1: A schematic diagram of the WMU Veto Wall placed in front of the Neutron Wall. Two Neutron Walls- Neutron Wall B and Neutron Wall A are placed behind the WMU Veto Wall as shown in diagram.

Figure 3.1 shows a schematic arrangement of the WMU Veto Wall and the LANA also referred as the Neutron Wall A and the Neutron Wall B. The WMU Veto Wall was placed in front of the Neutron Wall B and the Neutron Wall A is behind the Neutron Wall B. The WMU Veto Wall's dimension is such that it completely shadows the Neutron Wall. Therefore, charged particles can be completely vetoed from neutrons in the LANA. Top panel of Figure 3.2 shows the spectra on the Neutron Wall when the WMU Veto Wall has multiplicity zero. Particles in this spectra are neutrons and gammas. But when the

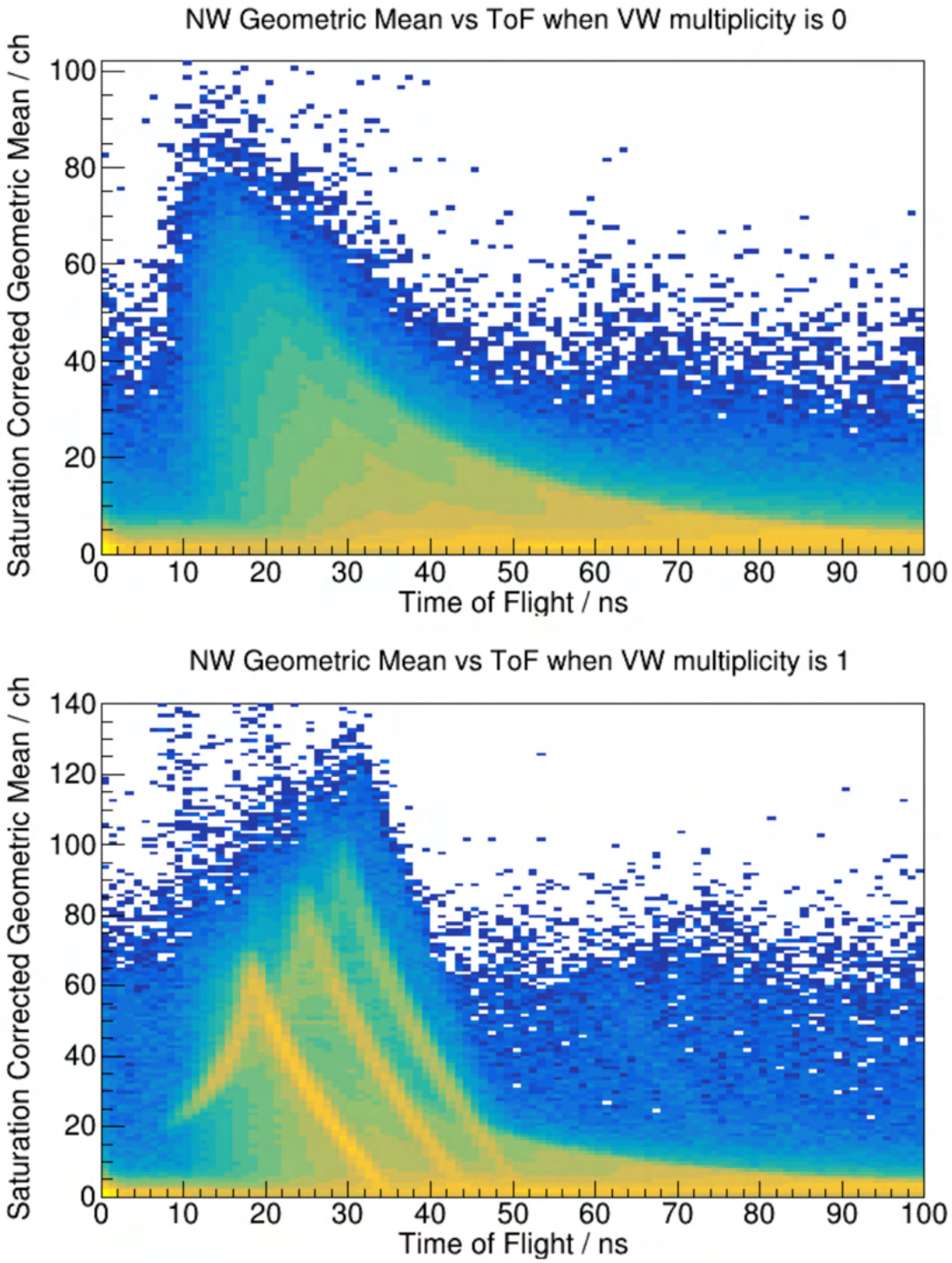

Figure 3.2: Particles on the LANA after gating on the WMU Veto Wall with multiplicity 0 (top panel) and multiplicity greater and equal to 1 (bottom panel). X axis represents the time of flight of particles in nano seconds and y axis represents saturation corrected geometric mean of the light output.

multiplicity of the WMU Veto Wall is 1 we also see charged particles in LANA as well. We can also see the PID lines of hydrogen isotopes (protons, deuterons and tritons) in the bottom panel of Fig 3.2.

3.2 Experimental Setup

Two experiments e14030 and e15190 were conducted over two weeks in February and March 2018 in S2 Vault NSCL. The K1200 Cyclotron produced the beams of ^{40}Ca and ^{48}Ca at 56 MeV/A and 140 MeV/A. The beam and target combinations are shown in Table 3.1. Though we also took the data for the mixed systems such as ^{40}Ca on ^{64}Ni, ^{40}Ca on ^{124}Sn, ^{48}Ca on ^{58}Ni and ^{48}Ca on ^{112}Ni, we did not used them for this analysis.

Table 3.1: A combinations of the different beams and targets used in experiment.

Beam	Targets			
^{40}Ca(20n,20p)	^{58}Ni(30n,28p)	^{64}Ni(36n,28p)	^{112}Sn(62n,50p)	^{124}Sn(74n,50p)
^{48}Ca(28n,20p)	^{58}Ni(30n,28p)	^{64}Ni(36n,28p)	^{112}Sn(62n,50p)	^{124}Sn(74n,50p)

Figure 3.3: The target ladder used in experiment. It starts with a focus, blank, four different targets (Ni, Sn) and CH_2 target.

The experimental setup consists of a vacuum chamber and various detectors. Some detectors along with targets were placed inside the vacuum chamber while the detectors that identify particles based on the time of flight technique were placed further away from the vacuum chamber. The schematic diagram of the experimental set up is shown in Figure 3.4. Figure 3.5 shows the experimental Setup of inside of the vacuum chamber.

Microball, HiRA, Forward Array and Downscale Scintillator (not shown in picture) were kept inside the vacuum chamber while the WMU Veto Wall, two Neutron Walls

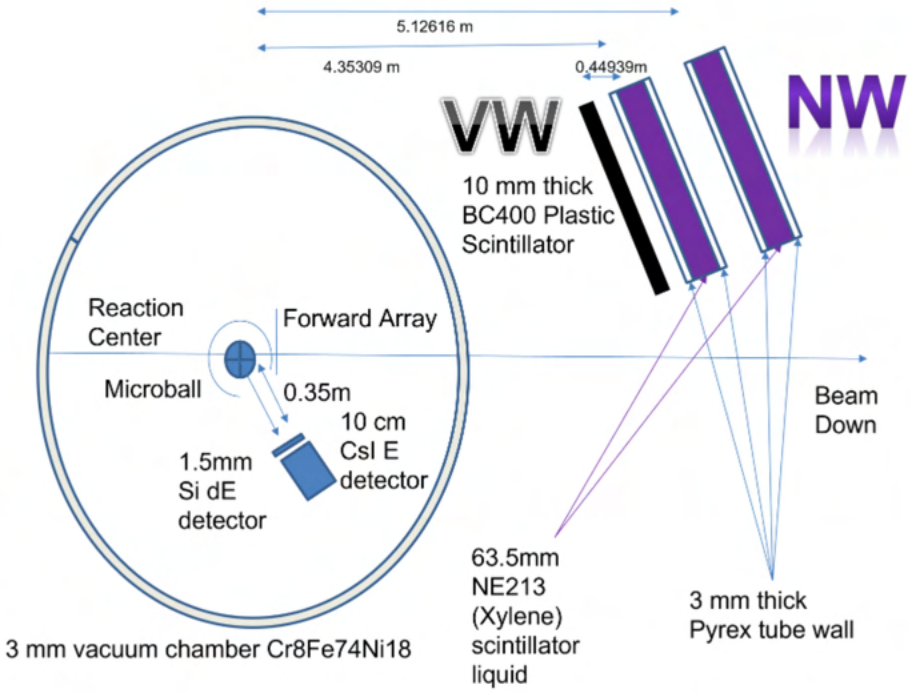

Figure 3.4: Schematic diagram showing the experimental setup (not up to scale). The measurements shown here were taken using laser beam.

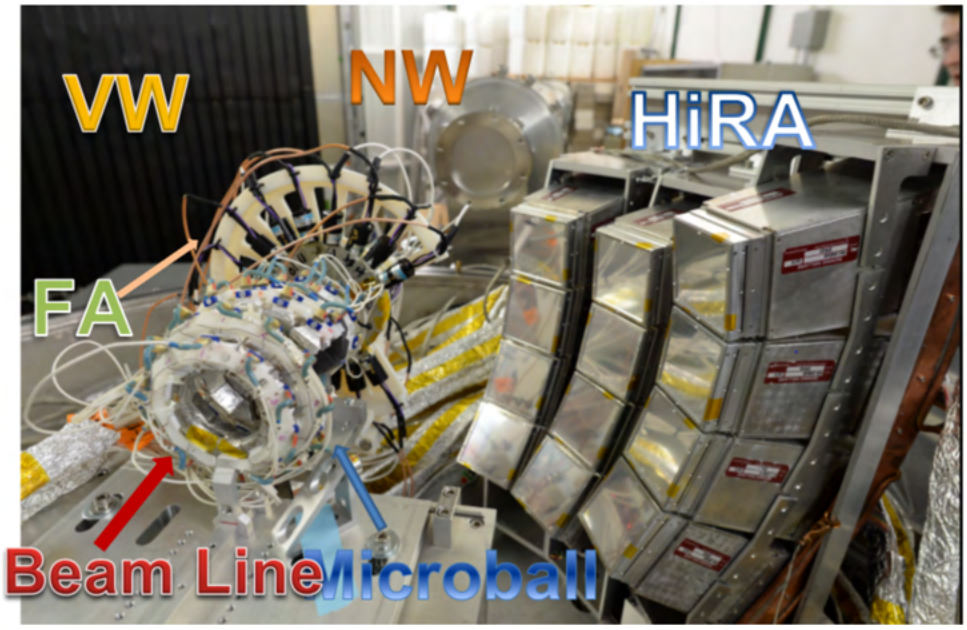

Figure 3.5: Experimental setup showing beam line and different detectors a)Microball b)HiRA c)Forward Array(FA) d) WMU Veto Wall(VW) and e)LANA (NW). This picture was taken after the commencement of experiment.

and Shadow bar stand (not shown in picture) containing shadow bars were kept outside the vacuum chamber. The LANA and the HiRA are kept at same azimuthal angle

from reaction center so that we can measure neutrons and charged particles of similar energy range by these detectors respectively. Each of those detectors mentioned above is discussed in more details below.

3.3 MicroBall

In order to study the centrality of the collision, determining the impact parameter is essential. It can be extracted from the multiplicity of emitted particles from the collision. We used the Microball detector to measure the multiplicity. Microball was one of the detectors placed inside the vacuum chamber close to the reaction center. It consists of 95 CsI scintillators arranged in nine rings. The angular coverage of these scintillators is from about 4.0^0 to 171.0^0 [71]. Different rings have different thickness of CsI; for example Ring 1 has 9.85 mm while ring 9 has 3.66 mm crystals. Ring 1 CsI crystals are thicker because ring 1 is closed to the reaction center where high energetic particles are produced. To protect these CsI scintillators from different substrates like light - a 0.9 mg/cm^2 Al foil was used in the front surface. High Z elemental foils such as Pb/Sn foils of different thickness were used in the frontal surface to stop delta electrons. The thickness of these foils varies from 73.5 mg/cm^2 in ring 1 to 9.8 mg/cm^2 in ring 9. To protect CsI from being hit by the beam, ring 1 and ring 9 were removed during the experiment. Ring 6 was also removed for the target spacing. In order to provide path for particles to hit the HiRA detector, some additional scintillators were removed as well. Those scintillators included four scintillators from ring 3, three from ring 4 and three from ring 5 [72]. Figure 3.6 and Figure 3.7 are the schematic diagram of Microball and a picture of Microball used in the experiment, respectively, while Figure 3.8 shows the view of the Microball along beam direction. It also shows the targets mounted on the target ladder inside the microball.

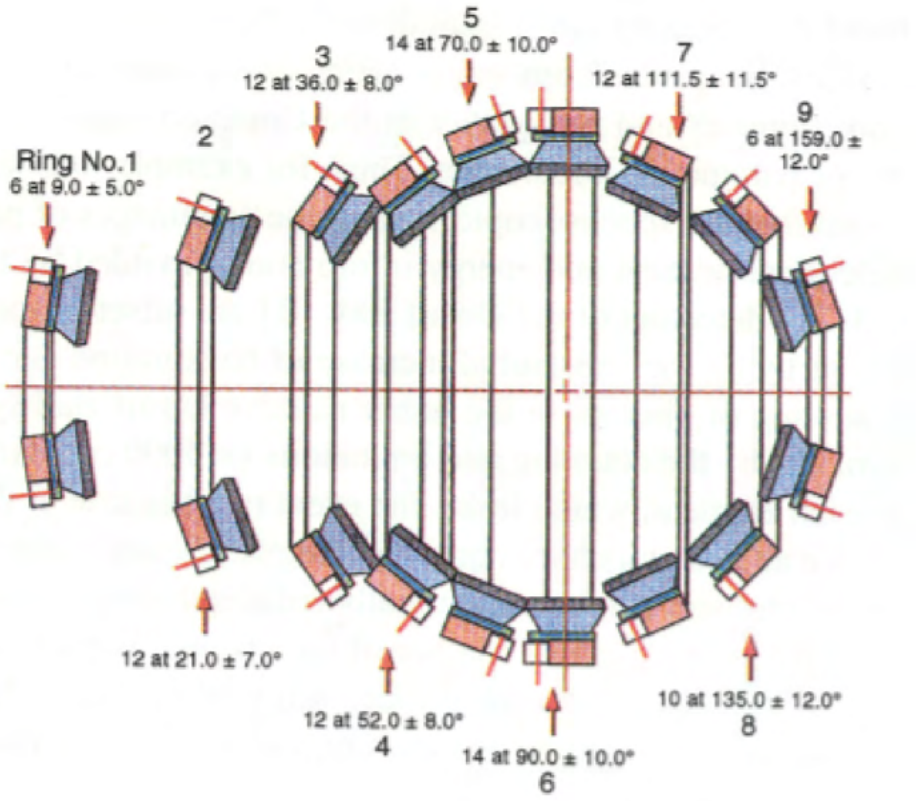

Figure 3.6: Schematic diagram of the vertical section of Microball. The Cesium Iodide scintillators are in grey facing towards the inner side and are attached to light guides in blue trapezoids. Green color patch are the diodes. Scintillators are supported by Delrin rings(red shaded area). Ring numbers with number of scintillators and angular coverage are also shown [71].

3.4 HiRA

High Resolution Silicon Array, abbreviated as HiRA is a double-sided silicon strip detector mounted in front of the four cesium iodide (CsI) crystals, which is collectively called as a telescope. In an original HiRA telescope, 4 cm CsI crystals were used with silicon strip detectors to measure charged particles. The Si-CsI detector uses dE-E energy loss technique to identify charged particles in the HiRA telescope [73]. If charged particles punch through silicon strip, energy is called as dE and the energy deposited in 4 cm CsI crystals is called as E. A charged particle must stop in CsI in order to be identified.

For high energetic charged particles like protons, deuterons, tritons, 4 cm CsI crystals are also a medium to punch through rather than stopping them which results in depositing

Figure 3.7: Microball detector. Ten scintillators were removed to give path for particles to HiRA.

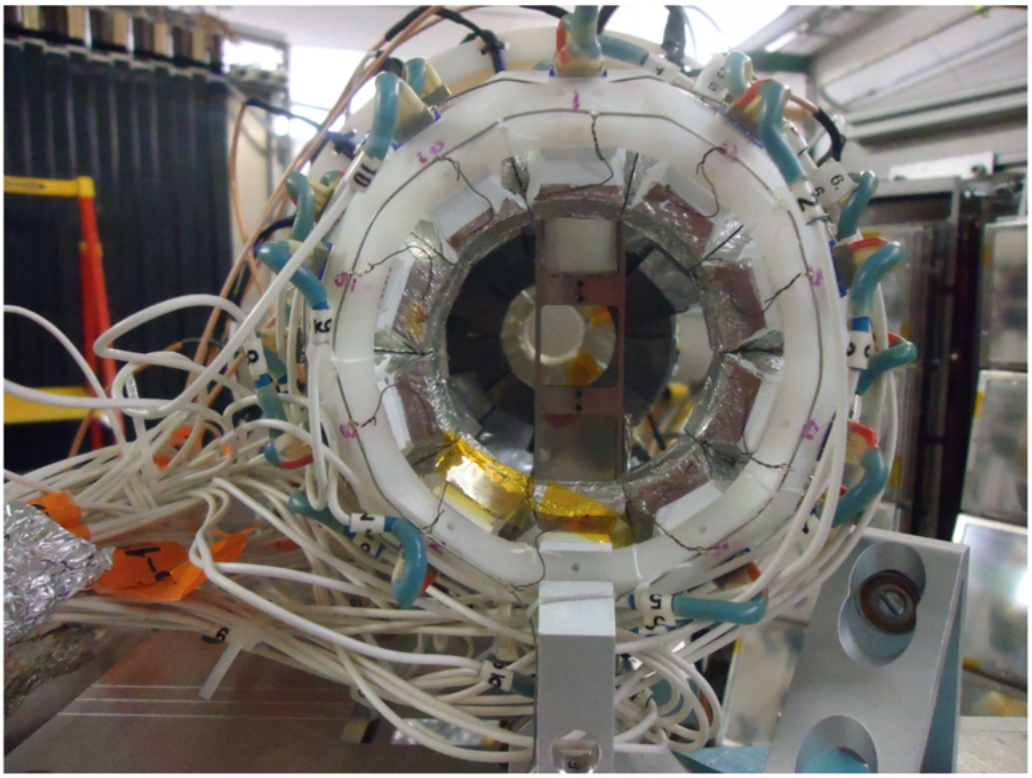

Figure 3.8: View of Microball from beam entry direction. Targets mounted on target ladder can be seen inserted inside the Microball.

a small fraction of their total energies. Since we needed to measure the high energetic charged particles in our experiment, we had to modify HiRA telescope. The original cesium iodide crystals were replaced with new ones that are 10 cm long so that they

can measure protons, deuterons and tritons up to 200 MeV, 263 MeV and 312 MeV, respectively [74]. That updated telescope, also know as HiRA10, consists of 1.5mm double sided silicon strips detector (DSSSD). Both sides of DSSSD have 32 strips (front vertical and back horizontal strips). About 2mm wide strips of DSSSD on electrodes on front and back receive pulse-indication of charge particle and these strips correlate to localize trajectory to a point pixel. Calibration of HiRA10 telescope is described in details in Reference [75]. Figure 3.9 shows the modified HiRA10 telescopes arranged in three towers; each tower consisting of four telescopes.

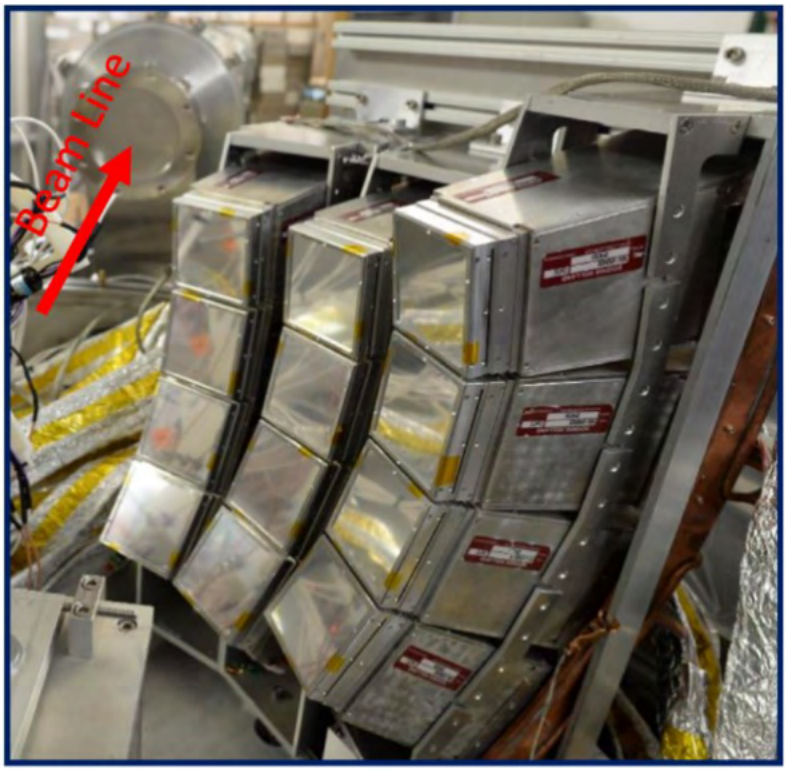

Figure 3.9: Twelve HiRA10 telescope arranged in three towers.

3.5 Forward Array

Forward Array was originally constructed in 2009 at Western Michigan University to study the density dependence of the symmetry energy with emitted neutrons and protons-e09042 [76].. Modifications to it were done at Western Michigan University for our experiment Forward Array consisted of a circular aluminum plate of 4.5 inch diameter.

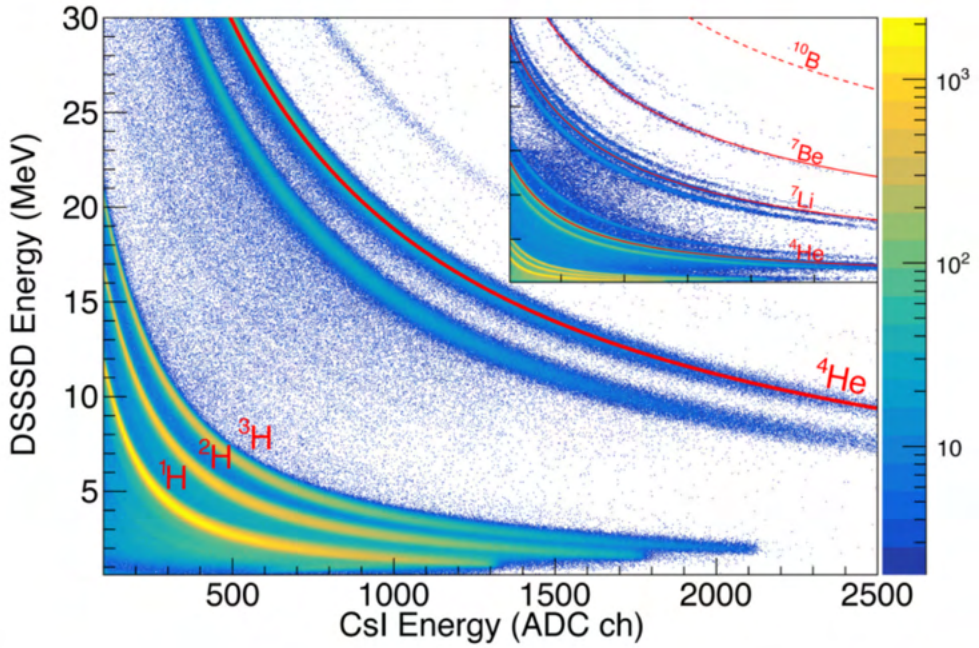

Figure 3.10: Particles Identification using the loss of energy (dE-E) technique. X axis is the CsI residual energy in ADC channel (E) and Y axis is calibrated DSSSD energy loss(ΔE). Red lines are the PIDs obtained from simulations for respective isotopes. Top right plot is the extended DSSD energy upto 120 MeV showing different isotopes at that energy [75].

One inch diameter hole at the center allowed the passage of the beam. A total of 16 NE 110 plastic scintillators, each wedge in shape, are attached on the circular plate. Each scintillator has a reflective paint of Bicron BC-620 to enhance the internal reflection of light. It is then wrapped in aluminum mylar foil in order to prevent light leak and cross talks between the adjacent crystals. The unwrapped and unpainted edge is coupled with Hamamatsu R5600U Photo Multiplier Tubes using E5780 base [77].

In our experiments, we used 18 wedges, two more than what the original Forward Array had. Each of those two wedges were covering an azimuthal angle of 36^0, thereby covering the original gap. These two wedges had to be shorter than the previous sixteen ones in order to avoid shadowing the HiRA. For the same reason, the PMTs were attached to the back of those wedges. Forward Array was kept at 12 cm downstream from the reaction center and the center hole was aligned with the beam path. Figure 3.11 shows a schematic drawing of Forward Array while Figure 3.12 shows the beam upstream (left) and downstream (right) view of Forward Array.

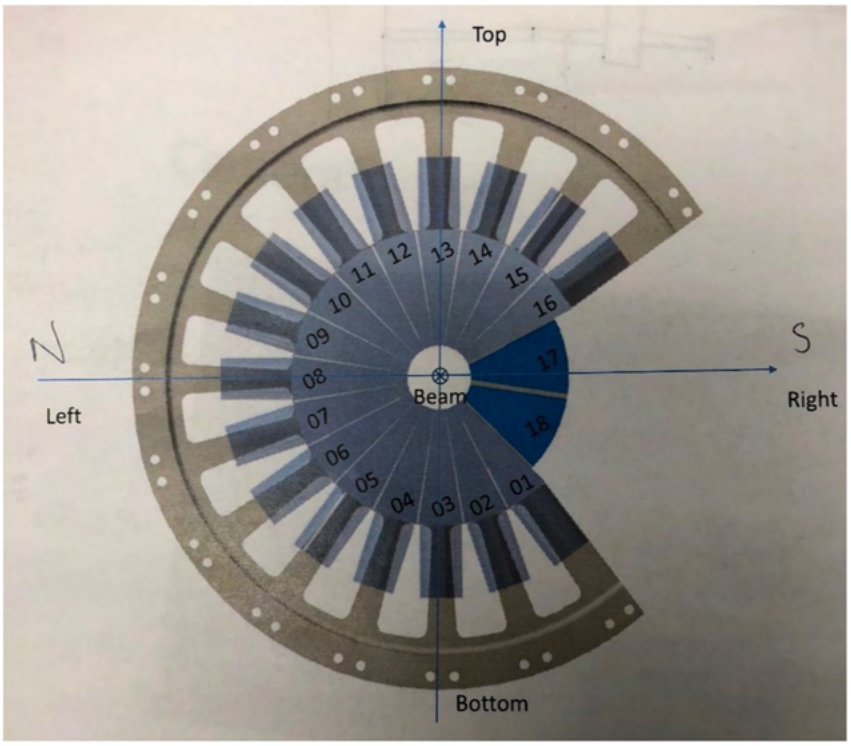

Figure 3.11: A schematic drawing of Forward Array showing the position of scintillators and PMTs.

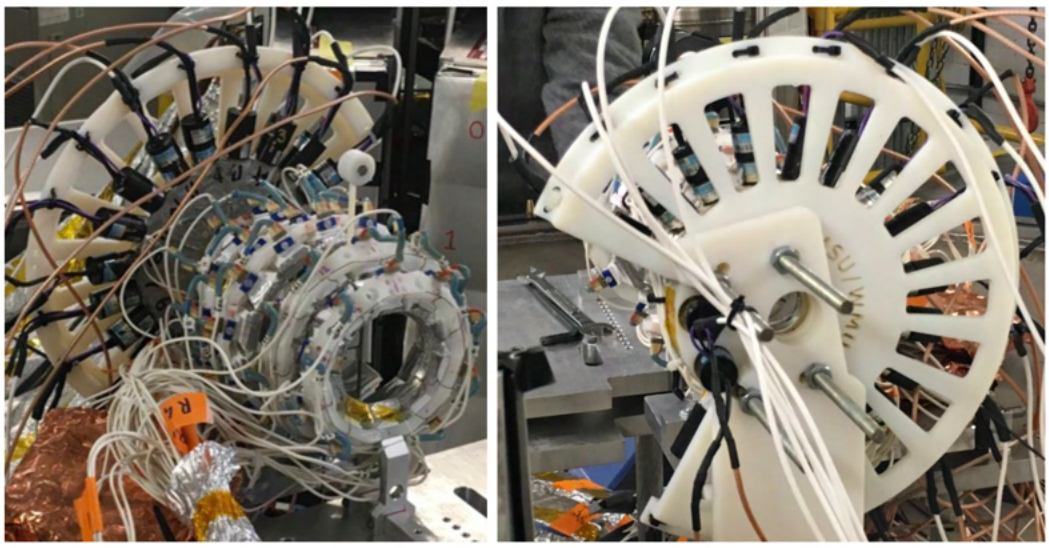

Figure 3.12: Forward Array used in the experiment. Left figure shows Forward Array along with Microball looking downstream. Right figure shows upstream view.

Forward Array is primarily used to measure the time of flight(ToF). ToF measurement can be used to calculate the energy of traveling particle knowing the distance, time travel

and the mass of the particle;

$$E = \frac{m \cdot v^2}{2} \tag{3.1}$$

The velocity is calculated as,

$$v = \frac{d}{t} \tag{3.2}$$

where d is the distance travelled by a particle and t is the ToF. If we know the start time and end time of the particle traveling distance d, then ToF(t) is the difference between them.

$$t = t_{END} - t_{START} \tag{3.3}$$

End time is the time recorded by any detector that detects the particle. In our case we have the WMU Veto Wall and the Neutron Wall and the start time is given by the Forward Array. When a prompt gamma particle hits the Forward Array, the start of the reaction signal (t_START) is produced. Many gammas are emitted from the reaction and they travel with the speed of light towards the Forward Array.The arrival time of triggering particles at the Forward Array is negligible as that detector was placed close to the target. Once we have the time of flight we can measure the energy of a particle using equation 3.1.

3.6 Large Area Neutron Array(LANA)

Being chargeless, neutrons are difficult for direct detections. Neutrons impart some of the energy to recoil charged nucleus through elastic scattering. However, measurement of the energy of such recoil nucleus does not give the neutron energy. To measure the neutron energy, the time of flight measurement is considered to be the best technique. Knowing the distance of travel and the time of flight of neutrons, we can calculate the velocity of neutrons and thus their energy. If the recoil nucleus has more energy, we can detect it easily. The condition for maximum energy of recoil nucleus is the mass of recoil nucleus being equal to the mass of neutron. This condition is achieved when hydrogen is

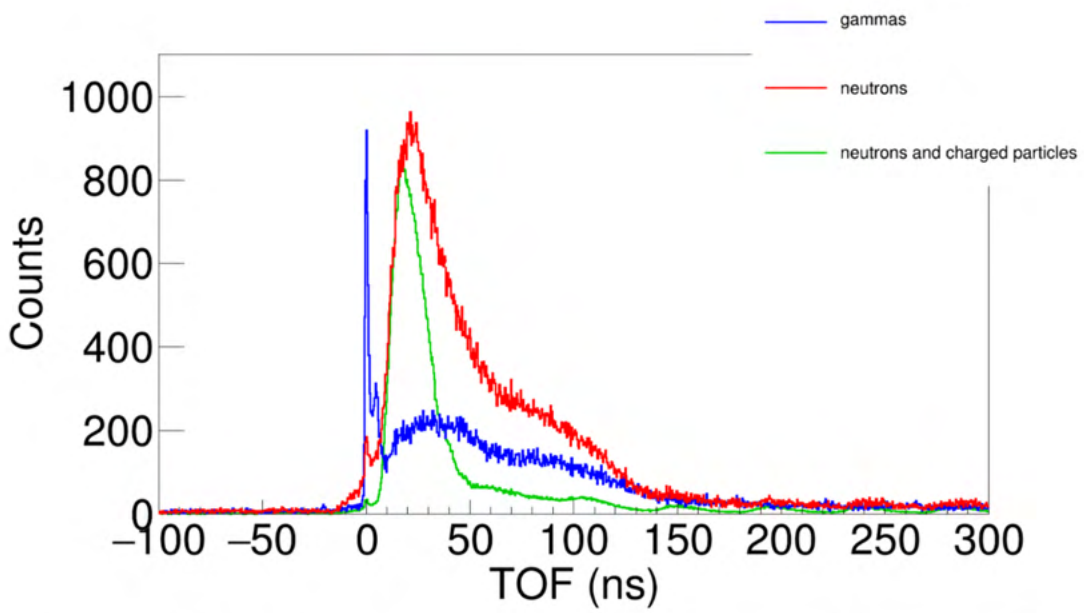

Figure 3.13: The time of flight spectra- color codes represent different particles. Red represents the time of flight of neutrons, green represents the time of flight of neutrons and charged particles while blue represents the time of flight of gammas. The spike at 0 ns represents the prompt gammas of the reaction.

used as scattering target for neutron. The detectors which use hydrogen scattering are also known as proton recoil detectors. Proton recoil detectors use organic scintillant such as plastic, organic solvents etc. When radiations strike the scintillant of such detectors, light pulses are produced. When a neutron hit the scintillator, a recoil proton is produced from hydrogen atom through elastic scattering which in turn deposits its energy in the scintillator. There are two Neutron Wall placed one after another. Each wall is made up of 25 bars which cover an area of 2 X 2 m^2. These bars are placed horizontally stacking one above the other. Each bar is a 2 m long Pyrex cell filled with liquid scintillator, NW-213 also known as Xylene. Pyrex cell is 3 mm thick and is coupled with Philips Photonics XP431213/04 model PMT on each end. To promote total internal reflection inside the Pyrex cell, its surface was left uncoated with any reflective material. There was a gap of 3 mm between the bars. The cell thickness and the gap reduce active area of 2 X 2 m^2 by 12% [78]. NE 213 when filled inside the cell covers a height of 7.62 cm in vertical direction while a thickness of 6.35 cm in horizontal direction. One of the Neutron Wall, NWB, is placed behind the WMU Veto Wall and NWA is placed behind NWB. The distance

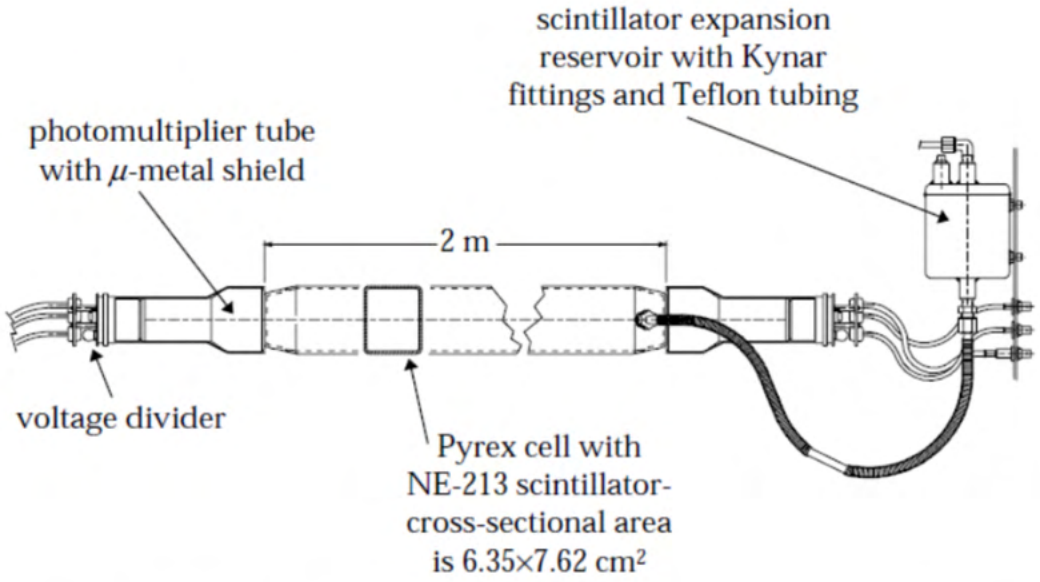

Figure 3.14: One LANA bar showing its connection with PMT [78].

between the front of NWB, NWA and target is 441.6cm and 517.5cm respectively. The walls are placed at an angle of 39.37^0 from the beam line [72]. Measurement of neutron energy is associated with the time of flight measurement. Time resolution is affected by the intrinsic time resolution of electronics, a rise time of the light pulse in a scintillator, an intensity of the scintillation light, a thickness of scintillator and collection efficiency of the available light. When light is produced in the scintillator, it travels along the scintillator undergoing multiple reflections and is collected as a light pulse at the PMT. Because of the multiple scattering of light in the scintillant, a number of photons moving towards PMT drops off by inverse square law ($\frac{1}{r^2}$). This creates uncertainty in the true start time of scintillation pulse as there will be uncertainty in flight path and time due to multiple scattering.

Since it is difficult to find the position of scintillation in the direction of thickness of scintillant, there is an uncertainty Δd (thickness of scintillant) in the distance d traveled by neutron from reaction center. Increasing the thickness of scintillant will though increase its efficiency but will decrease the time resolution.

Time uncertainty σ_t is determined from the width of prompt gamma peak from the

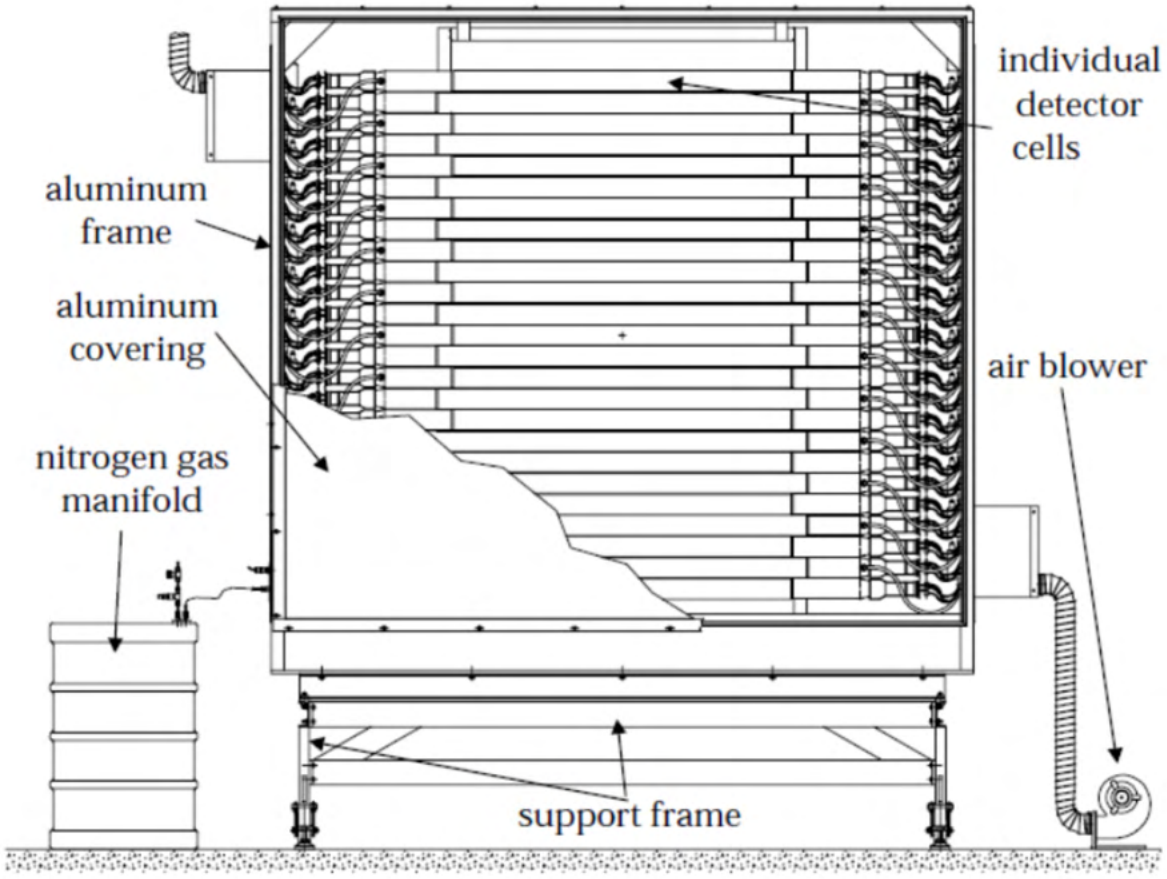

Figure 3.15: A drawing showing a cut away section of the LANA [78].

reaction. Using the width of prompt gamma peak and thickness of scintillant in detector, we can determine relative energy resolution. Time uncertainty is $\Delta t = \mathrm{t}\ \frac{\Delta d}{d}$. If energy is $\mathrm{E} = \frac{1}{2} m \cdot v^2 = \frac{1}{2}\ \mathrm{m}\ (\frac{d}{t})^2$ uncertainty in energy is given by $(\sigma_E)^2 = (\sigma_d)^2(\frac{\partial E}{\partial d})^2 + (\sigma_t)^2(\frac{\partial E}{\partial t})^2$ and the relative energy resolution is $(\frac{\sigma_E}{E})^2 = 4(\frac{\sigma_d^2}{d^2} + \frac{\sigma_t^2}{t^2})$.

Horizontal position of a particle is calculated from the difference of the time received by each PMT of the same bar. The position resolution is 7.65 cm/ns [78]. The LANA detects not only fragments from the experiment but also a lot of background radiation like cosmics and gammas. PMTs produce electric pulse after receiving light produced by particles when they interact with the scintillator. The shape of the pulse plays an important role

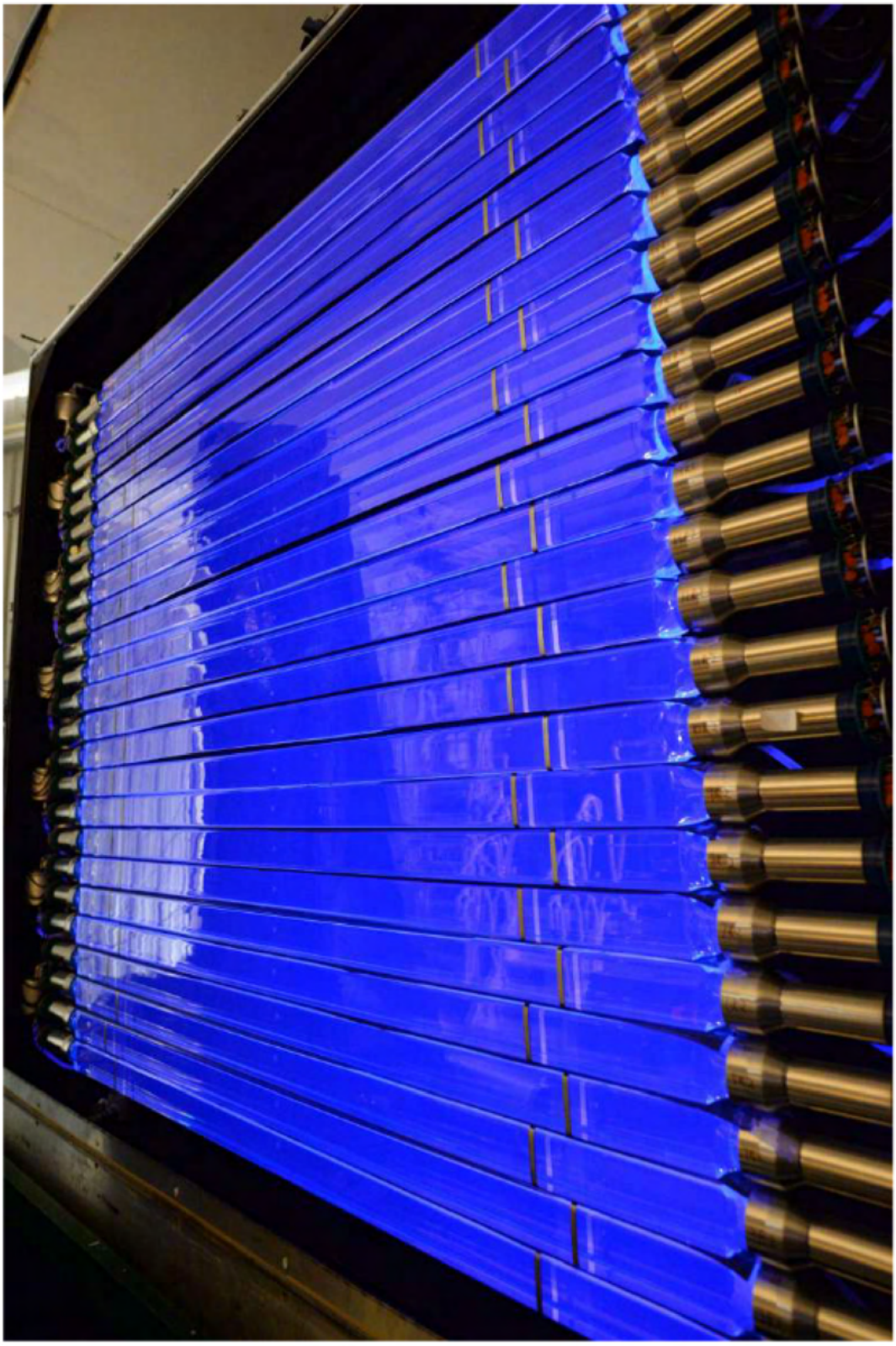

Figure 3.16: Illumination of the LANA wall through ultra violet light.

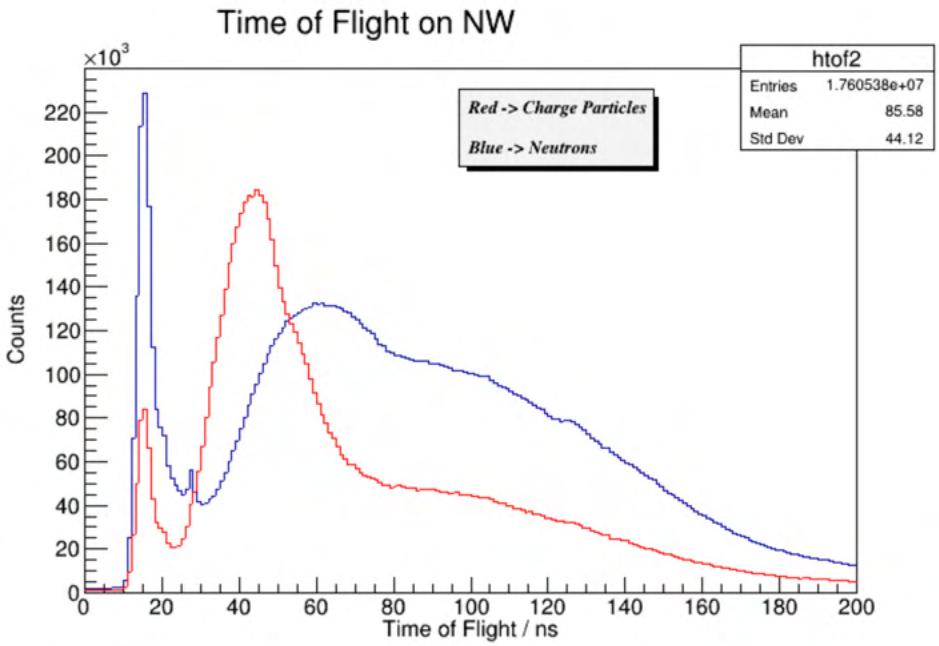

Figure 3.17: Time of flight spectra as seen in the Neutron Wall for neutrons and charged particles. The spike represents the prompt gammas of the reaction.

in separating fragments from the background. Light produced from ionizing radiation has prompt fluorescence (decay constant of few nano second) and delayed fluorescence (decay constant of few hundred ns). Cosmics and gammas produce small fraction of its light in delayed fluorescence while recoil proton from neutron scattering produce large fraction in delay fluorescence. This gives different time shape pulses for neutrons and other backgrounds [78]. That pulse shape technique is used to separate backgrounds and gammas from neutrons to obtain a fine neutron spectra which can be used for further analysis [79, 80].

3.7 Shadow Bar

Neutrons and charged particles produced from the reaction can be scattered from the equipment and anything else that comes in their way. In order to measure the background scattering of neutrons and protons, shadow bars are used in the experiment. Four brass shadow bars, each 30 cm long (shown in Figure 3.18) are kept in the stand at about 130 cm from the reaction center. These bars partially or completely stop charged particles

like protons, deuterons, tritons and neutrons. A figure of a shadow bar stand with four shadow bars is shown in Figure 3.19.

Figure 3.18: A 30 cm brass Shadow Bar to measure the background efficiency [81].

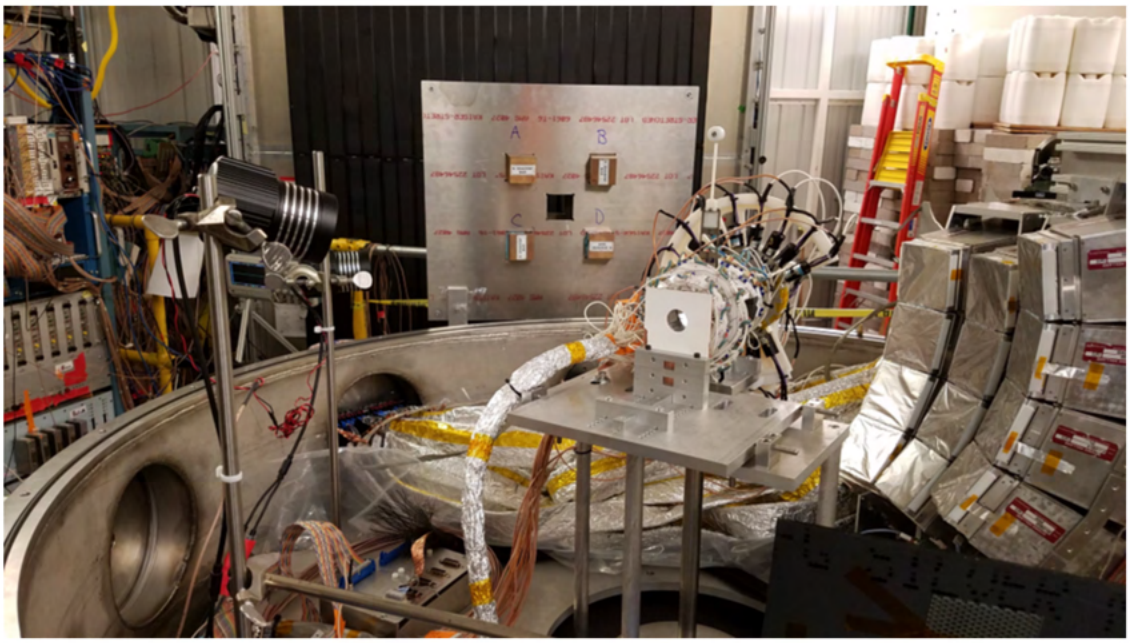

Figure 3.19: Shadow bar stand with four shadow bars in it. This set up was placed in front of the vaccuum chamber during the experiment [82].

3.8 WMU Veto Wall

WMU Veto Wall was designed to identify the charged particles, ultimately, to separate the charged particles from neutrons hitting the LANA. The WMU Veto Wall consists of

25 plastic scintillator bars. Plastic scintillators are low atomic number detectors which have small electron backscattering. This makes them suitable for particle physics experiments. Different destabilization factors such as humidity, temperature, radiation, uv light, oxygen create free radicals in the plastic. These free radicals initiate the polymeric degradation [83] which deteriorates a detection efficiency, a light yield and the energy resolution of the plastic scintillator shifting Compton maxima in gamma spectra. The energy calibration of a thin plastic scintillator accounting for non uniform light output was done previously [84]. An example of the experimental spectra of plastic scintillator for ^{60}Co gammas along with Monto Carlo simulations shown in Figure 3.20 below are in good agreement.

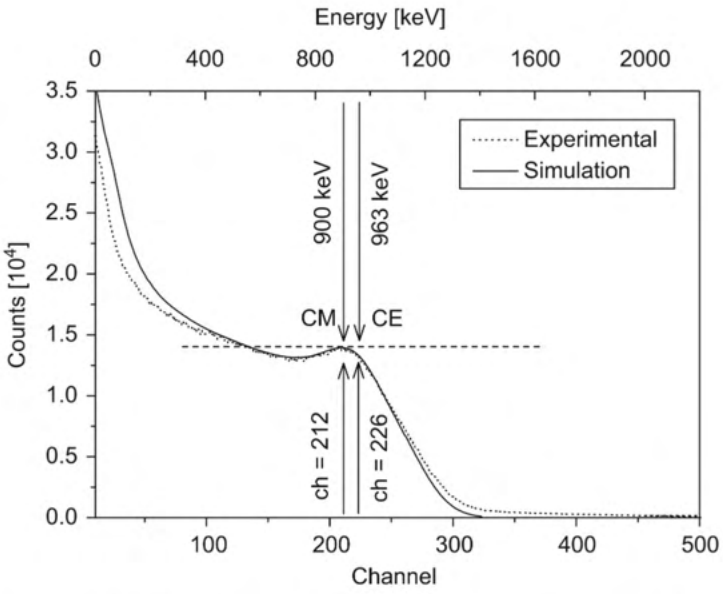

Figure 3.20: Simulated ^{60}Co γ ray spectra compared to measured one with corresponding energy value and channel for Compton edge [84].

The characterization of EJ 200 plastic scintillators using different radionuclide sources for active shielding purpose was done in reference [85]. In that experiment, radionuclides and different sources ^{137}Cs, ^{232}Th, ^{238}PuC, $^{241}AmBe$ were used to study the response functions for the detection of gamma rays. These responses were fitted around the Compton edge with theoretical simulations. Compton edge is the fractional energy registered by the detector when gamma ray is scattered by the scintillant of the detector. The full back scattering of the gamma ray by scintillant corresponds to the hightest energy

deposition in the detector. That energy is referred to as a Compton edge. Around the Compton edge, experimental and theoretical response functions were in good agreement especially with ^{137}Cs [85]. Figure 3.21 shows response of plastics to different radionuclides ^{137}Cs, ^{232}Th, ^{238}PuC. The response of EJ 200 Plastic scintillator to different charged particles can be found in [86]. The structural properties, physics constants, gamma attenuation coefficient of EJ-200 and light collection in the plastic scintillator can be found in references [87], [88], [89], [90].

Each WMU Veto Wall detector is 2.5 m in length, 9.4 cm wide and 1 cm thick. 25 bars are installed on an aluminum frame and it covers the Neutron Wall. To prevent the gap between the neighboring detectors, a 3mm overlap between the adjacent bars is made. The 9.4 cm wide bars are tapered to 5.65 cm at the end so that they can be attached to 7.62 cm diameter light guides [72]. Each bar is coupled to the PHOTONIS XP3462 Photomultiplier Tubes through light guides. Those plastic scintillators were wrapped with black paper and vinyl. The purpose of the wrapping in black is to make the scintillators light tight so that there is no leakage of light from outside. A photo multiplier tube is a photosensitive vacuum tube with a photo cathode, focusing electrode, electron multipliers and an anode. A schematic diagram of a photomultiplier tube is shown in Figure 3.22. Figure 3.22 shows light suffering multiple reflections inside the scintillator. When light finally enters the PMT, it hits the photocathode and primary electrons are produced by photoelectric effect which are focused by focusing electrode. Those electrons hit the electron multiplier called dynode and amplified secondary electrons are produced which follow a series of dynodes thereby multiplying the number of electrons. These electrons finally get collected at anode and an output signal is produced. The ratio of anode output current to the photoelectric current from photocathode is referred to as a gain of PMT.

$$G = \delta^n \tag{3.4}$$

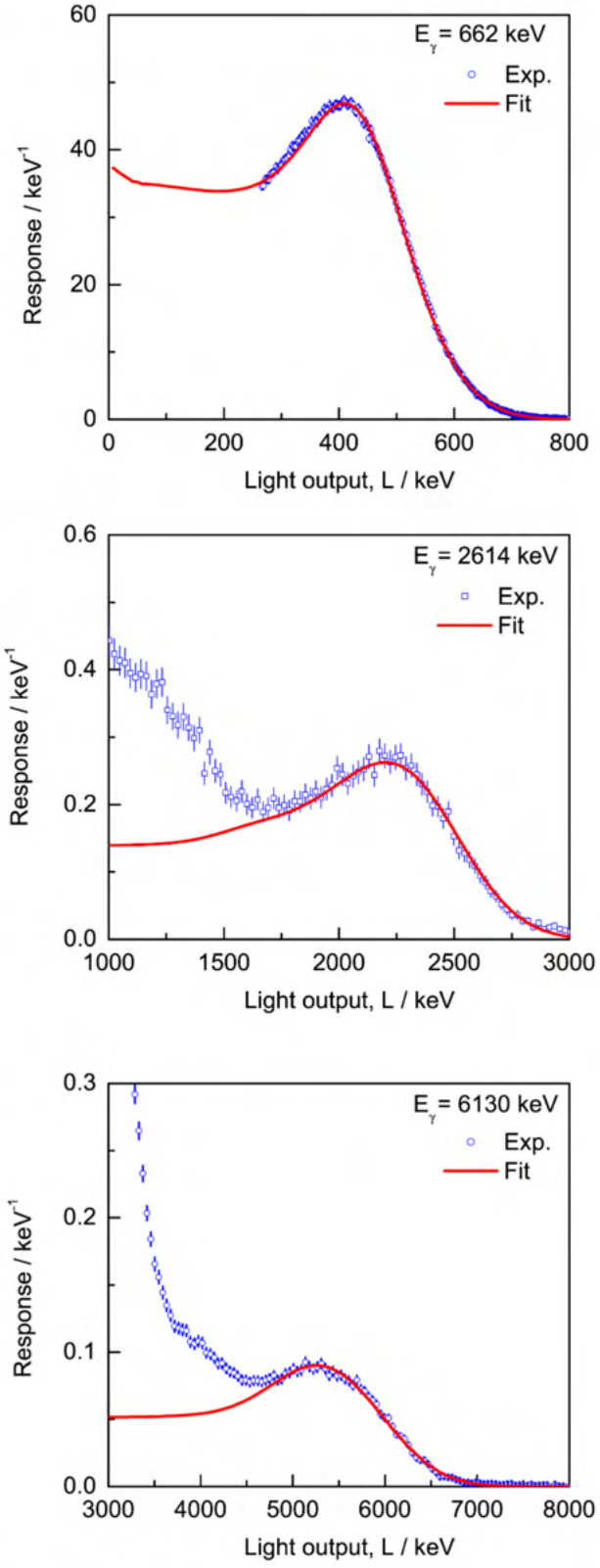

Figure 3.21: Comparison of experimental response function of EJ-200 plastic scintillator (25 mm thick) with theoretical response.Top shows experimental response from 137Cs, middle from 232Th and bottom from PuC source [85].

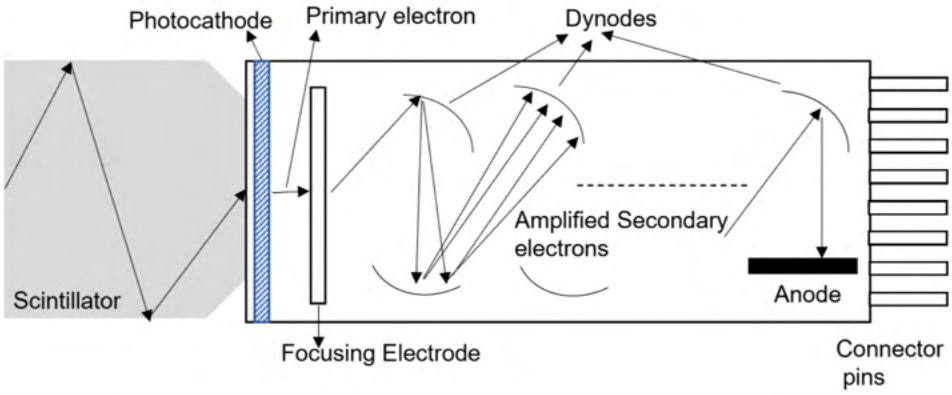

Figure 3.22: Schematic diagram of Photo Multiplier Tube.

G is a gain, n is the number of dynodes and (δ) is average secondary emission ratio

$$\delta = A \cdot E^{\alpha}, \tag{3.5}$$

where: A is constant, E is the interstage voltage, α is a coefficient determined by dynode material and geometric structure (value of α is from 0.7 to 0.8).

$$G = (A \cdot E^{\alpha})^{n} \tag{3.6}$$

$$G = A^{n} \cdot (\frac{V}{n+1})^{\alpha n} \tag{3.7}$$

$$G = \frac{A^{n}}{(n+1)^{\alpha n}} \cdot V^{\alpha n} \tag{3.8}$$

$$G = K \cdot V^{\alpha n}, \tag{3.9}$$

where V is the applied voltage between cathode and anode and K is constant [91].

The WMU Veto Wall is about 393.3 cm from the target. Both Neutron Walls and the WMU Veto Wall are parallel to each other covering the same solid angle from the target. The WMU Veto Wall bars were labelled with numbers from 0 to 24 starting from left to right from the target looking downstream. Construction and calibration of the WMU Veto Wall is explained in details in the following chapters.

PMTs were powered with high voltage supply called LeCroy 1440 [92]. A high voltage

is applied between photocathode and anode. A typical voltage divider circuit is shown in Figure 3.23. The circuit consists of resistors in between the dynodes and a decoupling capacitor connected parallel to the nth Resistor. Anode is grounded through a load resistor.

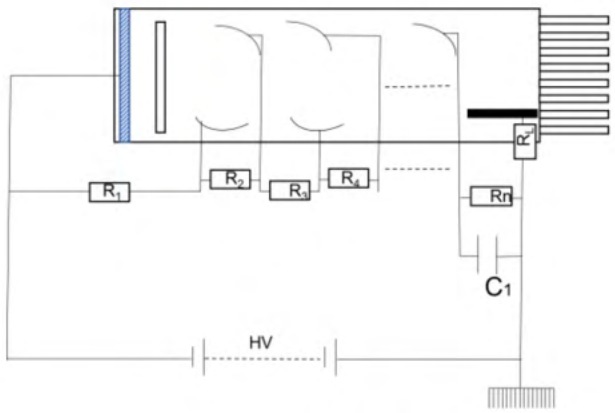

Figure 3.23: A voltage bias circuit for PMT operation.

3.9 Downstream Scintillator(DSS)

Downstream scintillator is a plastic scintillator placed downstream of the microball. This scintillator is connected to the photomultiplier tube. The main purpose of this scintillator is to count the amount of beam passing through the target. DSS was used only for calibration and the x-section measurements. DSS was used to determine the cross section and impact parameters for different multiplicities of the Microball. Those runs were performed with DSS in and out. DSS "in" measures the beam count while DSS "out" measures the back-scattering of particles into the Microball. Such calibration runs were performed for all sets of beam, targets and energies.

Chapter 4

Commissioning of the Veto Wall Detector

4.1 Introduction

Observables involving neutrons are essential to understand the dynamics of nuclear reactions involving neutron−rich isotopes. Study of neutrons is not enough to understand the equation of state. In heavy ion collisions, neutrons and many charged fragments are produced. Apart from detecting neutrons, detection of charged particles is also required. Heavy−ion collision reactions require detectors to detect all those particles, to identify them and to measure their energy. Large Area Neutron Array (LANA) was used in our experiment to identify neutrons and measure their energy using the time of flight technique. A detector placed downstream of reaction center, Forward Array(FA), provides a start time for the ToF measurements of neutrons. Neutrons interact with liquid scintillator of the LANA and recoil protons. However, protons are also emitted from the reactions. For accurate measurement of neutrons we need to distinguish these two sources of protons. To achieve that goal we need a detector that detects charged particles emitted from reactions. This detector is the WMU Veto Wall (VW).

The Veto Wall, placed in front of the LANA, identifies charge particles and that

information is used to "veto" protons hitting the LANA. The Veto Wall consists of twenty five plastic scintillators with Photo Multiplier Tubes (PMTs) at both ends. Each Veto Wall bar is 250 cm long, 9.4 cm wide and1 cm thick. Charged particles deposit energy in the Veto Wall and are detected while neutrons do not interact with it.

4.2 Construction of the Veto Wall

Organic scintillator is composed of a polymer base, a primary dopant and a secondary dopant. A particle hitting the scintillator excites the base and migrates to primary dopant producing detectable light. Secondary dopant then absorbs the detectable light from primary dopant and emits longer wavelength light which is detected by PMT [93]. Each bar of the Veto Wall consists of a plastic scintillator attached to the PMTs on either side via light guides. Light guide connects rectangular shaped plastic scintillator with a circular shaped PMT. The refractive index of light guide is matched with the plastic scintillator so that light guide does not alter the of amount of light passing through it. EJ-200 plastic scintillators were purchased from Eljen Technology [94]. The construction of the Veto Wall involved testing of PMTs, gluing of the light guide to the PMT, gluing of the PMT to the plastics scintillator and wrapping of the scintillator to make it light tight. All these steps are explained in details in the following sections.

4.2.1 Testing of PMTs

Photo Multiplier Tubes used in a bar should be functional. Since a bar has two PMTs on either ends, these PMTs should have preferably equal or nearly equal gain as different PMTs produce different output voltages even though they are given same the input voltages. So, testing the PMTs and gain matching them was the first step. Figure 4.1 shows our testing setup. PMTs were labeled with numbers. High voltage (SHV) cable from the power supply was connected to marked "power in" connector on the blue box (output divider) which has two outputs. One output was connected to the base of the

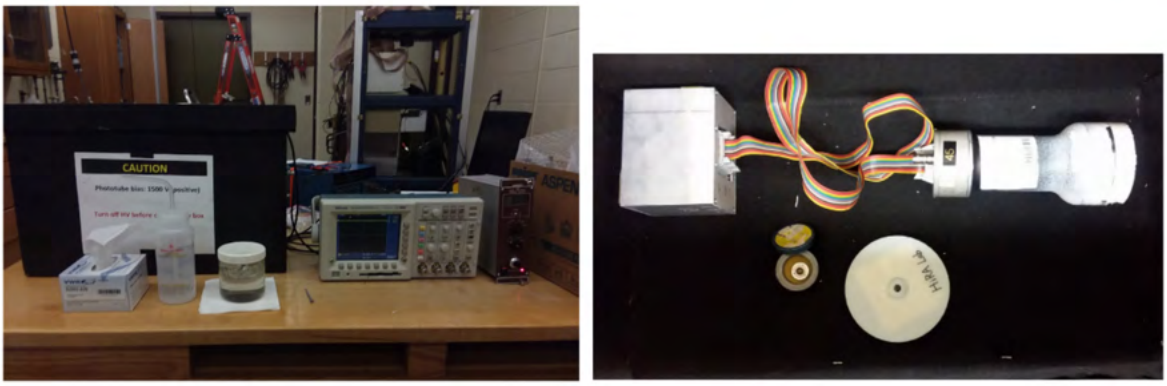

Figure 4.1: PMT testing kit which includes dark box, oscilloscope, ORTEC power supply, optical grease, PMT with base, alpha source, resistor divider box, scintillator with holder.

PMT via SHV cable and another output (the signal) was connected to the oscilloscope via a LEMO cable. A ribbon cable was used to connect a resistor divider box to the PMT. A glass surface of the PMT was cleaned thoroughly using alcohol and wipes and a layer of optical grease was applied to it. Optical grease prevents reflection and loss of light during transmission from one surface to another. Scintillator film with holder was placed gently in order to make a good seal between glass and film. Figure 4.2 shows a good and a bad contact. PMT with scintillator was placed inside the dark box and an alpha source was kept on the top as shown in Figure 4.3 (left). The box was covered with the lid. 1500 V was provided to the PMT and if the PMT was good, we could see the signal on the oscilloscope as shown in Figure 4.3 (right). An excel sheet was created to record the PMT number, full width half maximum of the signal, an amplitude and the maximum amplitude of the signal. Once the recording was done, voltage was turned down to zero and all connections were dissembled and the PMT surface was cleaned thereafter.

4.2.2 Gluing the Light Guide to the PMT

Light guides are glued to the glass surface of the PMT so that the light produced in a plastic scintillator is guided to the PMT. In order to maximize light transmission to the PMT, we use glue of the similar refractive index as the material it is gluing to. Our goal was to make a thin layer of glue with no air bubbles in between the light guide and

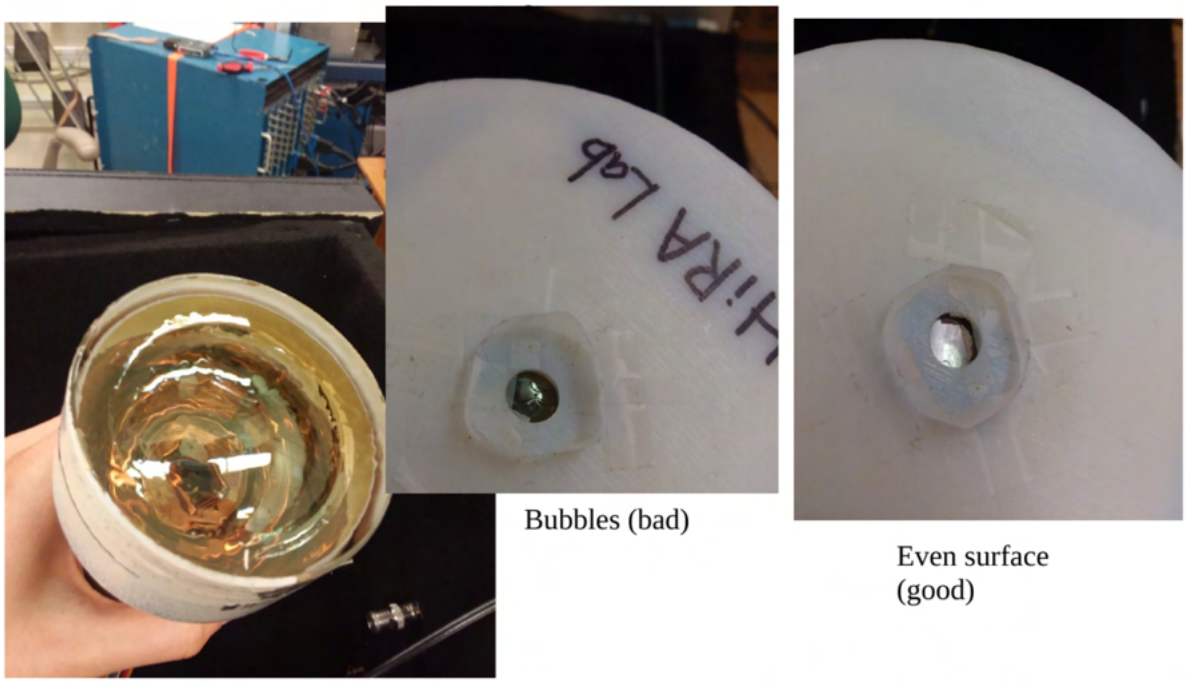

Figure 4.2: Left: glass surface of the PMT with optical grease, center: bubbles seen after placing the scintillator holder on the surface of the PMT, right: good surface after placing the scintillator holder on the PMT.

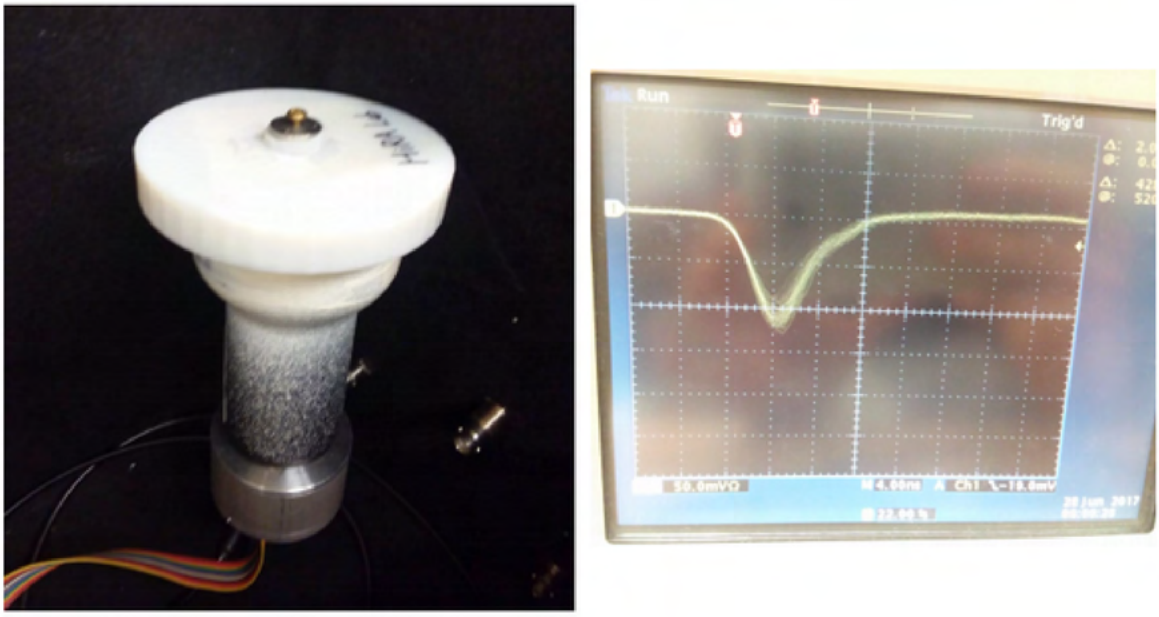

Figure 4.3: (Left)PMT with an alpha source kept inside the dark box, (right) signal as seen in the oscilloscope.

the PMT. We mixed 184 Silicone Elastomer Base with 184 Silicone Elastomer Curing Agent in a ratio of 10:1. Each light guide needed about 5.5 grams of glue. In order to

make the glue free of air bubble, we placed it in the vacuum chamber to degas. Once all the bubbles were pumped out and glue was seen clear, vacuum pump was turned off. To prevent the dripping of the glue down the body to base of the PMT, PMT was wrapped with black tape from the top and a ring of paper was attached making an "umbrella" as shown in Figure 4.4 so that it collects the dripped glue. During the gluing time the PMT

Figure 4.4: Paper ring makes umbrella like structure to hold the dripped glue.

should be upright and leveled so that glue can be poured smoothly on a flat surface and the light guide can be leveled on the top of the PMT. This setup was placed undisturbed for three days which is the curing time for the glue. Figure 4.5 shows a gluing stand, made of T-slotted frames, used to glue light guides to PMTs. The base of the PMT has connectors and screw. During gluing, connectors were made to rest outside the aluminum bar of the gluing stand and the screw was rested inside the hole of a rubber tape making the base of the PMT flat so that the PMT can be rested flat in upright position. The

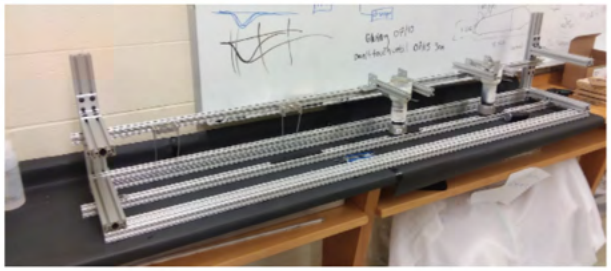

Figure 4.5: Gluing stand set up in lab

top of the PMT was supported by an U-shaped piece and zip ties were used to hold the PMT in place after it was leveled. Once the PMT is in position, the glue was poured on the glass surface. After placing the light guide on top of the PMT, UV flash light was used to detect bubbles. If any bubbles were seen, they were moved to the edge of the PMT by gently moving the light guide. Once the bubbles were minimized, the center groove of the light guide was aligned to make it parallel to the ribbon connector of the base. This was necessary as the tapered ends of the scintillators were later glued inside the grooves of light guides so that when these detectors are assembled in the frame they should remain flat like the LANA. For this, a laser beam was used and shined through the center of light guide. If the laser passed through the groove, it was aligned, if not, the light guide had to be realigned. At the end a teflon tape was wrapped around the edge between the PMT and the light guide. The first 24 hours after gluing was the most important so regular checking was done to see if the light guide has not moved.

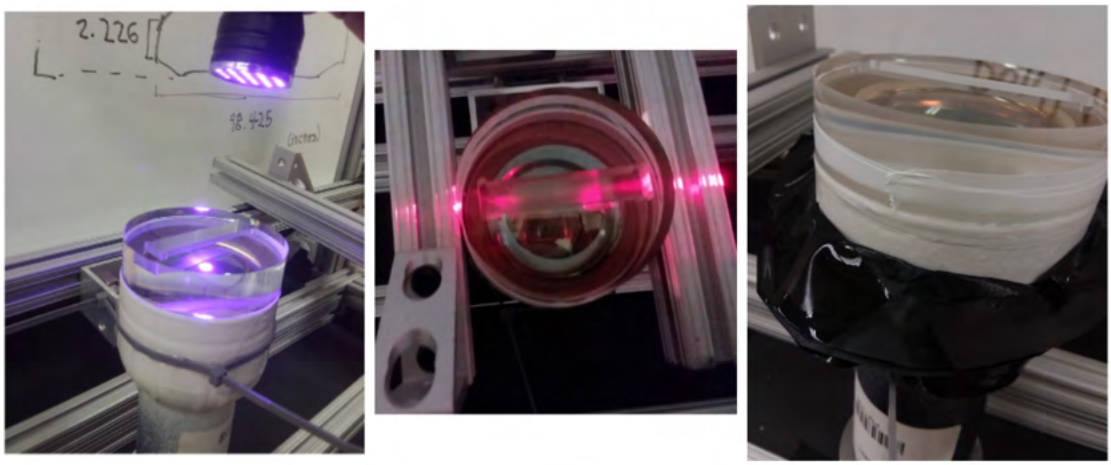

Figure 4.6: Left: using UV flash light to check any bubbles, center: using laser level to align the groove of light guide with base ribbon connector, right: using teflon tape to hold the light guide until the glue cures.

4.2.3 Gluing PMT to Plastic Scintillators

As all of the PMTs were labeled, once light guide was glued to the PMT, two PMTs with similar gains were taken and these PMTs were glued to the either end of the same

plastics scintillator. Plastic scintillators are wrapped along the body while few inches on either side were left unwrapped. This was done in order to glue the detector to the light guide. The groove in the light guide has dimensions of the scintillator bar. Optical cement was prepared to glue this end with the light guide as we wanted the connection to be permanent. The PMT was placed on the stand and leveled. Stand is such that it can be moved up and down. The end of the scintillator was aligned with the groove of the light guide. The optical cement was poured on the groove and aligned. The stand was moved up gently so that the end of scintillator fits exactly in the groove of the light guide leaving only a thin layer of glue in between. Gentle movement of the stand helped removing the trapped air bubbles. The setup was left undisturbed for 24 hours and after

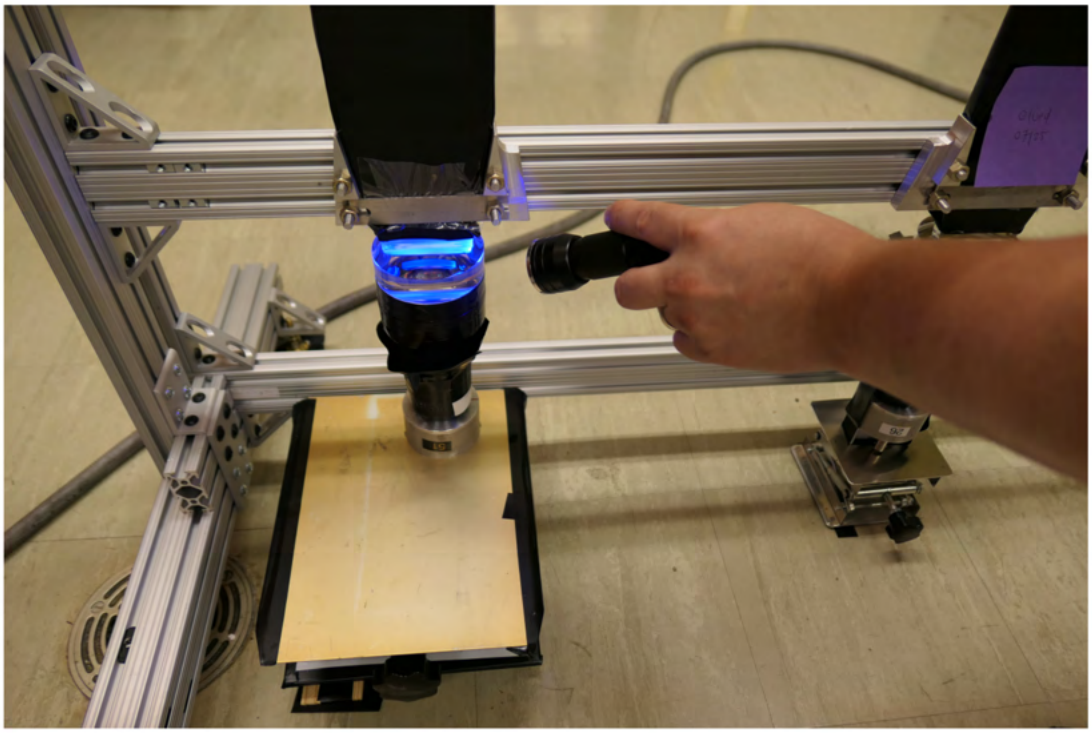

Figure 4.7: Checking for the air bubbles during gluing.

the optical cement(curing time is few hours) is fully cured, plastic scintillator was flipped to attach the PMT to another end of the detector.

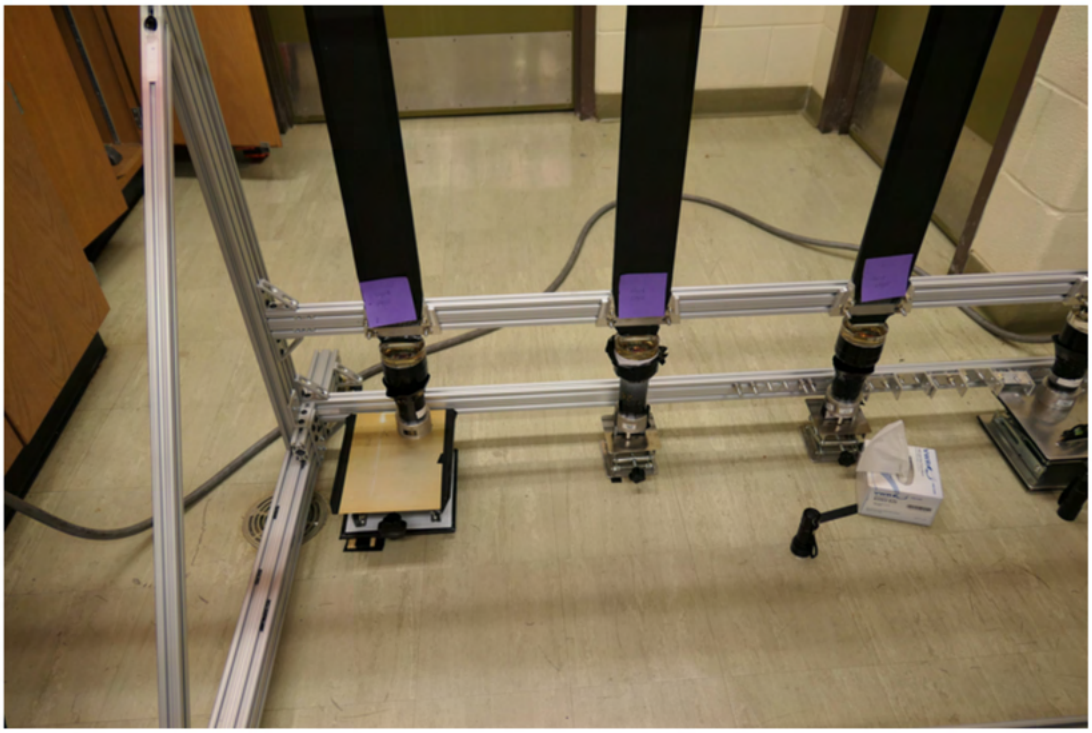

Figure 4.8: Gluing of the light guides to the plastic scintillators.

Figure 4.9: Shining UV flash light to the plastic scintillator.

4.2.4 Making the Scintillator Light Tight

Unwrapped portion of the plastic scintillator, the light guide and the PMT should be wrapped in order to make a bar light tight. For this purpose, the black paper and vinyl were used. Different shapes (tapered, semicircular, rectangular) of paper and vinyl pieces were made as shown in Figure 4.10 so that they cover the unwrapped region. First

Figure 4.10: Different shapes cutting used to wrap the bar.

the paper pieces were placed and then they were covered by a vinyl piece. Black electric tapes were used to attach them to each other and fit them in place. Minimum amount of tape should be used so that it would not provide extra thickness to the bar. To test the light−tightness of the bar, PMTs were biased. If the signal from the gamma source was seen on the oscilloscope, the PMT is light tight and if no signal was seen, the wrapping had to be fixed.

Figure 4.11: Wrapping the bar.

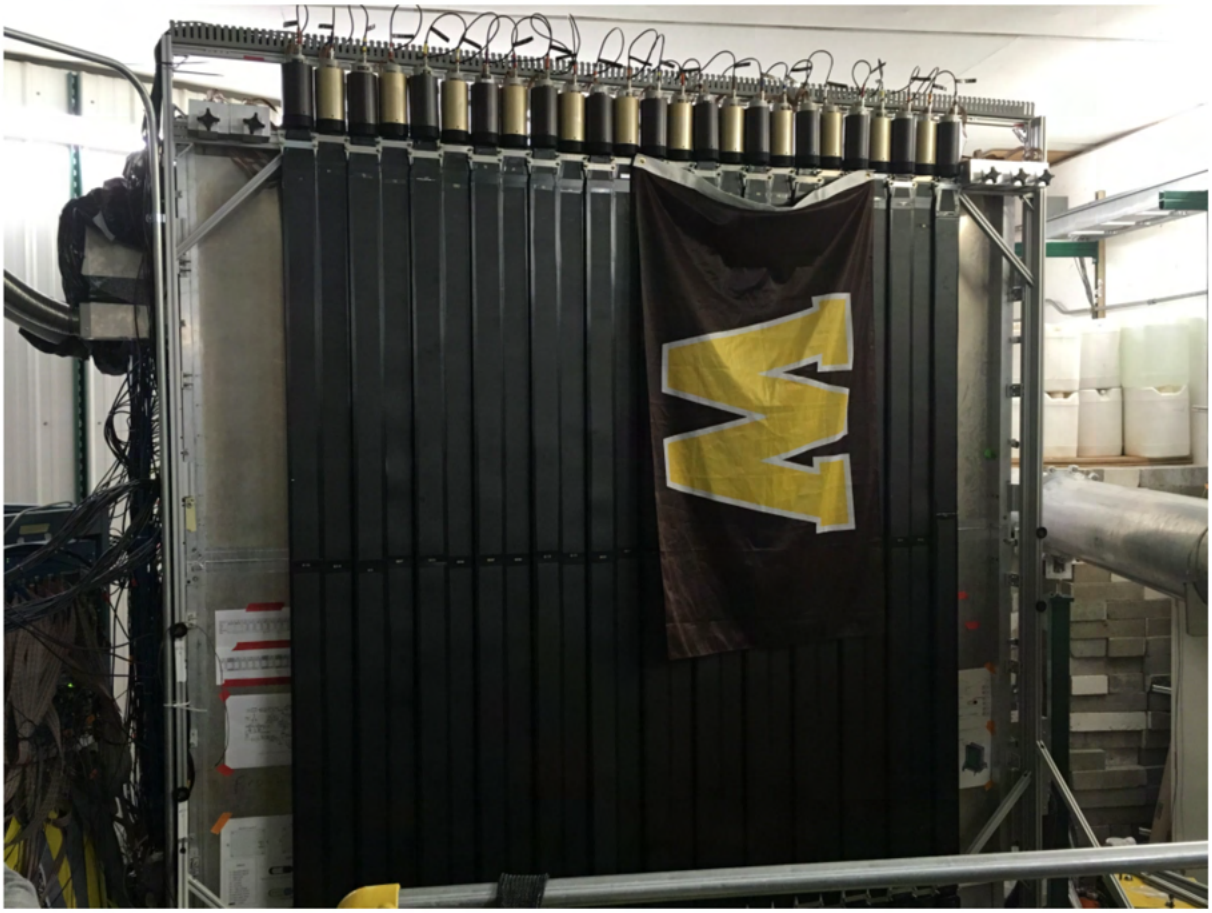

Figure 4.12: Completely constructed Veto Wall.

There were 25 bars mounted on the veto wall stand and was placed in front of the LANA during the experiment. The Veto Wall stand was constructed using aluminum T-slotted frames. It was light in weight and easily portable. The frame of the stand, when assemble before the LANA, was not shadowing the LANA. That stand was good to carry the weight of all the Veto Wall detectors including cable runners and SHV cables. Once the construction and testing of all 25 bars was completed, these bars were moved to NSCL and installed in the frame in front of the Neutron Wall. A complete Veto Wall used in the experiment is shown in Figure 4.12.

The data acquisition circuit diagram for the Veto Wall is shown in Figure 4.13. The

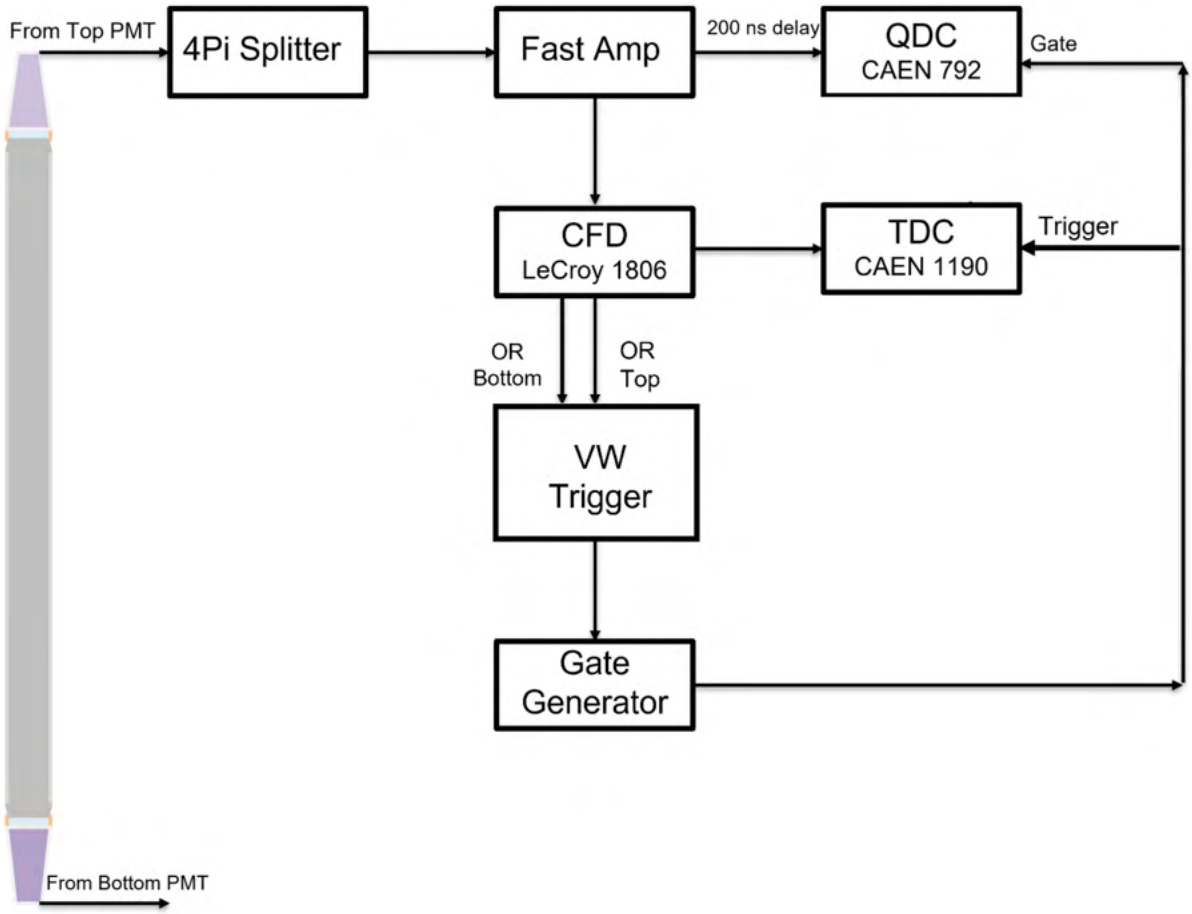

Figure 4.13: Flowchart of data acquisition for the Veto Wall.

setup of DAQ during the calibration of each bar is similar to what was used in the actual experiment. High Voltage is supplied to the PMT through SHV cable and anode and dynode signals from PMT travel through the same cable to 4 Pi splitter. The anode signal

is the negative voltage pulse used to produced charge signals (QDC signals). One of the signals from 4 Pi splitter is sent to CAEN 792 charge to digital converter (QDC) [95] after amplifying it using NSCL Fast Amp module and delaying it by about 200 ns. QDC integrates the total charge and digitizes it. Another copy of the same signal is used to generate gates for QDC module using the Lecroy 1806 constant fraction discriminator (CFD). Signal is recorded by the QDC if it is within the gate. A trigger for the signal to be recorded at QDC is set up from the coincidence of top and bottom signals of PMTs from CFD and the master trigger was produced by the signal from the LANA. Times were recorded by CAEN 1190 time-to-digital converter (TDC) [96].

4.3 Calibration of the Veto Wall

4.3.1 Energy Calibration

^{60}Co source was used to perform the energy calibration of the Veto Wall bars. When

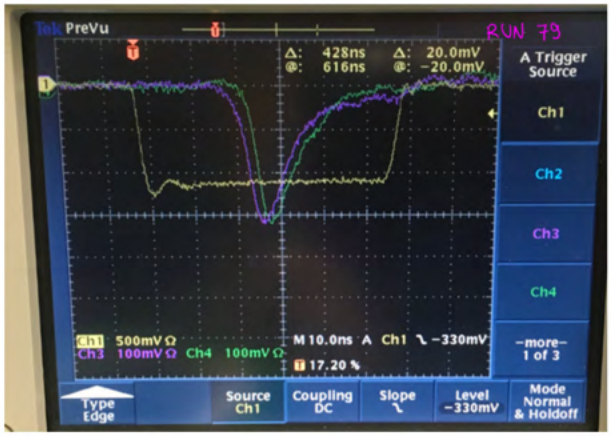

Figure 4.14: Gamma signals from two PMTs as seen at oscilloscope.

the source is kept in the middle of the bar, both top and bottom PMTs receive signal of equal strength. Figure 4.14 shows such signals. Gamma ray from the source undergoes Compton scattering from the detector materials so we used Compton kinematics for the

energy calibration. The energy of scattered photon is given by the following equation:

$$E_1 = E_0 \frac{m_e c^2}{m_e c^2 + E_0(1 - cos\theta)}, \tag{4.1}$$

where E_1 is energy of scattered photons, E_0 is initial energy of photons , m_e electron rest mass, c is velocity of light and θ angle between incident and scattered photons. When θ is 180, E_1 is minimum and (E_0 - E_1) is maximum that is the maximum energy is deposited by an incident photon to the detector material. This energy corresponds to the Compton edge energy. Compton edge(CE) at maximum scattering angle is calculated by

$$CE = E_\gamma \frac{2E_\gamma}{m_e c^2 + 2E_\gamma} \tag{4.2}$$

E_γ is incident gamma photon energy [97]. Our Energy calibration started with the position dependence of the geometric mean using gamma source. We studied the position dependent geometric mean and calculated the energy deposited by an incident particle using the following equation:

$$E = \frac{CE}{a \cdot pos + b} \cdot GM, \tag{4.3}$$

where GM is a geometric mean of the charge signals from the top and the bottom PMTs, pos is the position of the hit of particle on VW, a is a slope of the energy calibration and b is an offset of the energy calibration as a function of position. Figure 4.15 shows the method we used to determine the Compton edge at each source position of the detector. The top panel of the Figure 4.15 shows the integrated charge signal from the top PMT which is labeled as "q top", the middle panel shows such signal from the bottom PMT which is labeled as "q bottom" and the bottom panel shows the geometric mean of the charge signals from both PMTs of the same detector. The edge of the geometric mean is fitted with the Gaussian distribution to calculate the Compton edge. Red line on the bottom panel shows such fit.

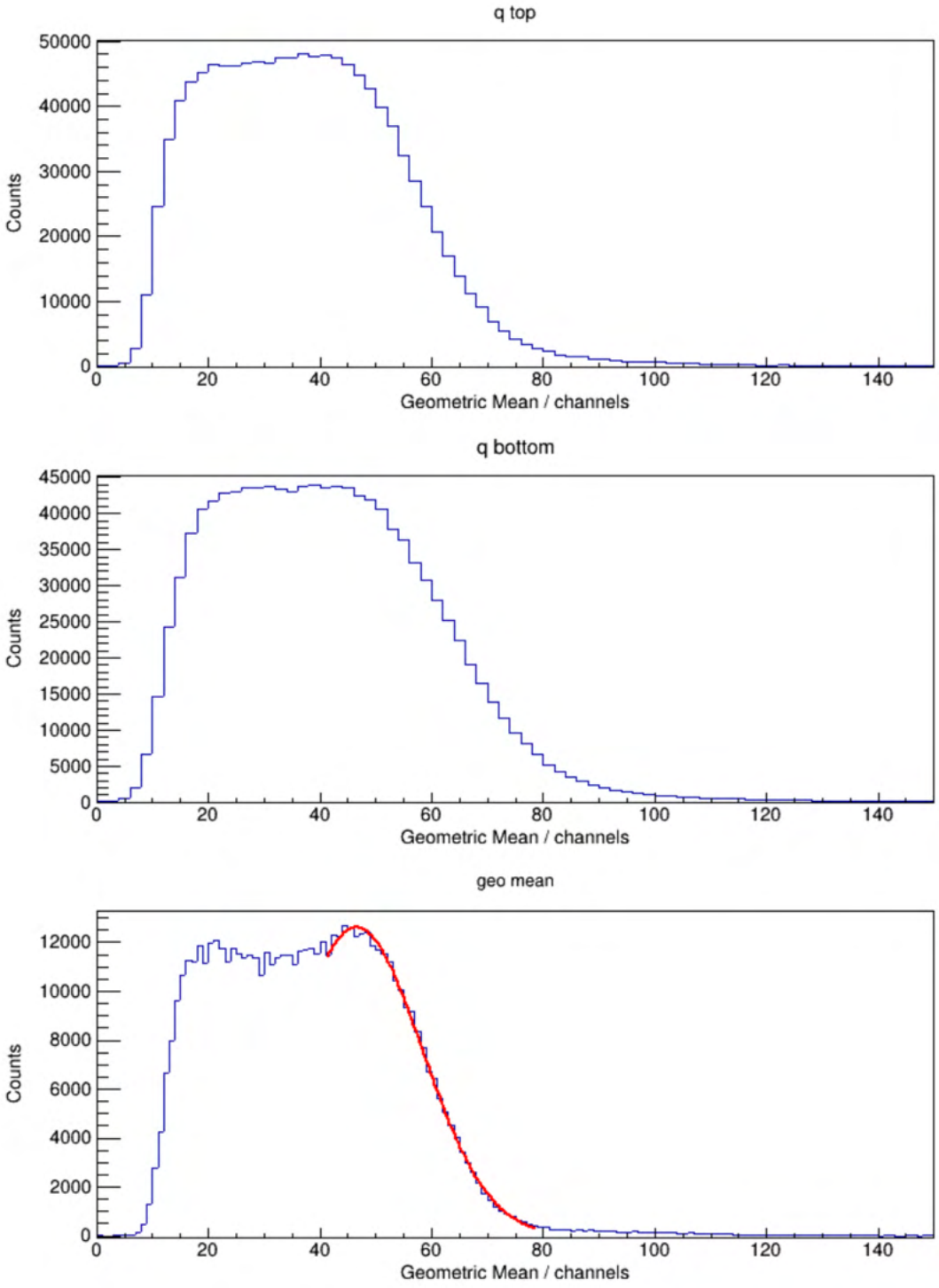

Figure 4.15: Compton edge fit for bar 20 gamma source at center.

For each Veto Wall bar we used Cobalt 60 gamma source to determine the Compton edge at different positions. All the positions along the bar were measured with respect to the Top PMT and offsets were adjusted. We plotted CE vs distance and fitted linearly to

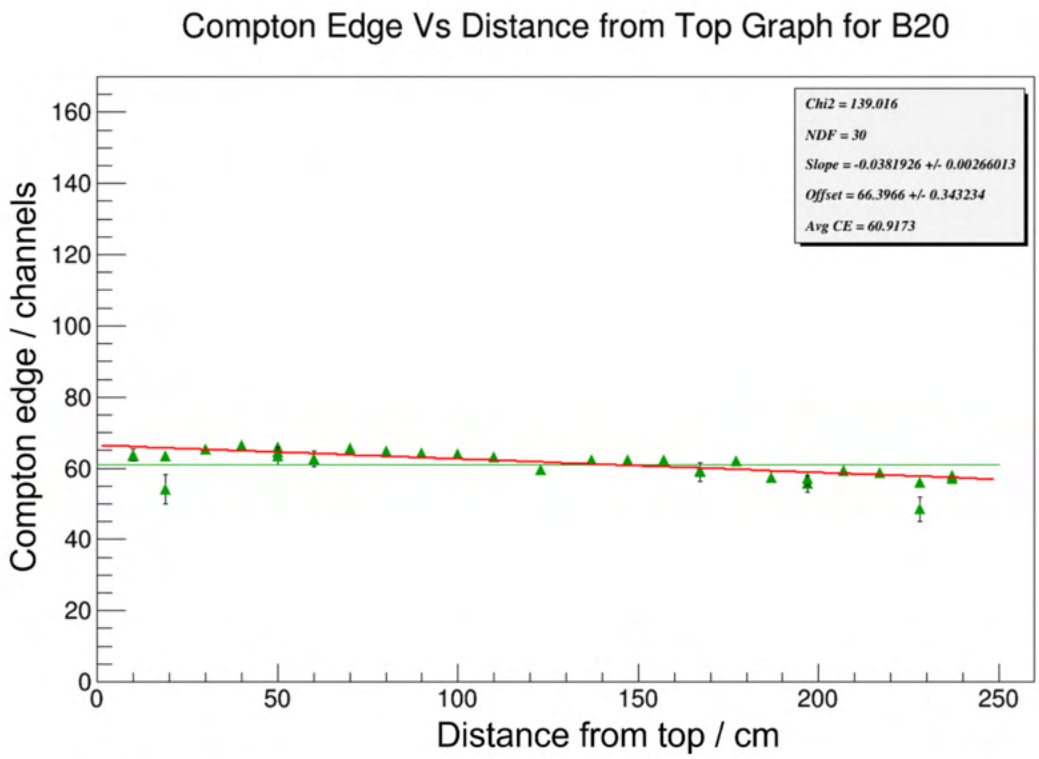

Figure 4.16: A plot of Compton edge Vs distance for bar 20.

obtain the slope and offset. Figure 4.16 shows an example of such plot for one detector. In Figure 4.16, data (Compton edge), represented by green triangles are not flat along the bar, this suggest that our energy calibration is position dependent.

We used 2 % of CE in error bar in order to account the fluctuations of CE with fit parameters. Using the calibration parameters slope and offset, energy deposited histograms for each detector is shown on following 1D and 2D plots. These histograms were obtained for (Ca48, Ni64) system at 140 MeV/A beam energy when shadow bars were removed. In Figure 4.18, there are only 20 detectors as left three detectors and right two detectors cover the PMTs of the Neutron Wall bars so they are not used in analysis. Figure 4.17 is two dimensional histogram of an energy lost by charged particles in each detector. X-axis represents the detector numbers ranked from left to right of the Veto Wall (right side being the closer to the downstream of the beam) and y-axis is the energy loss in these detectors. Figure 4.18 shows the one dimension histogram of energy loss. These both figures show our energy calibration when applied to our data.

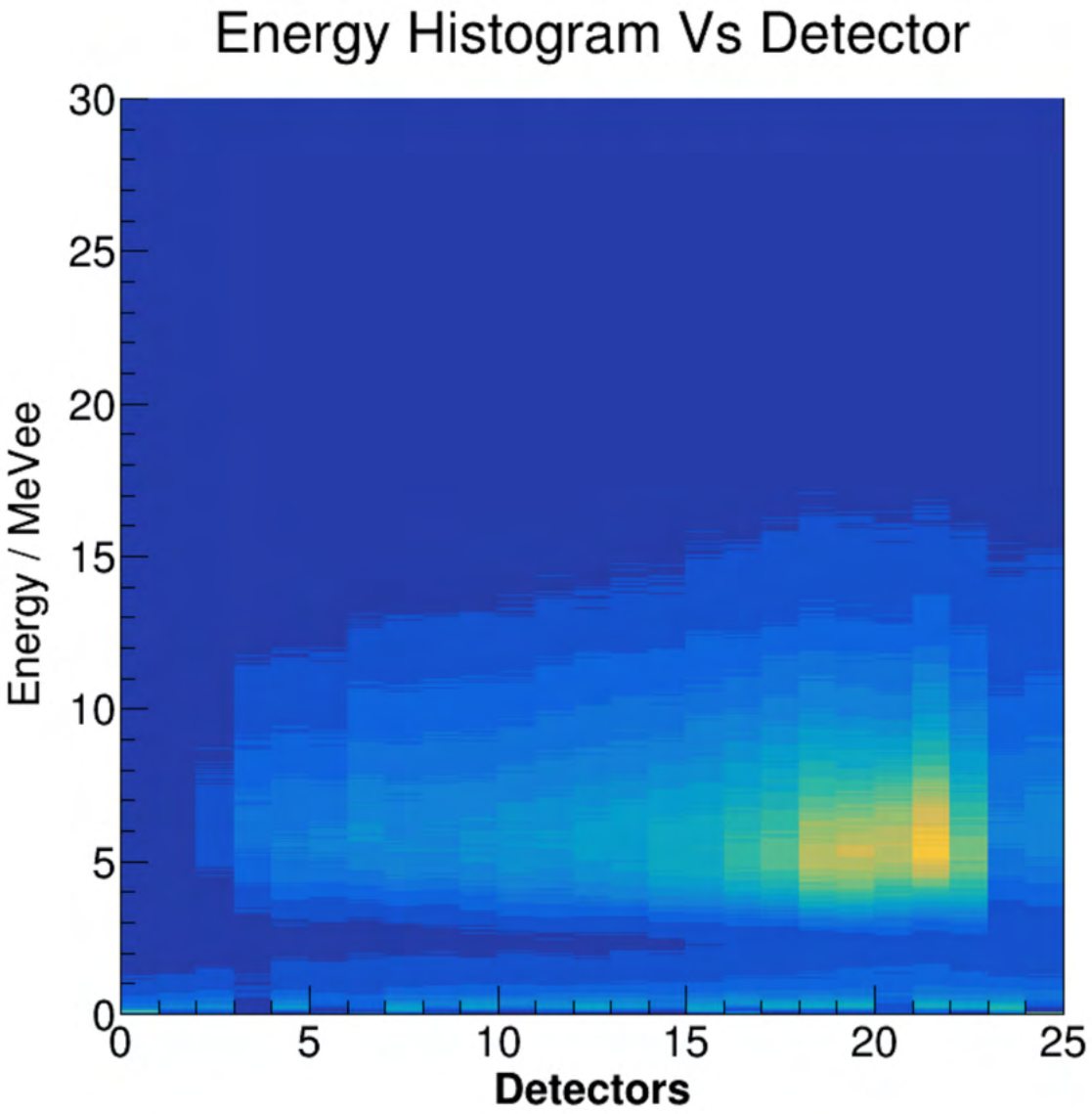

Figure 4.17: Two dimensional histograms of energy deposited with respect to detectors.

4.3.2 Position Calibration

The time difference is calculated from the time signals from the top and bottom PMTs. That time difference is related to the position along the detector. Light produced in the detector takes about 1 ns to travel a distance of 7cm along the scintillator. If a particle hits the detector at the center, light produced at that point will take the same time to reach the top and bottom PMTs respectively.

The time difference histogram was fitted with Gaussian distribution to calculate the

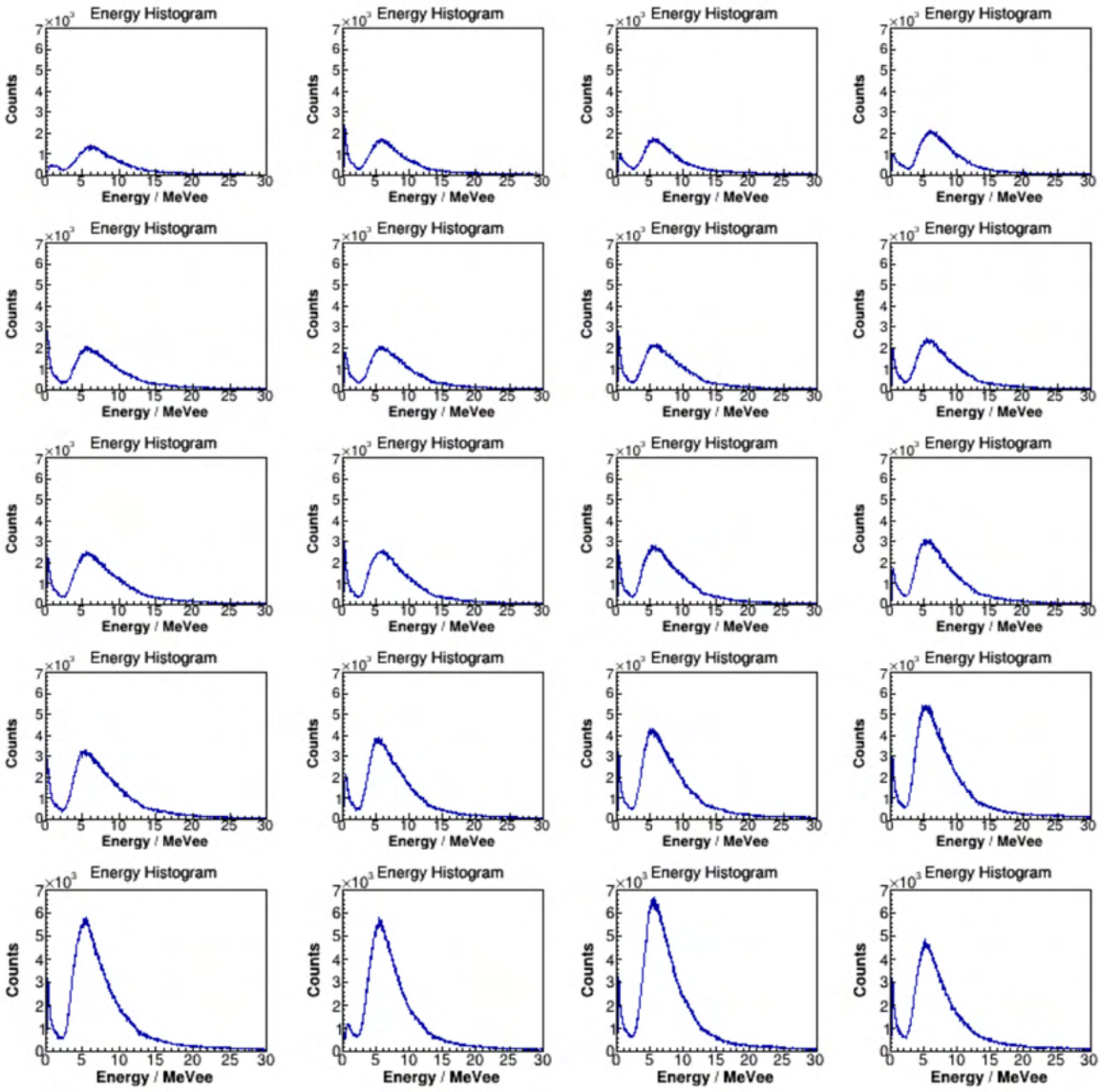

Figure 4.18: One dimensional energy deposited histograms of the detectors.

average time difference. A plot of such a time difference vs the location of the source along the detector was drawn and fitted using a linear function to get the slope and the offset. These slopes and offsets are the position calibrating parameters of each detector. Figure 4.20 shows such a plot with corresponding fits. The red line in Figure 4.20 is the fit with free parameters while the blue line is the fit with the slope being fixed. Both of the fits show almost identical offsets. Using the fitted parameters and time difference,

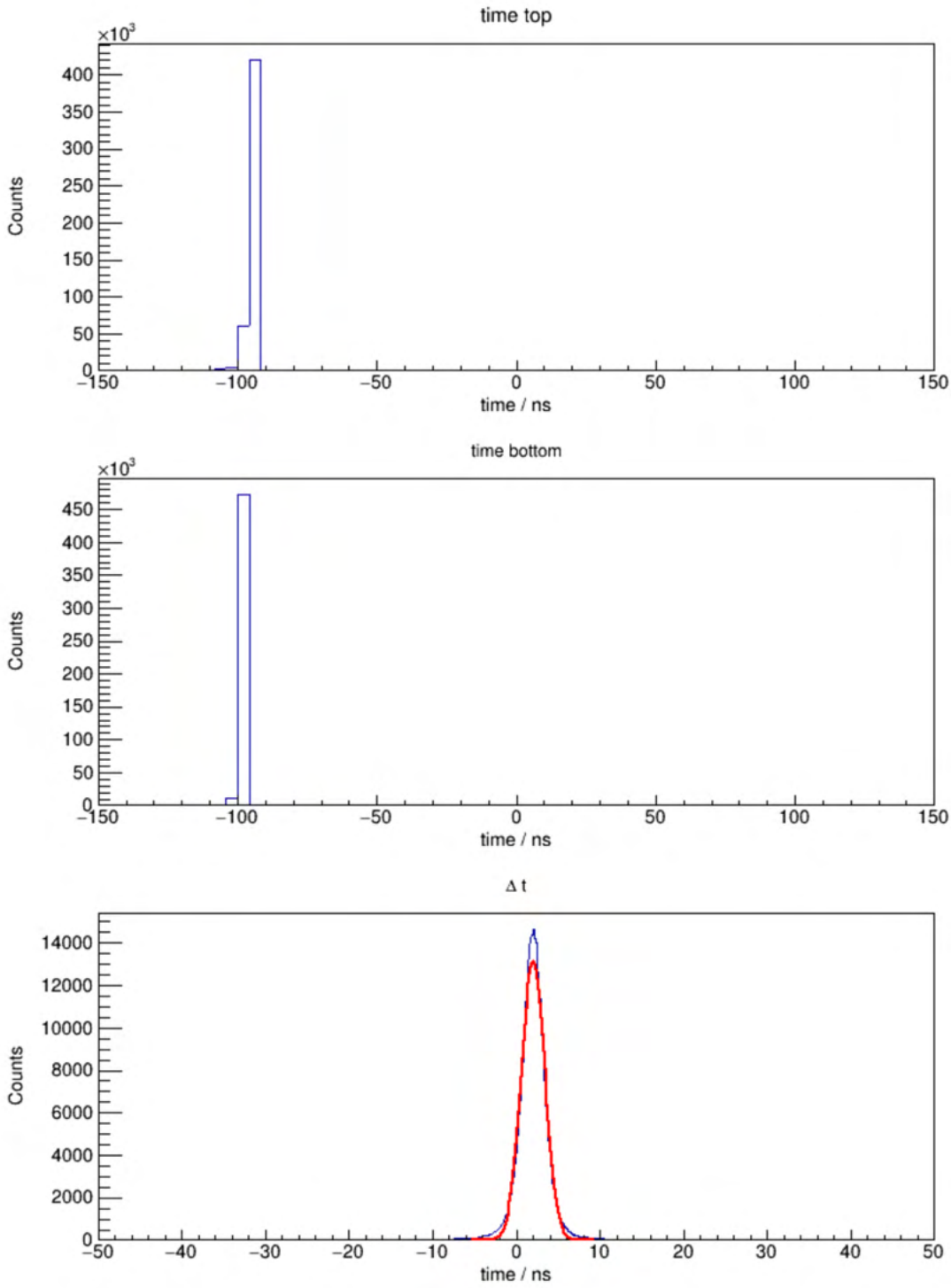

Figure 4.19: Times from the top and bottom PMT with Gaussian fit applied to time difference between these two times.

the position of hit in the Veto Wall is calculated by using following equation:

$$x = m \cdot \Delta t + c \tag{4.4}$$

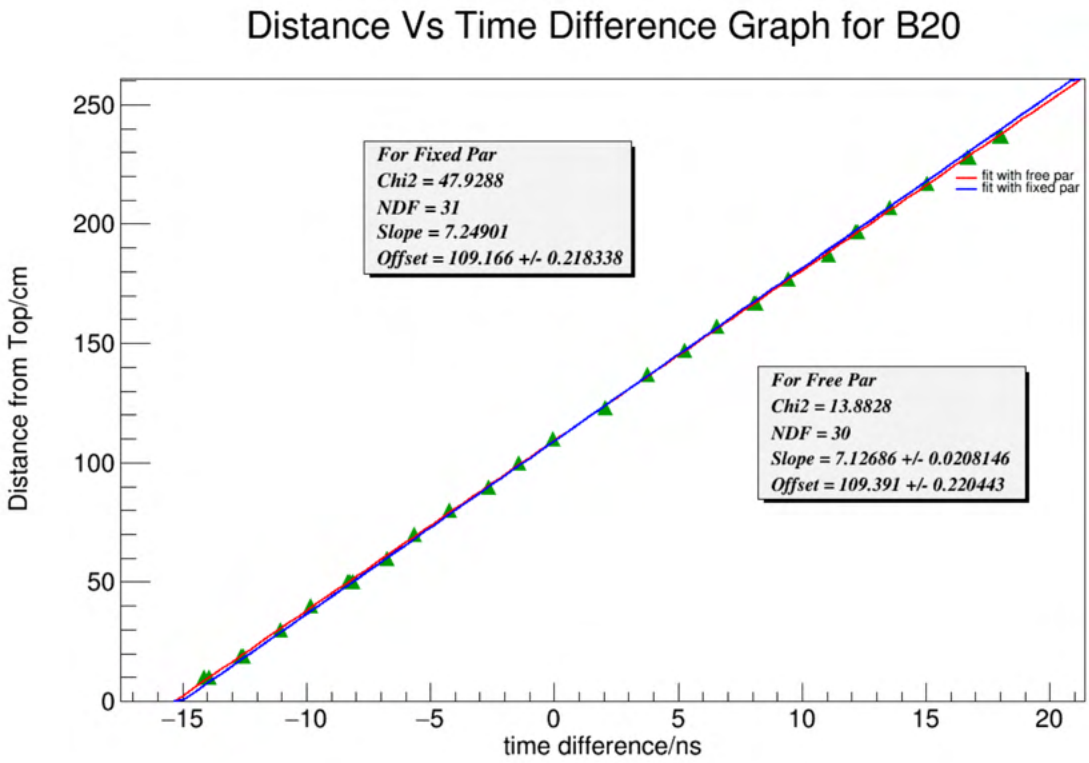

Figure 4.20: A plot of time difference vs distance of source.

Here x is position of hit on VW, m is the slope of position calibration, Δt is time difference and c is the offset of position calibration.

In order to check the position calibration parameters for all the detectors, we used these parameters for the data to calculate the position of the hit in the Veto Wall bars by gating on one of the Neutron Wall. Figure 4.21 shows the results of that check. Top histogram of Figure 4.21 indicated that we required an adjustment of offsets. That histogram shows positions on each Veto Wall detector when gated on the Neutron Wall detector 11. We can see a clear shift of the position on several detectors. These shifts were seen due to the error in the global offsets of the position calibrations. Projection of this histogram for each detector gives one dimensional position histogram. That histogram was then fitted with Gaussian function and mean for each detector is noted. Taking mean of the detector 19 as reference, differences between the mean of all other detectors with the reference mean were taken and those differences were adjusted for the offsets of respective detectors. The bottom histogram of Figure 4.21 shows the position histogram with adjusted offsets

which is a straight line. This proves our offsets are now corrected.

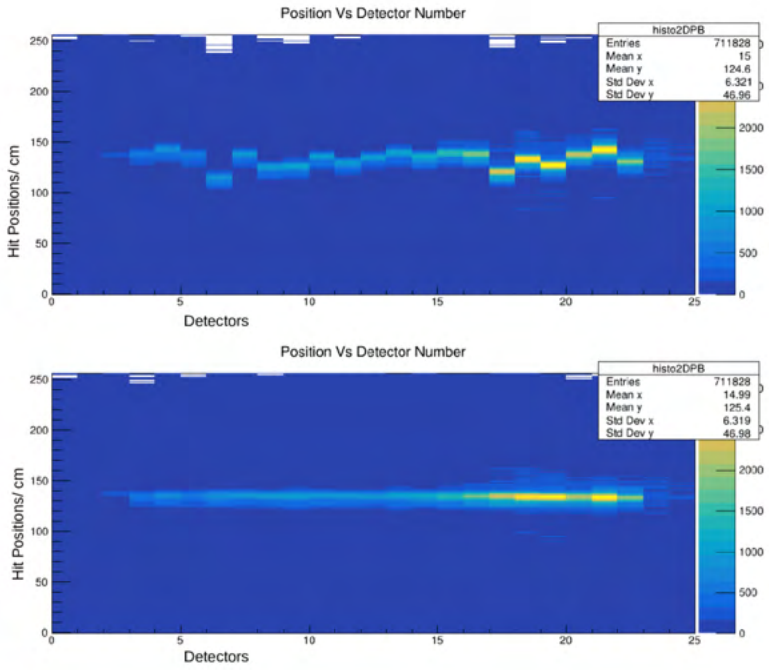

Figure 4.21: Two dimensional histogram of position of hit on the Veto Wall when gated on NW11 vs the Veto Wall Detectors.

4.3.3 Corrections to Position Calibration

In order to adjust the offsets of position calibrations, we plotted two dimensional histogram of position versus detector. Figure 4.22 shows one such plot where three LANA detectors on top, center and bottom are gated. We can see shifts in positions for some of the Veto Wall detectors lying at the extreme. Our different sets of position calibrations needed to be corrected because of the various changes during the experiment. Figure 4.22 shows position spectra for three different LANA (Neutron Wall) detectors- detector 3 (bottom), detector 11 (center) and detector 22 (top). Detector 11 lies close to the middle of the LANA and close to the height of reaction center so the spectra behaves flat and nice. As we move up and down from center position spectra for the LANA detectors should show somehow curve nature (curved down at top and curved up at bottom). In the top panel of Figure 4.22, there is a jump on the position spectra of NW3

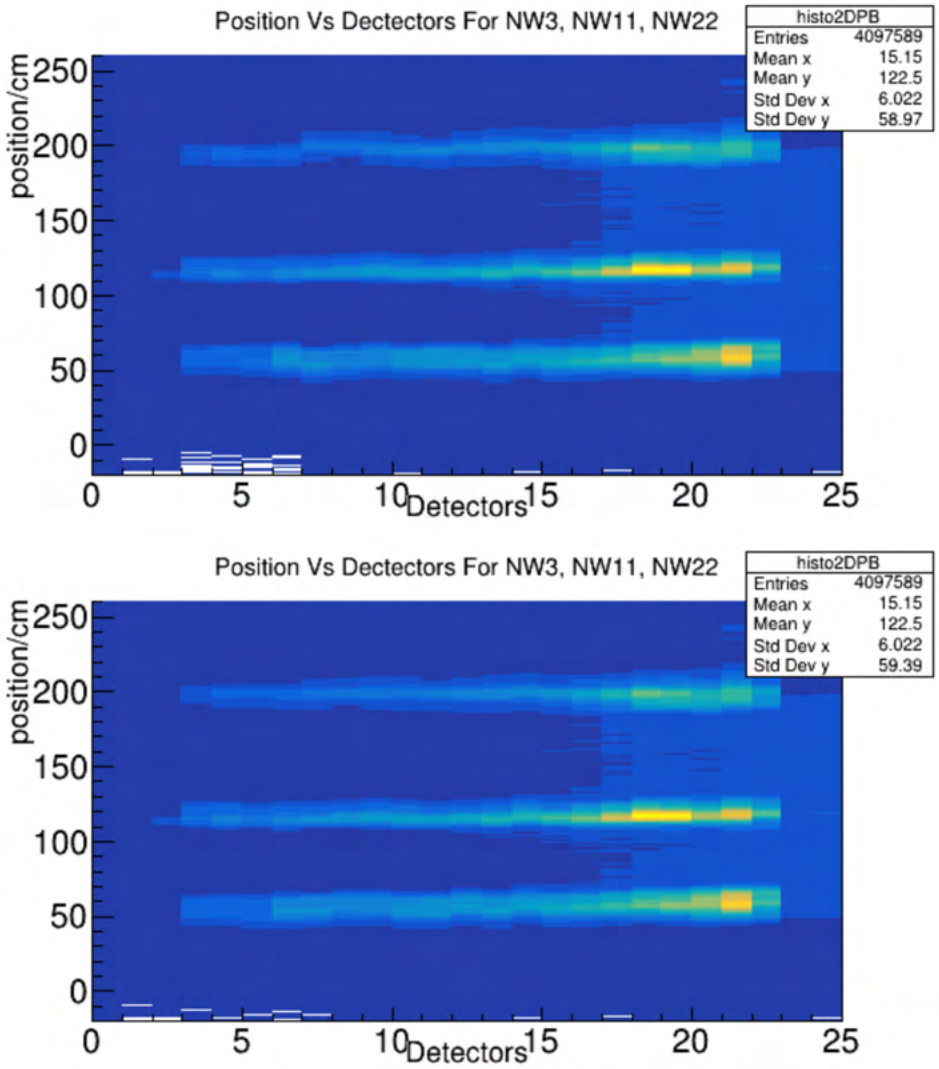

Figure 4.22: Position spectra of NW3,NW11, NW22 before (top) and after(bottom) correction.

and NW22 in moving from the Veto Wall detector 6 to detector 7. This jump is corrected in the bottom panel. To correct for such changes, we took the calibration parameters given by figure 4.20. Our input is a time difference and the output is a position. Reference detector position is taken either from NW3 or NW22. Corrected slopes and offsets are calculated using following equations:

$$a = \frac{p_r - p_w}{t_o - t_w} \tag{4.5}$$

$$b = p_w - a \cdot t_w, \tag{4.6}$$

where p_r is the position of the referred Veto Wall detector which is correct, p_w is the position of the second Veto Wall detector which needs to be corrected, t_o is a time difference of the second Veto Wall detector for NW 11, t_w is a time difference of the second Veto Wall detector for NW 3 or 22 whichever is taken as reference. Figure 4.23 shows the comparison of the position spectra for the Veto Wall detector 6 and 7 for NW3, NW11 and NW22. In the top panel of the Figure 4.23, the detector 6 (blue) and detector

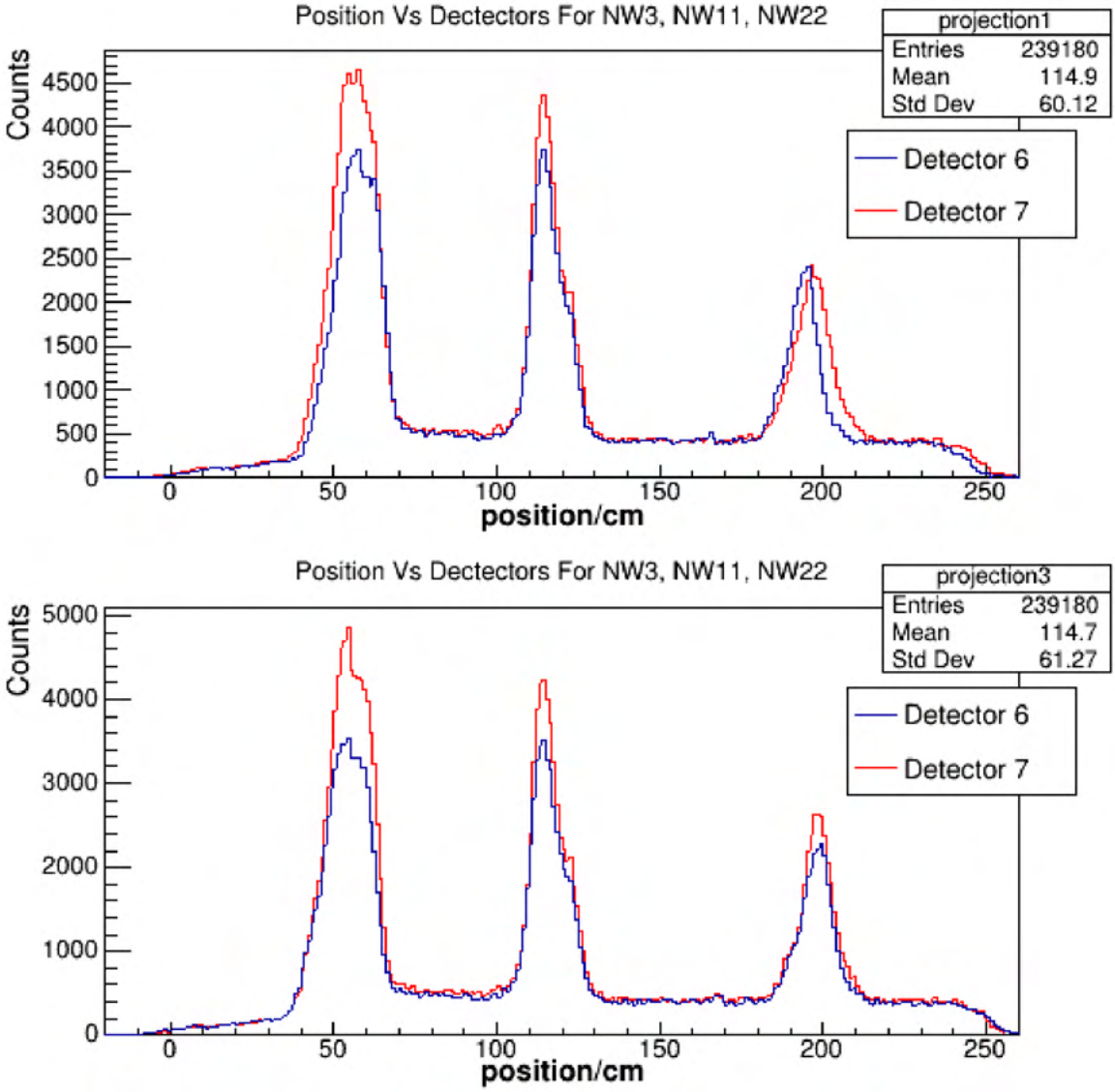

Figure 4.23: Position spectra compare for the Veto Wall detector 6 and detector 7 with reference to NW3, NW11, NW22.

7 (red) do not overlap for the Neutron Wall detector 3 (around 40cm -50cm) and the Neutron Wall detector 22 (around 190 cm to 210 cm). This is corrected in the bottom

panel which show good match between blue (detector 6) and red (detector 7) curves.

4.3.4 Corrections to Energy Calibration

We use the Veto Wall and the LANA detectors jointly for the analysis of charged particles and neutrons. The Veto Wall has the same coverage as the LANA. Typically twenty Veto Wall detectors are used for charged particles analysis while all LANA detectors are used for neutron analysis.

Incident particles deposit energy in the Veto Wall. Since the scintillating material of all the Veto Wall detectors is the same, energy spectra obtained from charged particles should be similar for all the Veto Wall detectors. If we have errors in energy calibrating parameters then the shapes of energy distributions of two adjacent detectors will show discrepancies. In that situation energy distributions should be scaled by some scaling parameters to fix the calibrations. Such scaling parameters are obtained by using χ^2 minimization method.

We calculated the χ^2 value for different scaling factors. Our scaling factor varies from 0.9 to 1.1 with an increment of 0.01. The chi square is obtained by following equation:

$$\chi^2 = \frac{\sum(Y_1(E) - Y_2(kE))^2}{\sqrt{(Y_1(E))^2}} \tag{4.7}$$

$Y_1(E)$ is the number of counts for energy bin E for referred detector, $Y_2(kE)$ is the number of counts for energy bin kE where k is scaling factor for the detector which needs to be corrected. The scaling factor where the χ^2 is minimum is taken as correction factor for the energy spectrum.

Figure 4.24 shows the energy spectra of detector 11 and detector 12. The χ^2 value is minimum when scaling factor (k) is 0.99, so we use 0.99 to scale energy spectrum of detector 11 with respect to detector 12. We have

$$E = a \cdot GM \tag{4.8}$$

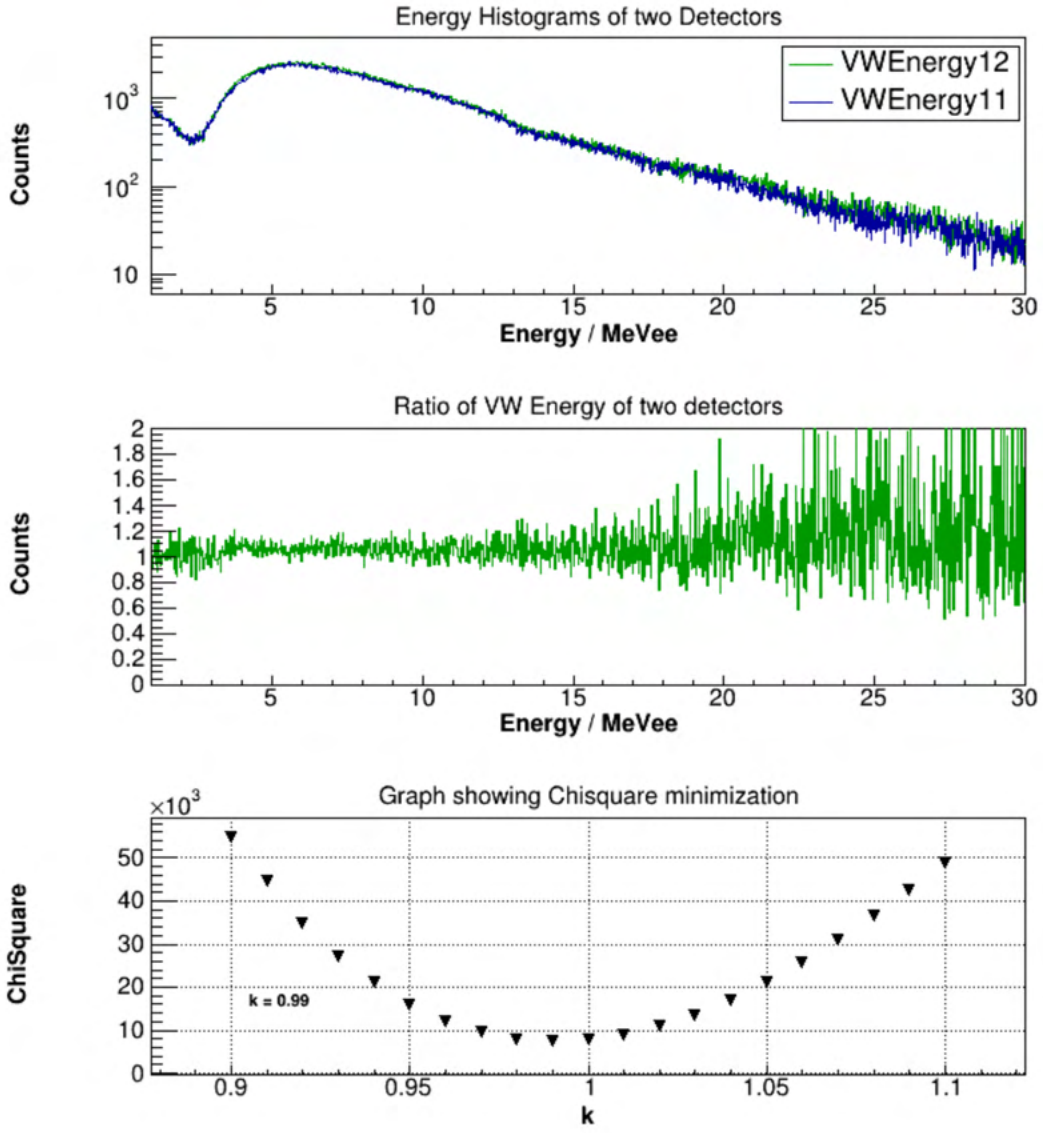

Figure 4.24: Calculation of scaling factor for detector 11 with respect to detector 12 using χ^2 minimization.

where E is energy, a is calibrating term GM is geometric mean. This a term is scaled by k determined from χ^2. The parametr a can be written as;

$$a = \frac{CE}{m \cdot pos + c}, \tag{4.9}$$

where CE a is Compton edge which is constant, pos is the position of hit on VW, m and c are the slope and the offset of energy calibrations. This slope and offset are scaled with k. Middle panel of Figure 4.24 shows the ratio of these energy spectra. The ratio is flat

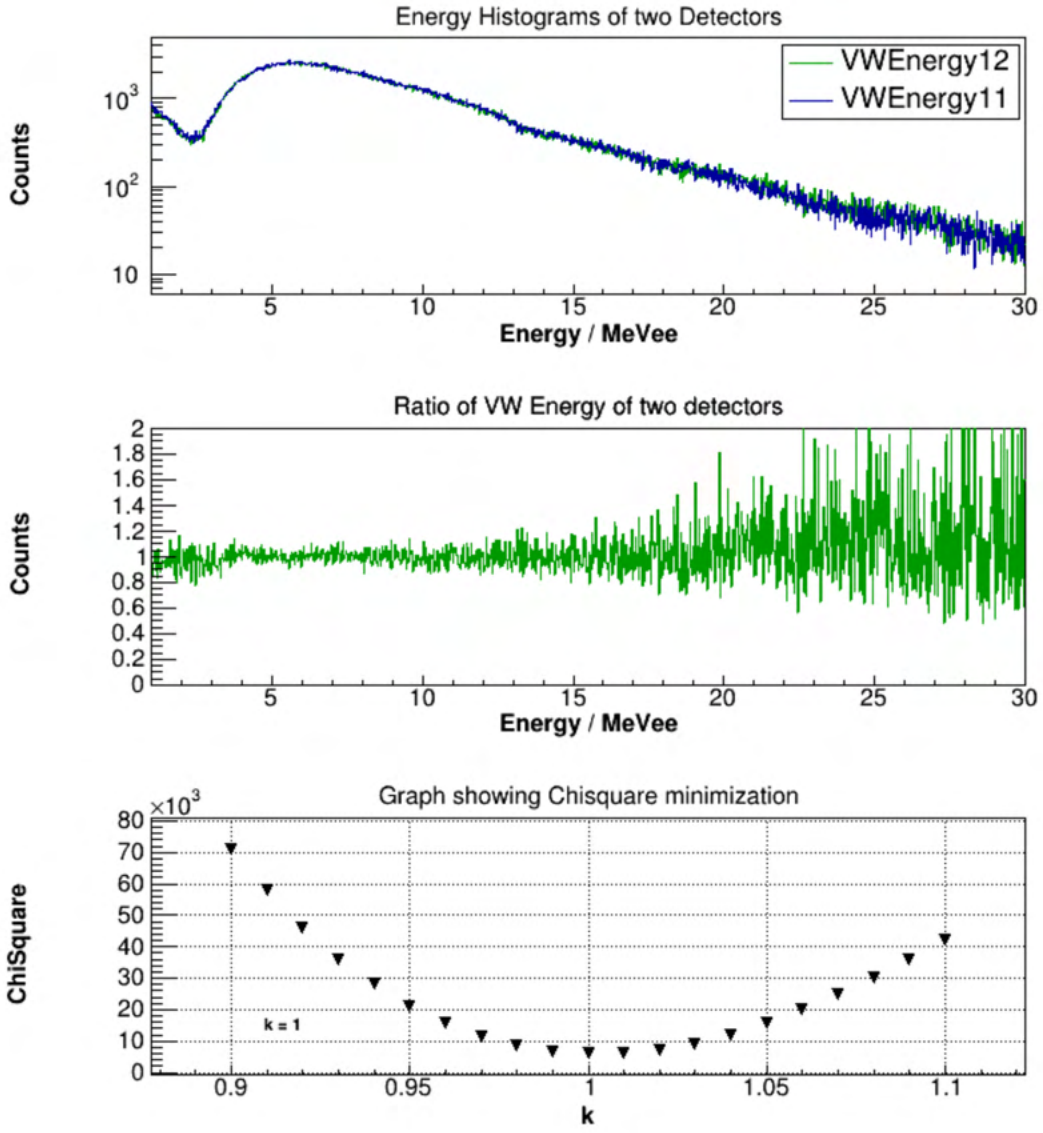

Figure 4.25: Check of energy histogram for detector 11 with respect to 12 after applying scaling factor calculated from χ^2 minimization.

within the error bars. After applying 0.99 scaling factor to energy spectrum of detector 11, we plot the energy spectrum for detector 11 and detector 12, their ratio and the value of χ^2 vs k in Figure 4.25. We can see χ^2 is minimum for scaling factor of 1 which is as expected. We took detector 12 as our reference and adjusted the neighboring detector 13 with respect to detector 12. Once the energy spectrum of the detector 13 is adjusted, we took detector 13 as our new reference and adjusted detector 14 with respect to detector 13 repeating the same process. We used that method all the way up to detector 21 and

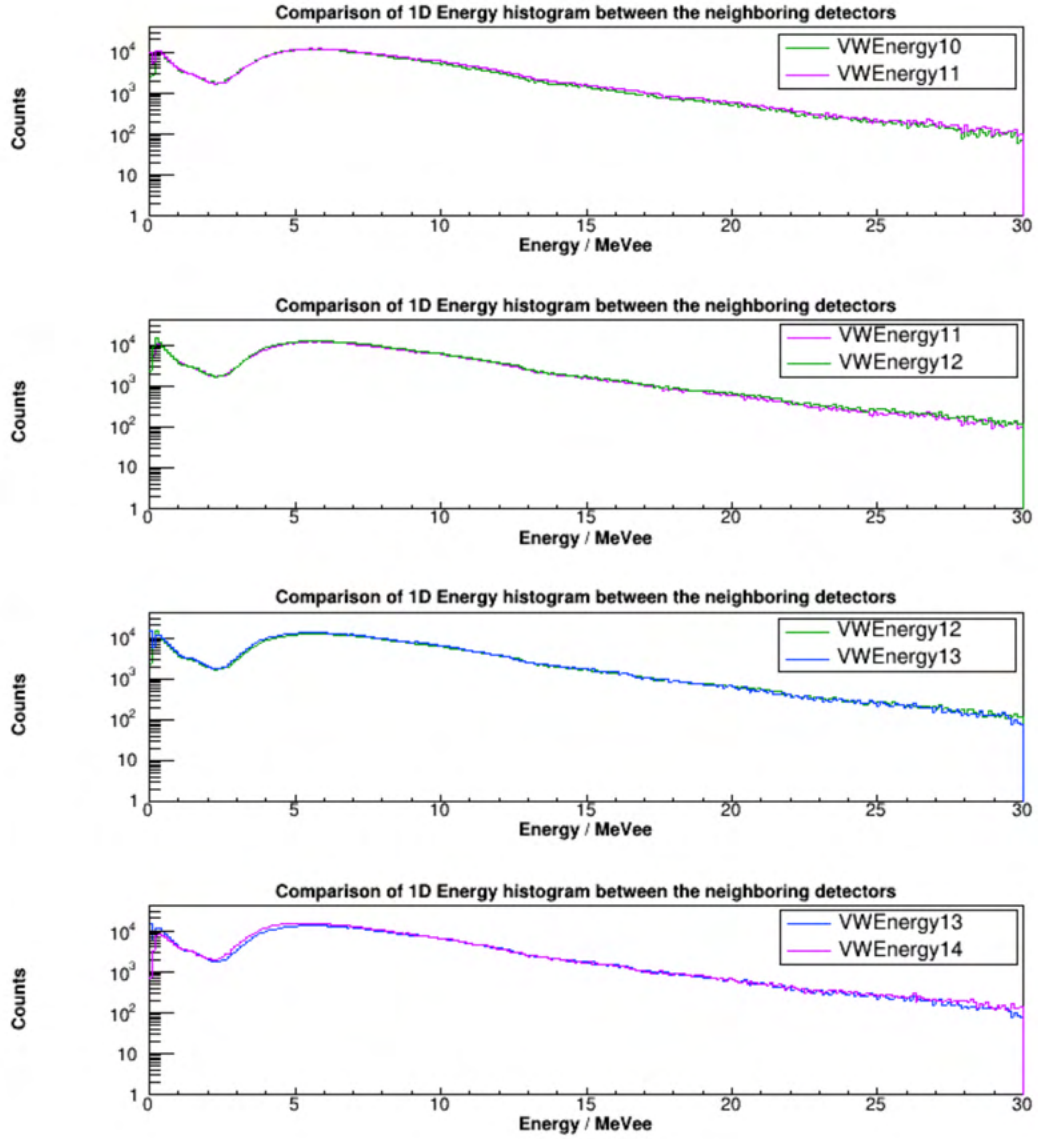

Figure 4.26: One dimensional energy comparison of the neighboring Veto Wall detectors.

down to detector 4. Figure 4.26 shows one dimensional corrected energy spectrum of some detectors.

4.4 Calculation of Threshold Energy

The Veto Wall detectors have the thresholds for the energies of charged particles that they can detect. The pedestal values (E=0) were determined by fitting the pedestal

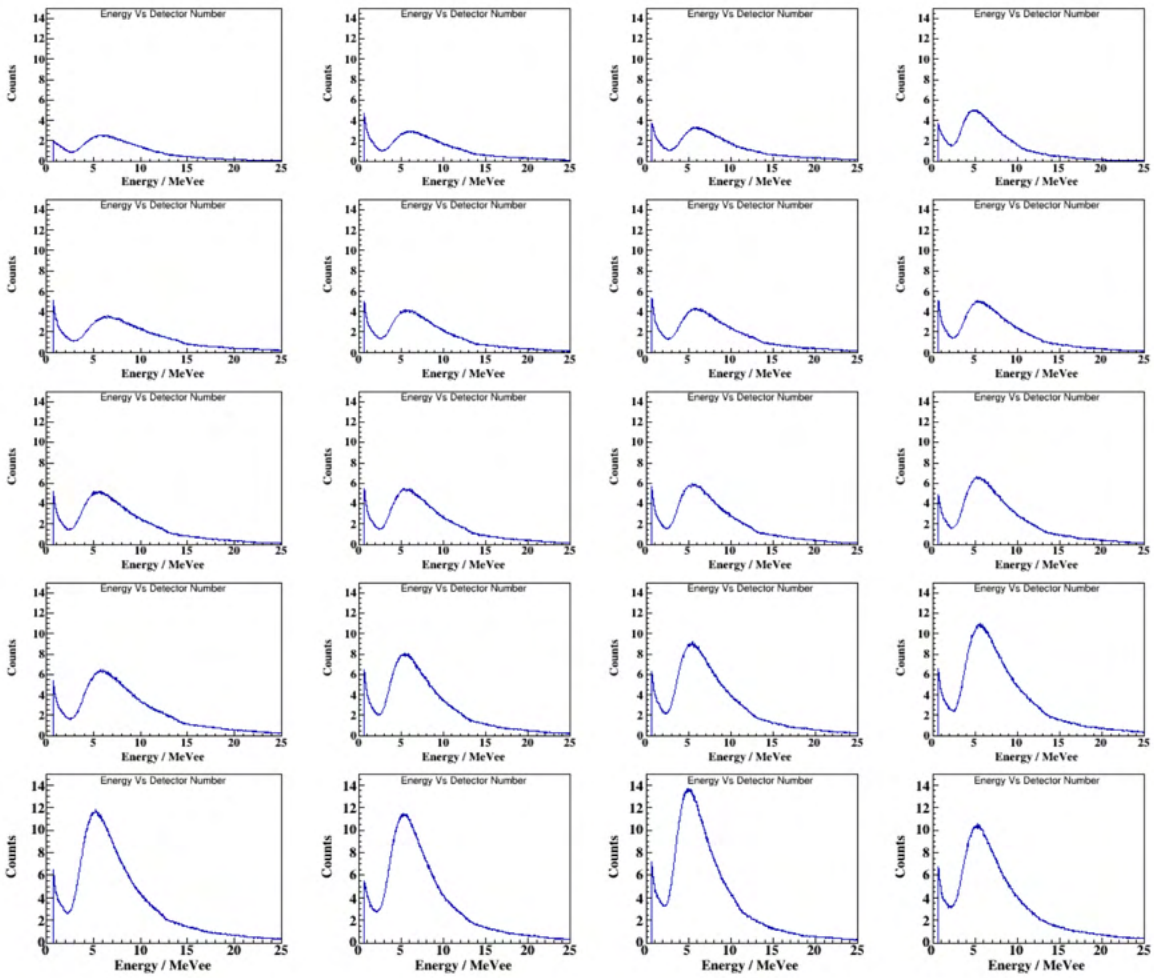

Figure 4.27: One dimensional energy histogram after apply energy threshold cutoff.

distribution with the Gaussian function and the mean of the fit was used as a pedestal. We aimed to find out the thresholds for all the detectors. For this we plotted one dimensional energy histograms for all the detectors and found the lower threshold values (minimum energy) for them. We found that different detectors have different thresholds. We came up with a common value of a threshold which agrees with all the detectors. This common value is 0.67 MeVee. A plot of energy histogram after implementing the threshold cut is shown in Figure 4.27.

4.5 Calculation of a Missing Charge Signal in One PMT

QDC is the term used for the charge-to-digital converter. When charged particles hit the scintillating material of the detector, light is produced. This light travels along the detector and is collected by the PMTs on both sides which is then multiplied and converted to the charge signal. This signal is recorded by the QDC module. In each detector, there are two PMTs (top and bottom) on either end of the detector. That charge is a function of various parameters. Charges at the top and the bottom PMTs are given by following equations:

$$Q_{top} = g_{top}\frac{N}{2}\exp\left\{-\frac{L/2 - X}{\lambda}\right\} \tag{4.10}$$

$$Q_{bottom} = g_{bottom}\frac{N}{2}\exp\left\{-\frac{L/2 + X}{\lambda}\right\} \tag{4.11}$$

g_{top} and g_{bottom} are the gain of the top and the bottom PMTs. N is number of photons produced by the charged particle. L is the length of the detector. X is the position of a hit on the detector. λ is the attenuation length of light response which is the length of scintillator that reduces the light by 1/e of its initial quantity [83]. Taking the ratio of above equations, we get

$$\ln\frac{Q_{top}}{Q_{bottom}}(X) = \frac{2}{\lambda}X + \ln\frac{g_{top}}{g_{bottom}} \tag{4.12}$$

This equation is in the form of

$$y = m \cdot X + c \tag{4.13}$$

where m $=\frac{2}{\lambda}$ is slope and

$$ln\frac{g_{top}}{g_{bottom}}$$

is the offset. If we know the slope and the offset then we can calculate Q_{top} and Q_{bottom}. Slope and offset were obtained by fitting the plot of ln $\frac{Q_{top}}{Q_{bottom}}$ vs position of the hit of the gamma source from the calibration data. Figure 4.28 shows one example of such plot for detector 19. Using Equation 4.14 and Equation 4.15, we can calculate Q_{top} and Q_{bottom}

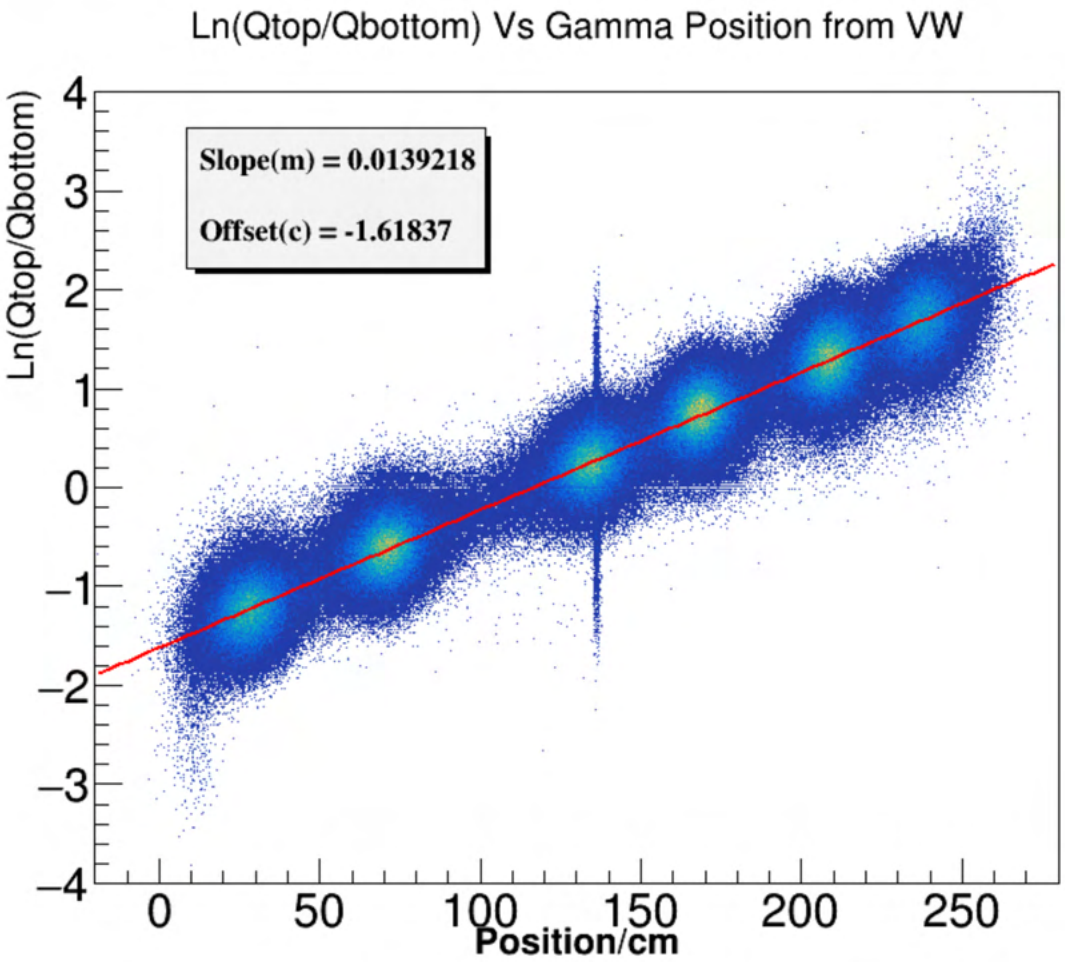

Figure 4.28: A plot of $Ln(Q_top/Q_bottom)$ vs position of gamma source.

as follows:

$$Q_{top} = Q_{bottom} \exp(mX + c) \tag{4.14}$$

$$Q_{bottom} = Q_{Top} \exp[-(mX + c)] \tag{4.15}$$

For any detector we can obtain the slope and the offset after fitting the data linearly as shown in Figure 4.28 and use these fitting parameters in Equation 4.14 or Equation 4.15 to calculate either Q_{top} or Q_{bottom} provided that we trust one of the QDC from data. This

is helpful to recover the lost qdc signal for the reasons like a loose cable connection, a high threshold values etc.

In order to validate equations 4.14 and 4.15, a check was done for the detector which has charge signals from both PMTs. We took calibrating gamma runs, plot the distributions as shown in Figure 4.28. We fitted that histogram with a linear function to obtain the slope and the offset. Similarly, we select one MeV particles, two MeV particles, all particles hitting the Veto Wall and all particles hitting the Neutron Wall B projected back on the Veto Wall. The histograms of $\ln \frac{Q_{top}}{Q_{bottom}}$ versus position for these different selections were fitted linearly to obtain slopes and offsets for different cases. We plotted the fit from gammas, 1 MeV particles, 2 MeV particles, all particles with the Veto Wall hit position and all particles with the Neutron Wall B hit position projected back on the Veto Wall. All these fits agree with the data. Such check is shown in Figure 4.29. Since this method was working for a good detector, we can adpot this method to recover the charge signals lost from one PMT due to various reasons like loose connections, broken cable, a high threshold of a QDC channel etc.

4.6 Energy and Position Comparison from the Veto Wall Versus LANA

If we miss/lose the time signal of the Veto Wall, we don't know the position of the hit along the detector. However, we may still be able to recover it. We can still calculate the energy deposited by particles at the Veto Wall from the energy calibration parameters and position. The only effort will be to project the hit position from the Neutron Wall back to the Veto Wall. We did such projections and calculated the Veto Wall hit position from the Neutron Wall hits. Of course, we applied angular correction back and forth and added a resolution of 7 cm. We plotted the Veto Wall position and the Neutron Wall position projection on the Veto Wall. We used these two positions to calculate the energy deposited by charged particles. Figures 4.30 and 4.31 show comparison of position and

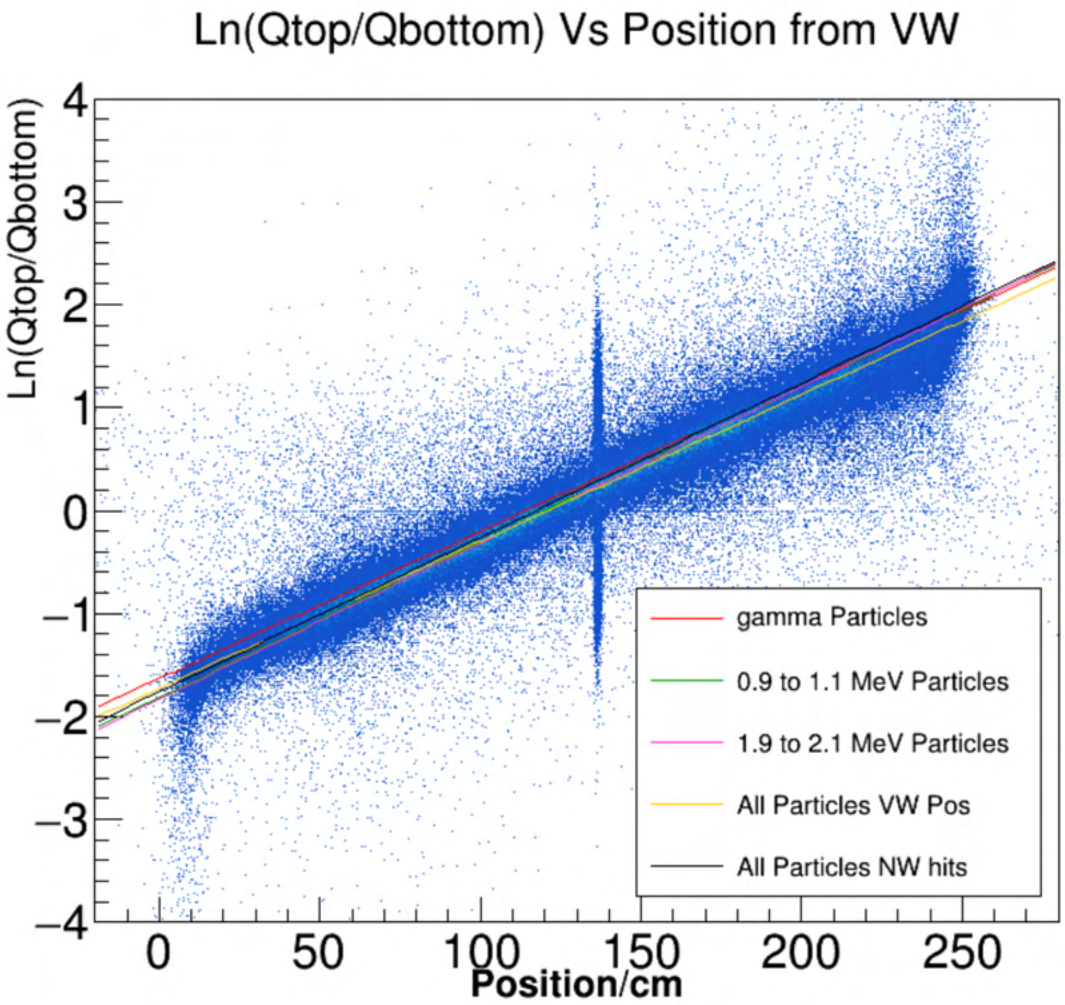

Figure 4.29: A comparison of the fit lines from different sources to data.

energy from these two methods.

Figure 4.30 shows the position of a hit on the Veto Wall by two different methods. Blue curves are the Veto Wall hit position obtained from the position calibration. Red curves are the projection of the Neutron Wall hits on the Veto Wall. If we know the Neutron Wall bar being hit, we can calculate the y- position of the hit with respect to the origin by using the height of the bar and by smearing data within the bar. That y position of the Neutron Wall is projected back to the y position on the Veto Wall by applying angular correction and position resolution. This y position is shown in red curves. We can clearly see the smearing effect.

Figure 4.31 shows the one dimension energy distributions in the Veto Wall. Blue curves

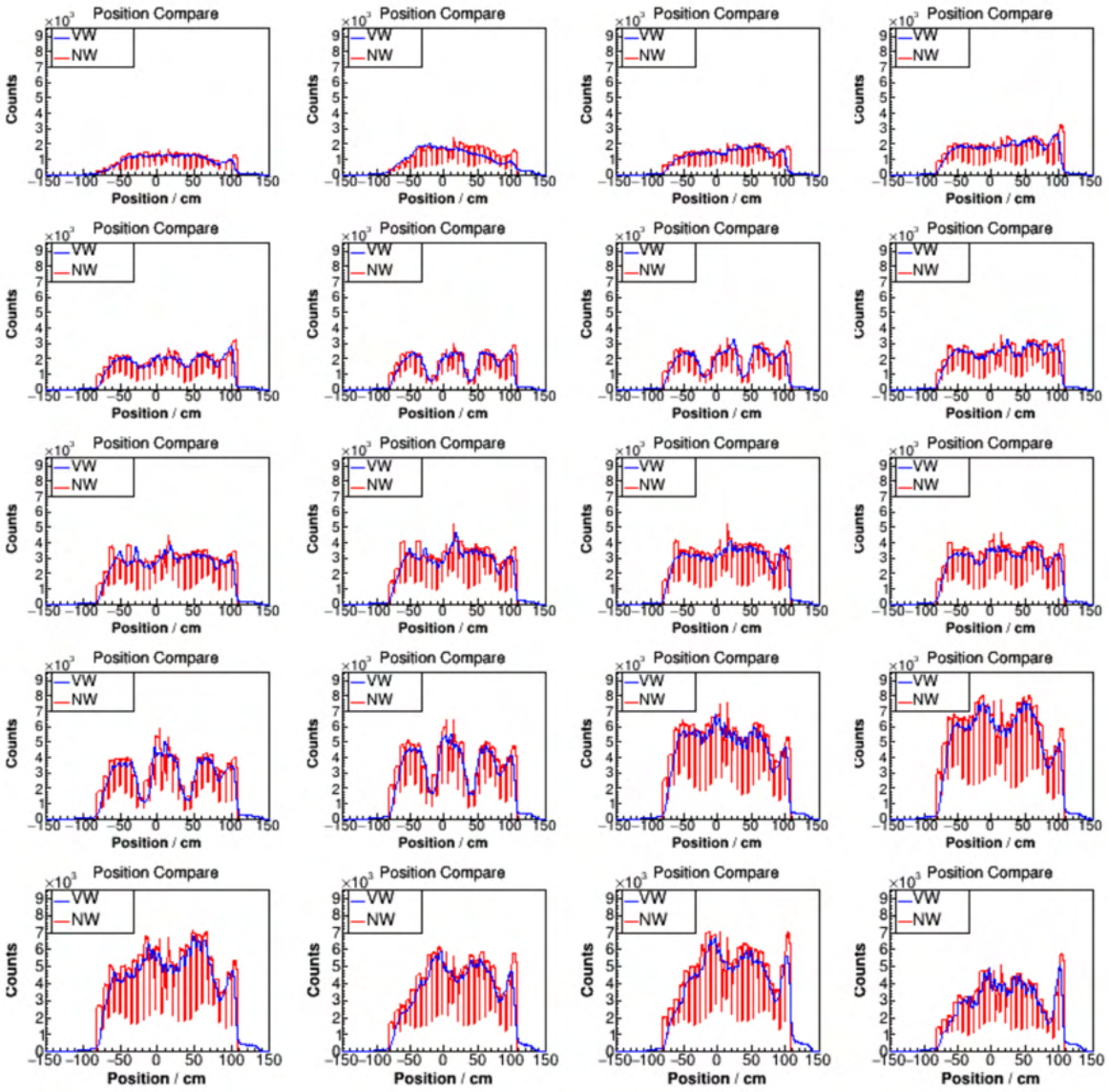

Figure 4.30: A comparison of the position histogram from the Veto Wall and position histogram projected from the Neutron Wall on the Veto Wall.

are the energy distributions obtained from the energy calibrating parameters and the Veto Wall hit position. Red curves are obtained from the energy calibrating parameters of the Veto Wall and the Neutron Wall hit positions projected back to the Veto Wall (red curves of figure Figure 4.30).

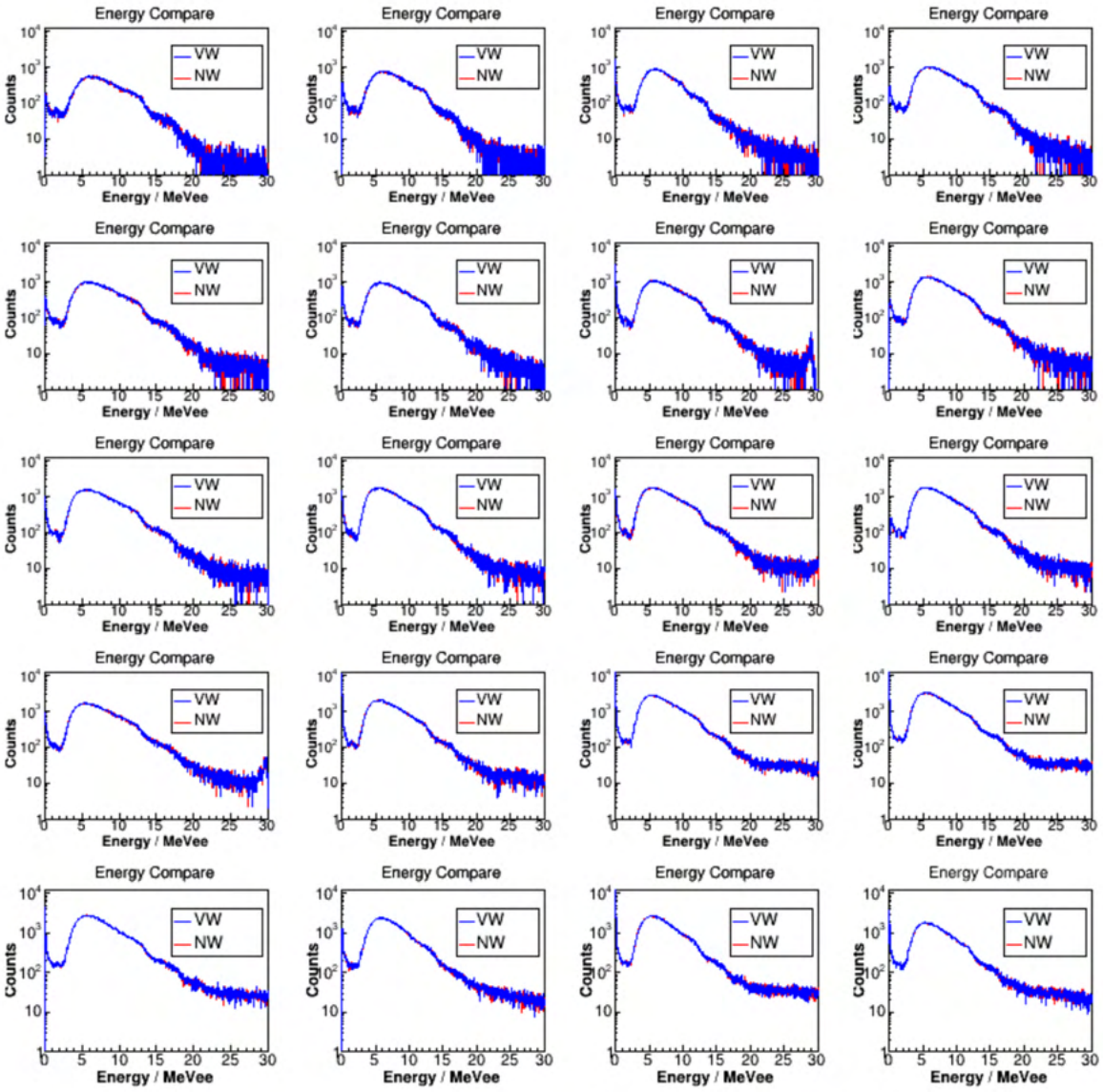

Figure 4.31: A comparison of energy from the Veto Wall position and the Neutron Wall position projection on the Veto Wall.

4.7 Energy Dependence on Position Calibration

Energy deposited by incident particle is given by equation 4.3 which shows a position dependence of the energy. Position-independent energy, which here is referred as an average energy is calculated by using following equation:

$$E_{avg} = \frac{CE}{b_{avg}} \cdot GM, \tag{4.16}$$

where b_{avg} is the average value of all Compton edges (refer to Figure 4.16 for Bar 20)

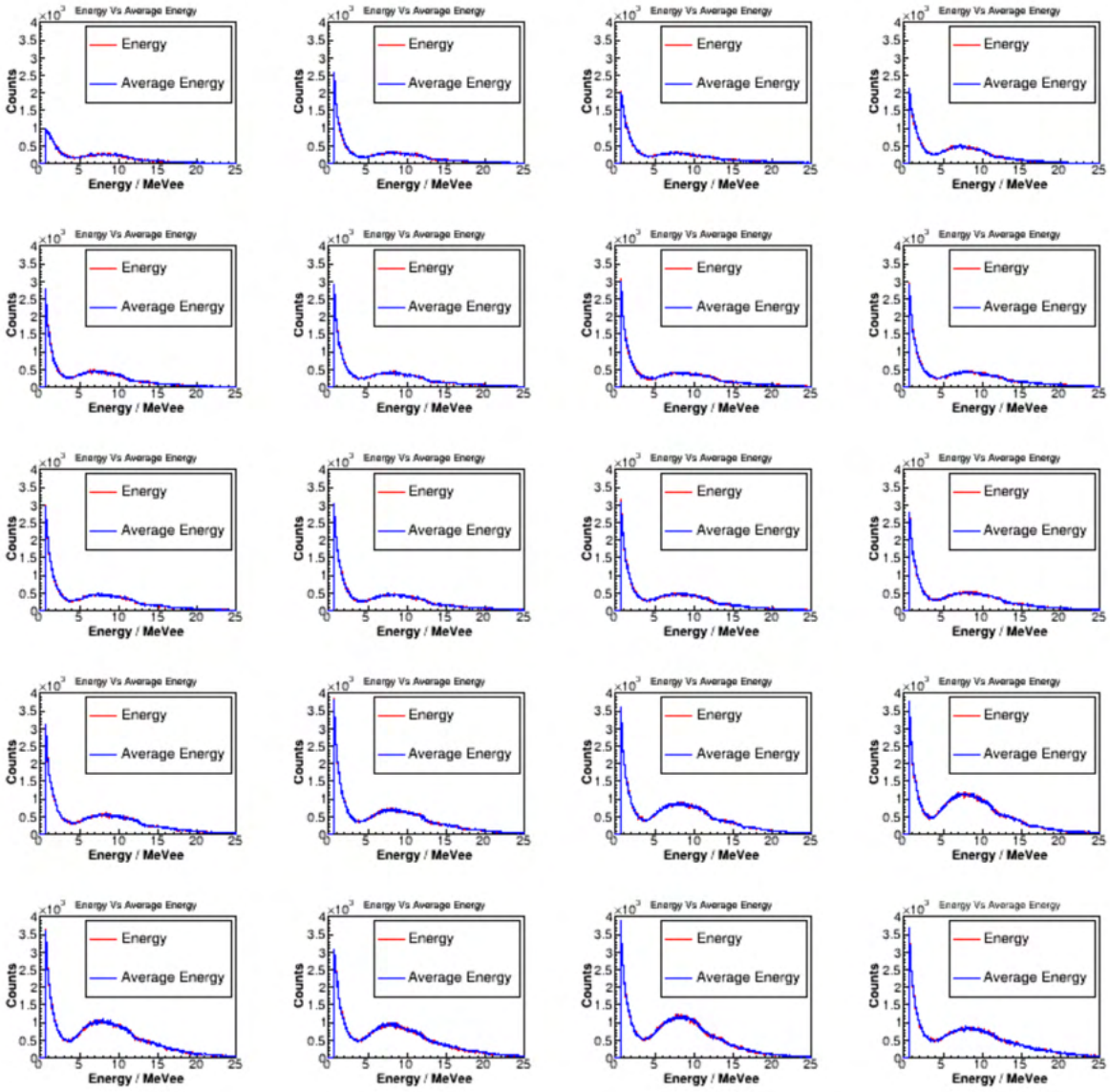

Figure 4.32: A comparison of energy vs average energy for all detectors of the Veto Wall.

Figure 4.32 shows the one dimensional energy histograms obtained by using Equation 4.3 (red plot) and Equation 4.16 (blue plot). Both distributions overlapped each other. This shows that if, for some reasons like a loose cable connection, we missed tdc signals and could not calculate the hit positions on the Veto Wall, we still are able to calculate the energy (blue one in Figure 4.32) which is not significantly different from the actual energy (red one in Figure 4.32).

4.8 Multiplicity

A hit in the Veto Wall requires time information from both PMTs of a detector, energy deposited in the Veto Wall greater than threshold value and a requirement of the Neutron Wall (only for vetoing charged particles). Average occupancy in the Veto Wall under these conditions was plotted in Figure 4.33. It shows maximum hits are on the detectors which lie closer to the beam. The multiplicity histogram is shown in the Figure 4.34. We excluded the zero multiplicity and only plot the multiplicities with greater than or equal to one in the plot. The average multiplicity is the average of the Figure 4.34

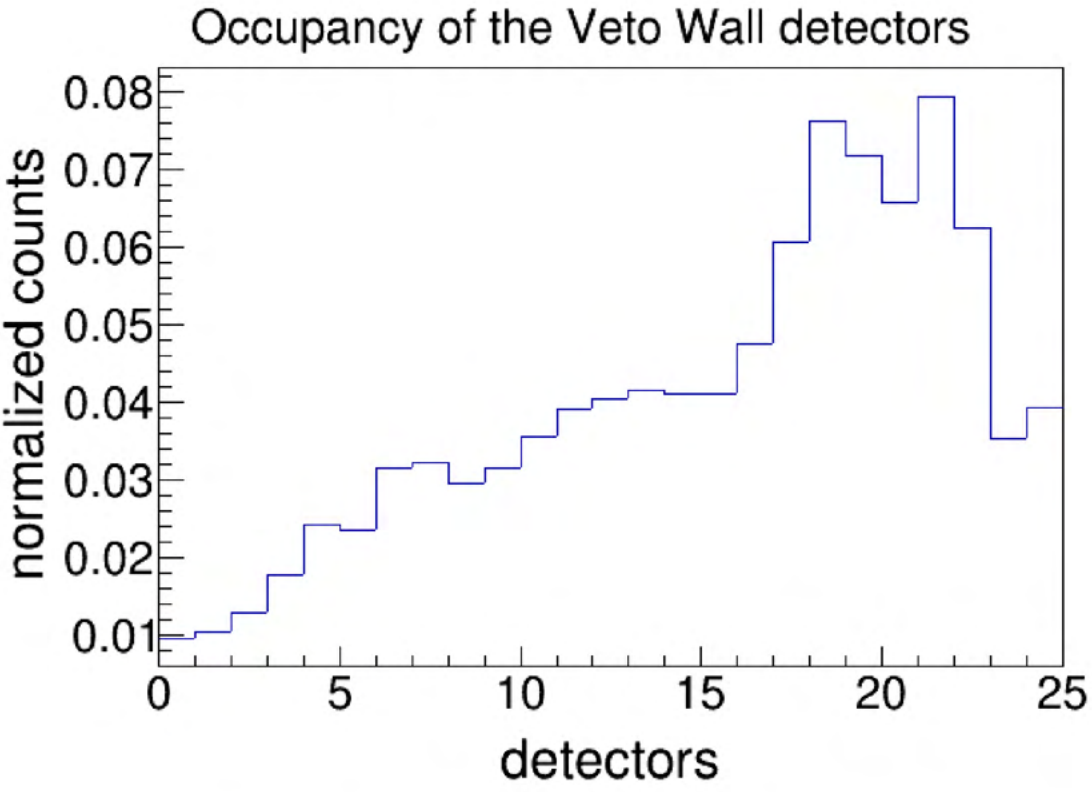

Figure 4.33: Average occupancy of the Veto Wall detectors.

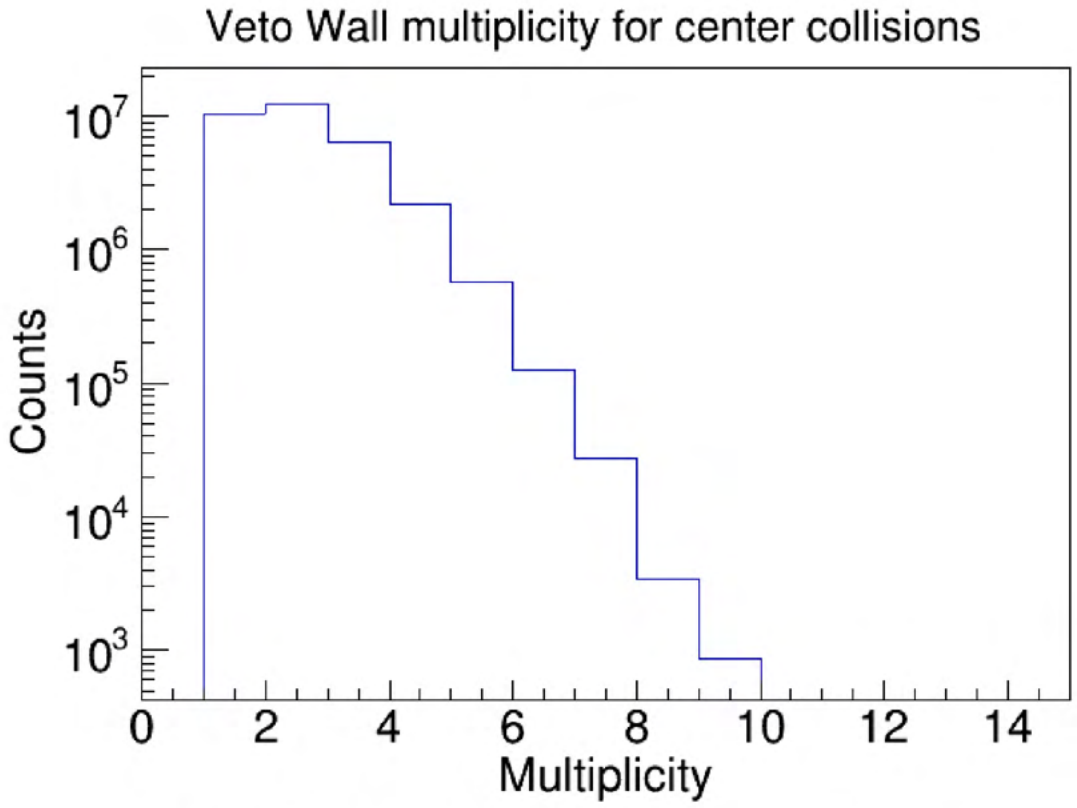

Figure 4.34: Veto Wall multiplicity for center collision events.

Chapter 5

Data Analysis

5.1 Finding the Time of Flight of Particles

Knowing the time of flight precisely is essential in determining the energy of the charged particles in the Veto Wall and neutrons in the LANA. If we know time of flight and the particle trajectory from the target we can calculate the velocity of that particle, and hence its energy. As discussed in the previous Chapter, the Forward Array detector is used to measure the start time of the reaction. A typical time of flight spectra for particles hitting one of the Veto Wall detectors is shown in Figure 5.1 (left panel). The spectra shows a spike at around 100 ns which represents prompt gammas which is followed by heavier particles. The time of flight in that figure is calculated with respect to the Forward Array time so it has an offset. As prompt gammas travel with the speed of light the start time of the reaction should be zero so we need to correct for that offset. To do it, we find the mean value of the spike and subtract it from the time of flight. Figure 5.1 (right panel) shows the corrected time of flight distribution for the Veto Wall detector 12. The start time of the Forward Array can be either the first time (FA Time Min) when one of the Forward Array scintillators gets hit first by a gamma particle or can be the average of all the times of particles hitting the Forward Array scintillators (FA Time Mean).

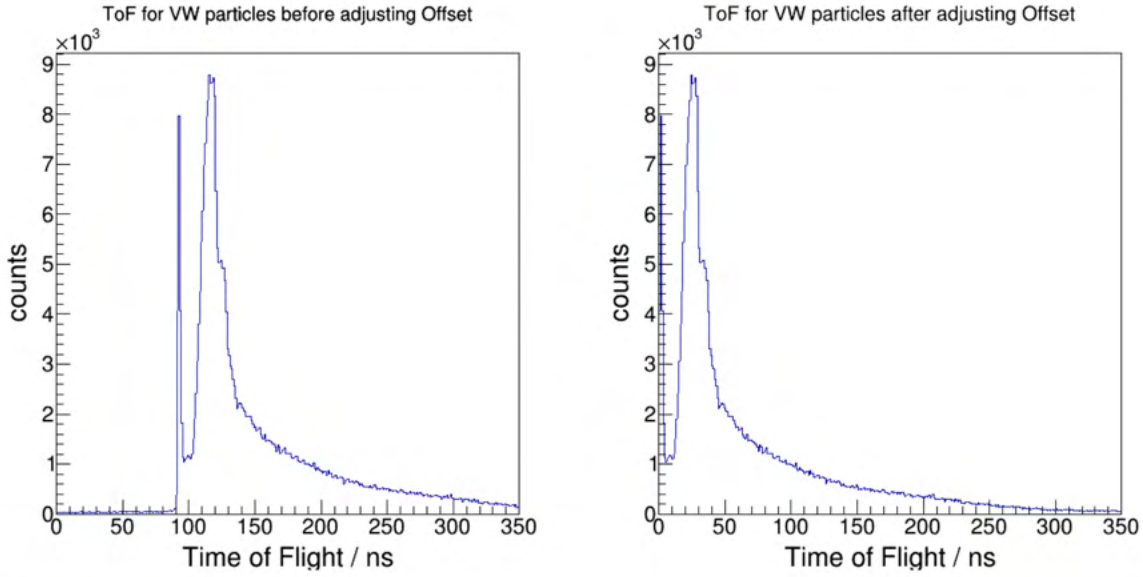

Figure 5.1: Time of flight spectra in nanosecond for the particles hitting the Veto Wall detector 12.

We find the time of a particle hitting the Veto Wall by using the average time of the signals from the top and the bottom PMTs. In order to find the best start time among FA Time Min and FA Time Mean, we used the prompt gamma spike and found its full width half maximum (FWHM). For this, we used the minimum distance from the reaction center to the Veto Wall and the distance for each hit on the Veto Wall. Each hit in the Veto Wall detectors have different distance from the target. For accurate calculation of the time of flight resolution, we normalized the time of flight using the following equation:

$$ToF_{Normalized} = \frac{ToF \cdot D_{minimum}}{D} \tag{5.1}$$

A distribution of the normalized time of flight is shown in Figure 5.2 and the gamma peak was fitted using a Gaussian function. The full width half maximum (FWHM) of the gamma peak gives the resolution of the time of flight measurements. A comparison of FWHM was made in the normalized histogram constructed using FA Time Mean and FA Time Min as shown in Figure 5.2. FWHM is minimum in the normalized time of flight histogram obtained from FA Time Min. Hence, in order to calculate the time of flight in our analysis, we use FA Time Min as our start time of the reaction.

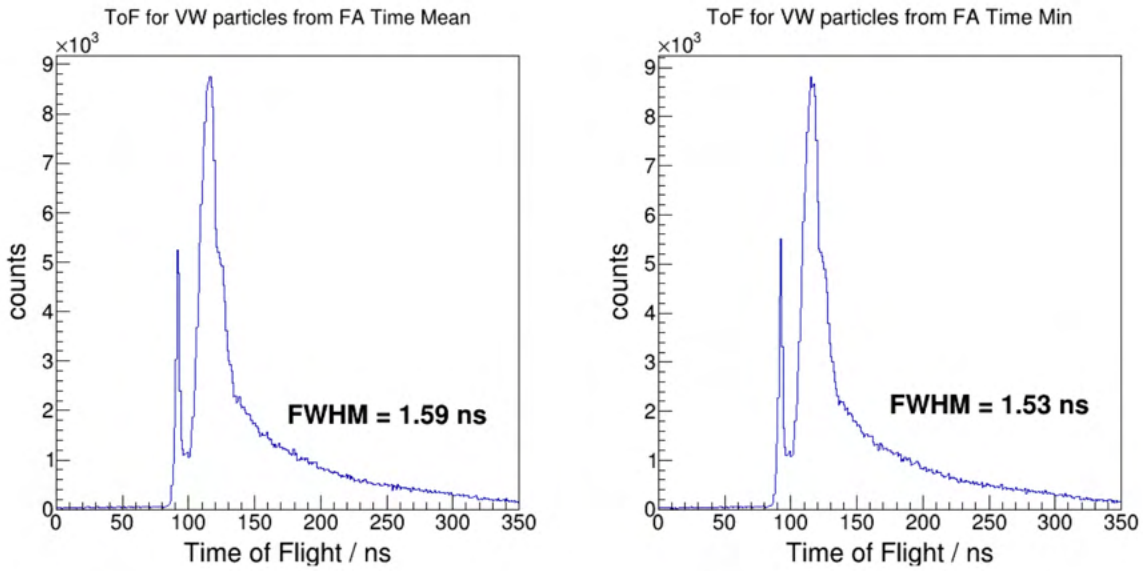

Figure 5.2: A comparison of full width half maximum of the gamma peak obtained from the normalized time of flight using FA Time Mean (left) as start time and FA Time Min (right) as start time.

5.2 Normalization of the Geometric Mean Signal

The geometric mean (in channels) of the signal in the Veto Wall detector is proportional to the energy deposited by the particle hitting it. That signal can be converted to the energy (in MeVee) as described in Section 4.3.1. The spectra of the geometric mean vs the time of flight can be used to identify charged particles like protons, deuterons and tritons. Since these charged particles have different energy loss for the same time of flight (velocity), we used the geometric mean of the energy signal versus the time of flight to identify those particles in our detector. To do that for all the Veto Wall bars, they have to be gain matched. By gain match, we understand that the PMTs used for a bar should have same or nearly same amplitudes (see Section 4.2.1). Figure 5.3 shows a comparison between unnormalized geometric mean with normalized geometric mean for the Veto Wall. X axis represents the time of flight in nanosecond (ns) while Y axis represents the geometric mean in channel (ch) units. Color scale of the Z axis represents the number of particles in each bin. The color is changing from blue to yellow, where yellow represents more counts and blue represents less counts. We can see a flash of yellow near origin

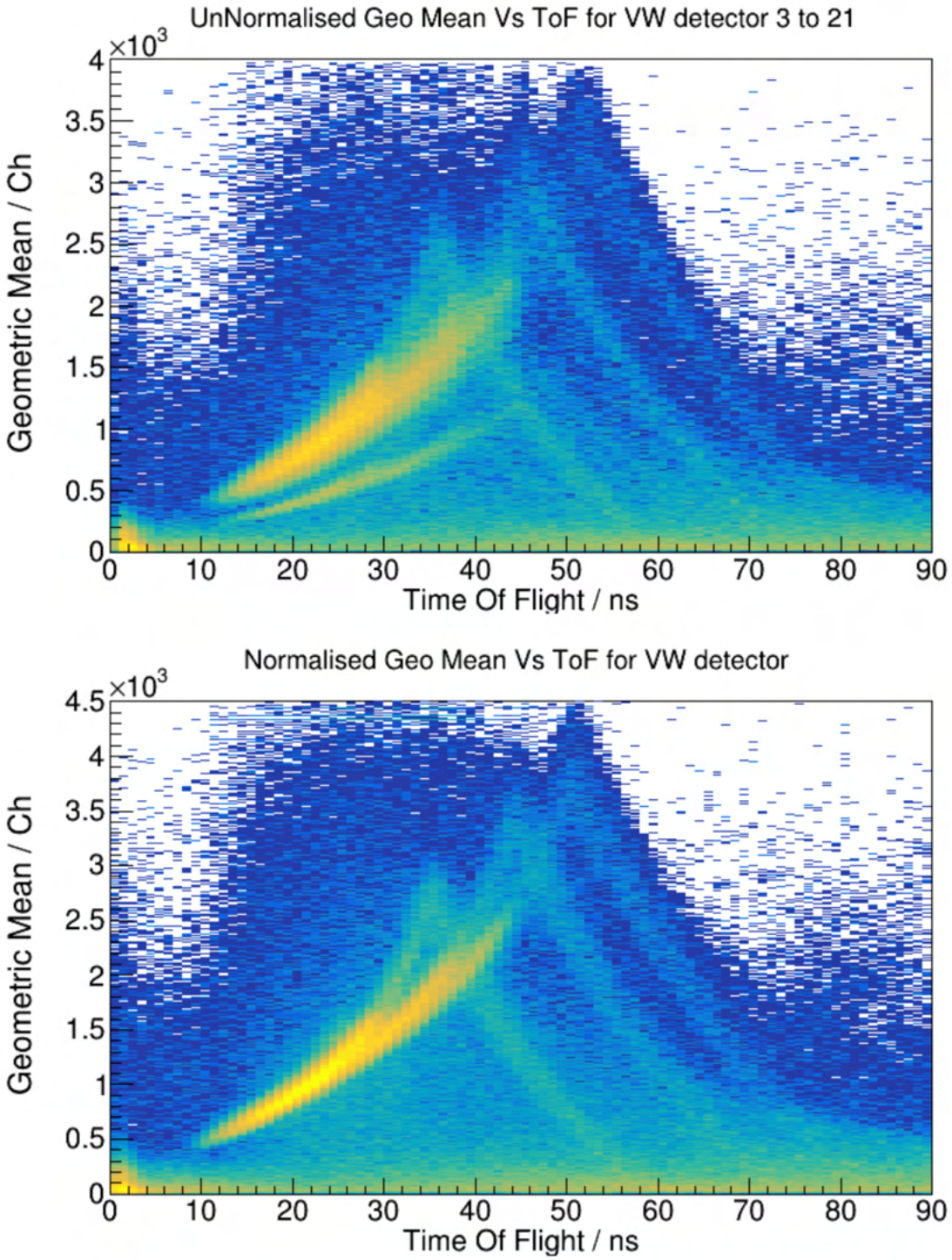

Figure 5.3: Unnormalized (top) and normalized (bottom) geometric mean vs the time of flight for the Veto Wall.

which represents prompt gammas that give the start time of our reaction. In the bottom panel of Figure 5.3 we can identify three distinctive bands coming from right, peaking at different values and then decreasing with the decrease of the time of flight. Those

bands finally merge with each other. These three bands represent protons, deuterons and tritons. The peak values of the lines represent the punch through energies of those particles. The yellow merged band represents the passing of the particles from the Veto Wall towards the LANA. The bottom panel of Figure 5.3 is the normalized geometric mean histogram with the time of flight. The normalization of the geometric mean is done using the top panel of the Figure 5.3. In that panel we can see a small yellow band below the punch through region which suggests that particles are overlapping with each other so normalization is needed to separate them. For normalizing the geometric mean, we found the punch through values for protons, deuterons and tritons for all the Veto Wall detectors. Taking the punch through values of detector 12 as reference, we scaled the punch through values of all other detectors with our reference.

5.3 Energy Loss in Different Materials

The fragments produced after the collision can travel through different materials before hitting the Veto Wall detector. Those fragments will then lose energy by passing through the vacuum chamber. The vacuum chamber is made up of stainless steel that is 3 mm in thickness. Additionally, there is a rim around the vacuum chamber which is 6 mm. This rim is to make the chamber rigid. Since the surface area of the rim throughout the chamber is small, only a small percentage of particles pass through it. Once particles get out of the chamber, they travel in air for some distance before hitting the shadow bar stand, that has two frames (front and back) with a gap of 19 cm in between. Each frame is 3 mm thick and is made of stainless steel with aluminum legs at the bottom. The legs of these two frames do not overlap with respect to reaction center and very few particles pass through them before hitting the Veto Wall and the LANA detectors. The particles emerging from the vacuum chamber lose some of their energy in the air, the shadow bar stand and then they travel few meters in air before hitting the Veto Wall.

Energy loss of the particles in different materials is calculated using LISE ++. LISE

is a DOS-based program that uses Fast Fourier Transform (FFT) algorithms for its operations. This software is used to calculate the transmission and yields of fragments produced at various stages of the beam development and reaction. LISE ++ is useful to select radioactive nuclei, produce radioactive beams, identify different nuclei and their charges. In present days, physicists use LISE ++ to calculate the reaction mechanism and cross sections [98], beam optics, acceptance and transmission calculations [99], energy loss and ranges in different materials [100, 101]. More information about LISE ++ can be found here [102, 103].

Charged particles can travel along different paths before hitting the Veto Wall detector which affect their total energy loss. For each of those cases of the energy loss calculations, a plot is made with the percentage of a loss in the energy versus the initial energy. The initial energy is the total energy at the reaction center. The values of the initial energies taken here vary from punch through energy to 500 MeV. The Figures 5.4, 5.5, 5.6 show such plots for protons, deuterons and tritons, respectively.

As shown in Figures 5.4, 5.5, 5.6, the higher the energy of charged particles the smaller the percentage loss in the energy is in different materials. Less energetic charged particles can be stopped before reaching the Veto Wall. Even if they make it to the Veto Wall, they can be stopped in that detector if their energy is less than the punch through energy (minimum energy to escape the detector).

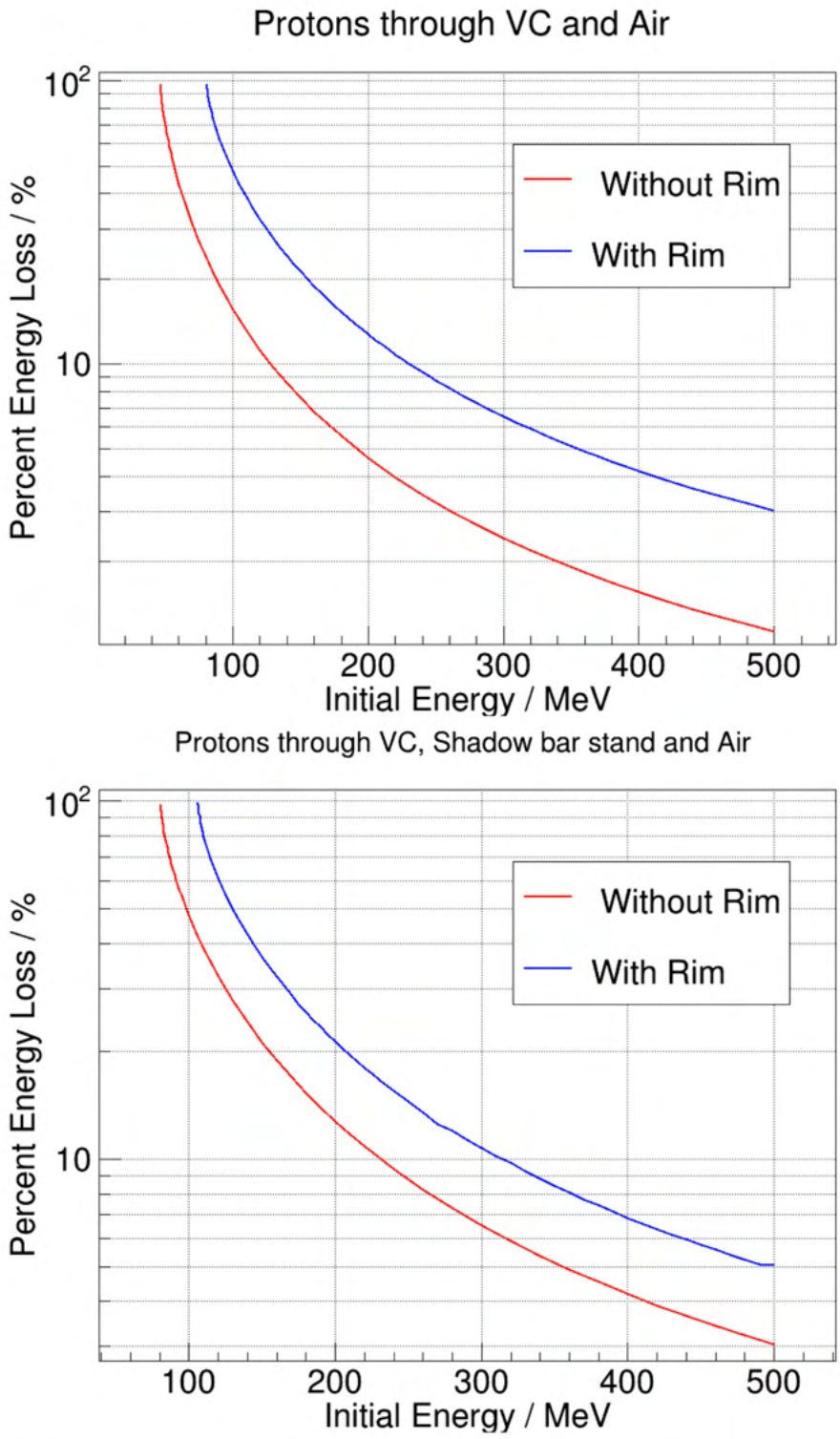

Figure 5.4: The percentage of energy loss in materials in all possible routes for protons. Top figure shows comparison of percentage of energy loss while hitting the Veto Wall when protons travel via vacuum chamber and air with vacuum chamber, rim and air. Bottom figure shows comparison of percentage of energy loss while hitting the Veto Wall when protons travel via vacuum chamber, shadow bar stand and air with vacuum chamber, rim, shadow bar stand and air.

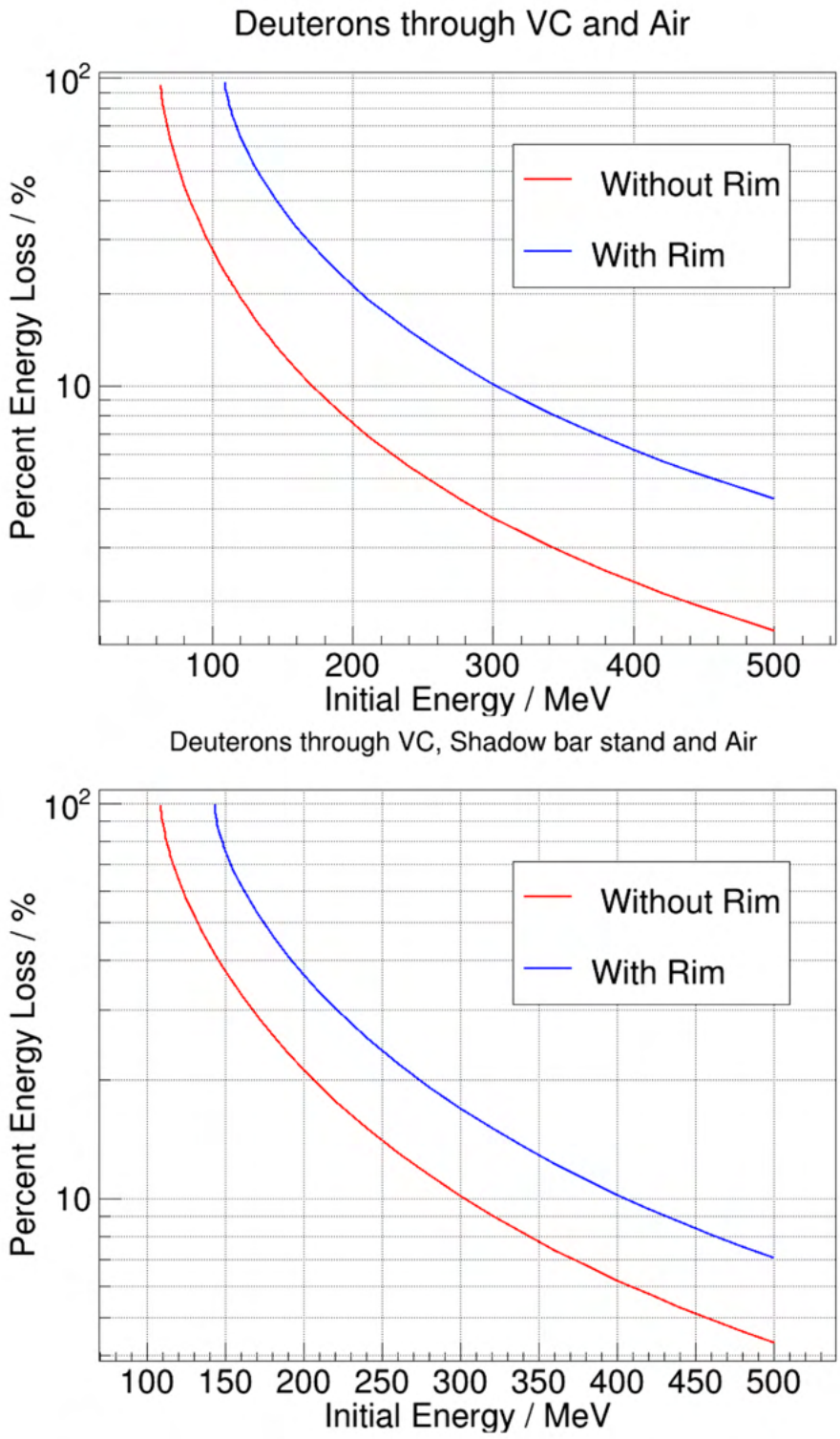

Figure 5.5: The percentage of energy loss in materials in all possible routes for deuterons. Top figure shows comparison of percentage of energy loss while hitting the Veto Wall when deuterons travel via vacuum chamber and air with vacuum chamber, rim and air. Bottom figure shows comparison of percentage of energy loss while hitting the Veto Wall when deuterons travel via vacuum chamber, shadow bar stand and air with vacuum chamber, rim, shadow bar stand and air.

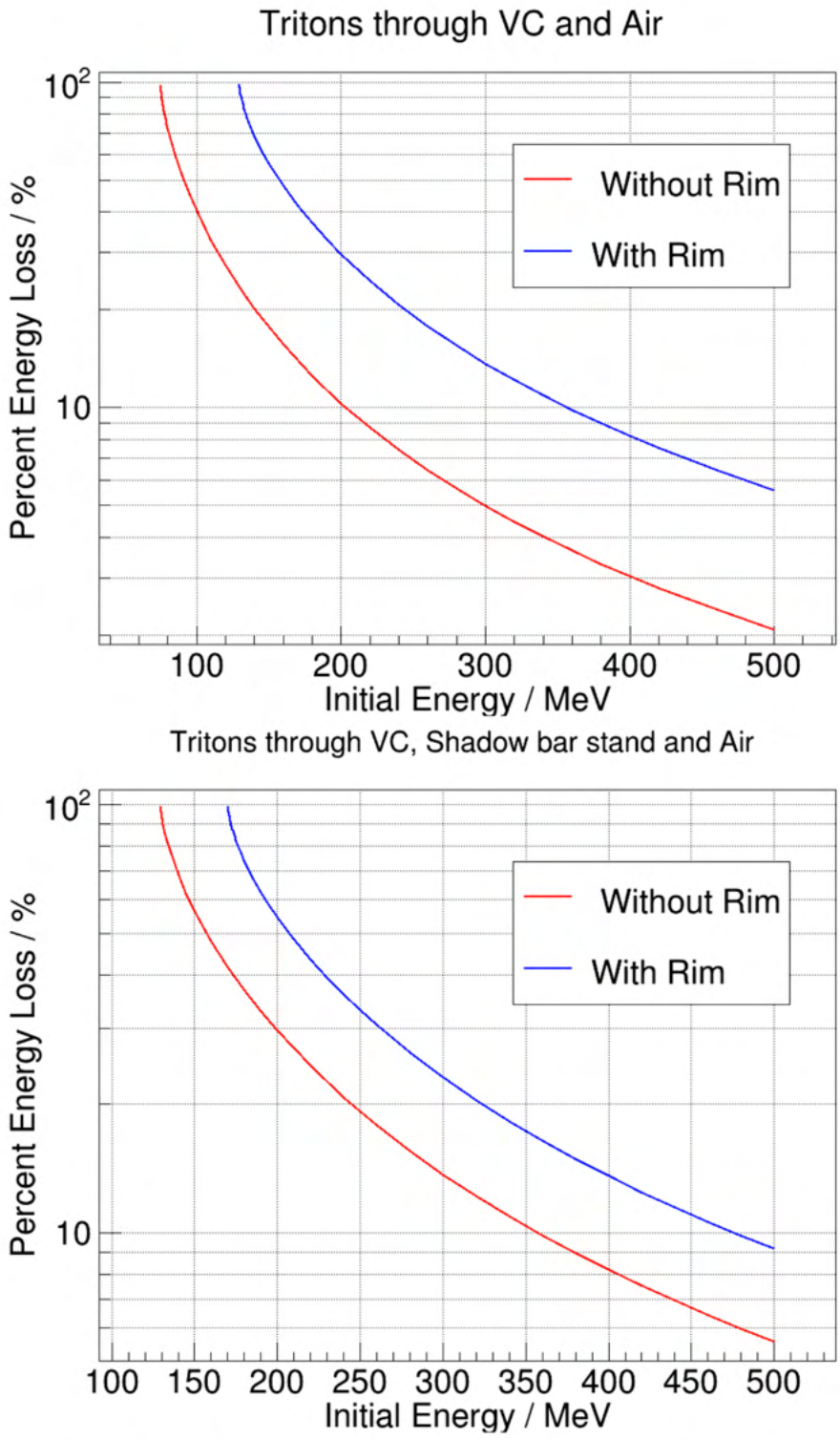

Figure 5.6: The percentage of energy loss in materials in all possible routes for tritons. Top figure shows comparison of percentage of energy loss while hitting the Veto Wall when tritons travel via vacuum chamber and air with vacuum chamber, rim and air. Bottom figure shows comparison of percentage of energy loss while hitting the Veto Wall when tritons travel via vacuum chamber, shadow bar stand and air with vacuum chamber, rim, shadow bar stand and air.

Punch through energy is the energy required to punch through the material. LISE ++ is also used to calculate the punch through energy of charged particles in different materials provided that the thickness of materials is known. The Table 5.1 illustrates the punch through energy of different charged particles in MeV for BC plastics of 10 mm thick (Veto Wall).

Table 5.1: The punch through energy along with energy loss for different charged particles.

Particles	Total KE (MeV)	Vacuum Chamber (3cm)	Air (63.8cmm)	SB stand (3mm)	Air (19cm)	SB stand (3mm)	Air (2.46m)	Vetowall (10mm)
${}^{1}_{1}H$	89.44	13.99	0.19	16.3	0.22	20.92	5.05	32.77
${}^{2}_{1}H$	120.91	18.72	0.26	21.85	0.3	28.07	6.85	44.86
${}^{3}_{1}H$	144.35	22.23	0.31	25.96	0.35	33.4	8.20	53.90
${}^{3}_{2}He$	315.89	49.67	0.67	57.79	0.77	74.13	17.81	115.05
${}^{4}_{2}He$	356.94	55.84	0.76	65.04	0.87	83.53	20.18	130.72
${}^{6}_{2}He$	426.16	66.24	0.91	77.31	1.05	99.27	24.12	157.26
${}^{8}_{2}He$	483.42	74.84	1.04	87.39	1.19	112.27	27.36	179.33

Table 5.2: The punch through energy along with energy loss for different charged particles when shadow bar frame is excluded and particles are supposed to travel through air once they emerged out of vacuum chamber.

Particles	Total KE (MeV)	Vacuum Chamber (3mm)	Air (3.3m)	VetoWall (10mm)
${}^{1}_{1}H$	59.22	20.74	5.69	32.77
${}^{2}_{1}H$	80.40	27.83	7.71	44.86
${}^{3}_{1}H$	96.24	33.10	9.23	53.90
${}^{3}_{2}He$	208.60	73.49	20.05	115.05
${}^{4}_{2}He$	236.26	82.81	22.71	130.72
${}^{6}_{2}He$	282.83	98.41	27.15	157.26
${}^{8}_{2}He$	321.45	111.29	30.81	179.33

The Table 5.1 shows the minimum energy loss (in MeV) for various charged particles in order to punch through those materials. For example 89.46 MeV proton loses 13.99 MeV energy while punching through the stainless steel (Vacuum Chamber) of 3 mm, 0.19 MeV while traveling through the 63.8 cm air before hitting the shadow bar stand. The shadow bar stand is 3 mm thick and is made of stainless steel and protons lose 16.3

MeV energy in the first frame, 0.22 MeV in the air in between two frames of the stand and finally 20.92 MeV in the second frame. Then protons lose 5.05 MeV during their propagation in air before reaching the Veto Wall. When striking the Veto Wall, protons will have about 32.77 MeV energy which is just sufficient to punch through the Veto Wall. The minimum energy at the reaction center for protons to punch through the Veto Wall is 89.46 MeV. Similarly, we can find energy loss and punch through energy for different charged particles from Table 5.2. It shows the punch through energy for different charged particles when there is no shadow bar stand, that is when these particles pass through the openings of the frame meant for shadow bars placement (see Figure 3.19). Using the

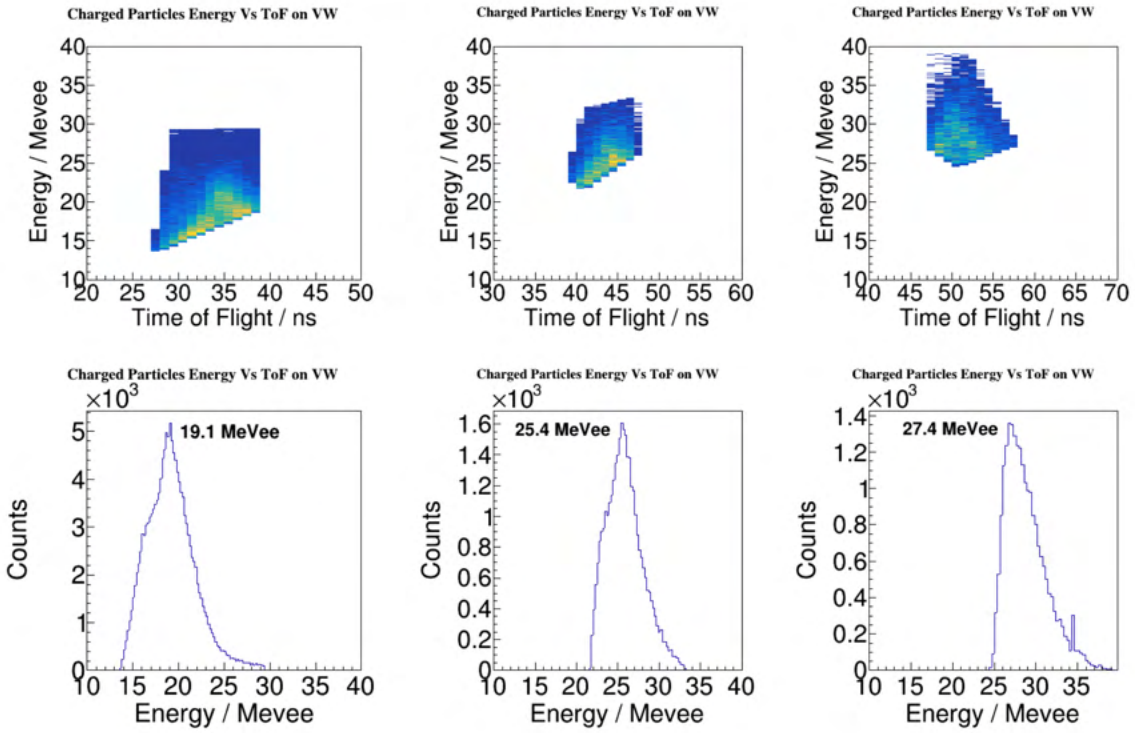

Figure 5.7: One dimensional and two dimensional histogram showing energy in MeVee unit at punch through region.

geometric mean of the light outputs we calculate the energy in electron equivalent unit MeVee as discussed in Section 4.3.1. In order to use the energy of MeVee unit from two PMTs for further analysis, we need to convert it to MeV. Energy in MeV depends linearly

on energy in MeVee as shown in following equation:

$$E = a \cdot E_{ee}, \tag{5.2}$$

where E is the energy in MeV, E_{ee} is the energy in MeVee and a is the proportionality parameter. The parameter a can be different for different particles such as protons, deuterons and tritons. We find the value of that parameter by using the punch through energy in MeV and in MeVee units. LISE++ gives us the punch through energy in MeV unit. Plotting a histogram of energy obtained from the light output versus the time of flight, gating on the punch through regions of different particles (protons, deuterons and tritons) gives us the top three panels of Figure 5.7. When we project those distributions onto the energy axis (here is y axis), we obtained one dimensional punch through energy histogram in MeVee units. Bottom three panels of Figure 5.7 show such histograms for protons, deuterons and tritons, respectively. The means of these histograms for respective particles are obtained which is shown in the label of the Figure 5.7.

This Figure 5.7 suggests that punch through energy of protons is about 19.1 MeVee and Table 5.1 from LISE++ calculations shows that punch through value of protons is about 32.77 MeV. Using these two values, the proportionality parameter for protons is 1.715 MeV/MeVee. Similarly for deuterons the value of that parameter is 1.766MeV/MeVee and for tritons it is 1.967 MeV/MeVee. These values clearly illustrate that "a" from Equation 5.2 is different for different charged particles.

5.3.1 Kinematics Calculations of the Time of Flight

The punch through time, the time of flight of a particle with minimum energy to punch through the detector, for protons, deuterons and tritons can be obtained from the histogram of energy deposited in the Veto Wall versus the time of flight. Those times are about 35 ns, 45 ns and 51 ns respectively and they correspond to energies of 19.1 MeVee, 25.4 MeVee and 27.4 MeVee for protons, deuterons and tritons, respectively. Calculations

of the time of flight is done to look for any discrepancies in the time of flight and the energy loss using LISE++. The results for different charged particles punching through various materials are shown in the Table 5.3.

Table 5.3: The time of flight for different charged particles as they punch through various materials including the shadow bar stand on their way.

${}^{1}_{1}H$	Vacuum Chamber (3mm)	Air (63.8cm)	SB stand (3mm)	Air (19cm)	SB stand (3mm)	Air (2.46m)	Veto Wall (10mm)	Total
Energy at (MeV)	89.44	75.45	74.84	58.46	58.23	37.10	32.77	
Time of Flight at (ns)	0.0229	5.3078	0.0250	1.7958	0.0284	29.1870	0.1262	36.49
${}^{2}_{1}H$	Vacuum Chamber (3mm)	Air (63.8cm)	SB stand (3mm)	Air (19cm)	SB stand (3mm)	Air (2.46m)	Veto Wall (10mm)	Total
Energy at (MeV)	120.91	102.19	101.36	79.38	79.08	50.72	44.86	
Time of Flight at (ns)	0.0708	6.4476	0.0304	2.1785	0.0281	35.2875	0.1525	44.19
${}^{3}_{1}H$	Vacuum Chamber (3mm)	Air (63.8cm)	SB stand (3mm)	Air (19cm)	SB stand (3mm)	Air (2.46m)	Veto Wall (10mm)	Total
Energy at (MeV)	144.35	122.11	121.12	95.02	94.66	60.92	53.90	
Time of Flight at (ns)	0.0312	7.2177	0.0340	2.4367	0.0385	39.4019	0.1702	49.33

Table 5.4: The time of flight for different charged particles as they punch through various materials excluding the shadow bar stand on their way.

${}^{1}_{1}H$	Vacuum Chamber (3mm)	Air (3.3mm)	Veto Wall (10mm)	Total
Energy at (MeV)	59.22	38.46	32.77	
Time of Flight at (ns)	0.0475	38.2122	0.1262	38.38
${}^{2}_{1}H$	Vacuum Chamber (3mm)	Air (3.3m)	Veto Wall (10mm)	Total
Energy at (MeV)	80.40	52.57	44.86	
Time of Flight at (ns)	0.0580	46.3258	0.1525	46.53
${}^{3}_{1}H$	Vacuum Chamber (3mm)	Air (3.3m)	Veto Wall (10mm)	Total
Energy at (MeV)	96.24	63.12	53.90	
Time of Flight at (ns)	0.0651	51.7318	0.1702	51.96

In the Table 5.3, we have listed the time of flight for charged particles as they punch through different materials. For protons, minimum energy of 89.44 MeV is required to punch through the Veto Wall detectors. 89.44 MeV protons take about 0.0229 ns to punch through 3 mm thick vacuum chamber. After losing some energy in vacuum

chamber, those protons take 5.3078 ns to travel through 63.8 cm air. After traveling that distance protons hit the first frame of the shadow bar stand which is 3 mm thick. They take 0.0250 ns to punch through that frame and take 1.7958 ns to reach the second frame of the stand. It takes 0.0284 ns time to punch through it. After escaping the shadow bar stand, protons take 29.187 ns to travel the distance of 2.46 m in air and hit the Veto Wall. They take 0.1262 ns to punch through 10 mm thick Veto Wall detector. The total time to punch through the Veto Wall starting from vacuum chamber is 36.49 ns. Similarly, the punch through times were found for deuterons and tritons. Results are shown in the Table 5.3. Tables 5.3 and 5.4 show the punch through times of the charged particles following different paths to the Veto Wall (different energy loss). The difference is that the first table includes the shadow bar stand while the second table doesn't. The reason for the calculations in the second table is that there are five holes in the stand where shadow bars are placed. The time of flight of protons from the Table 5.3 is pretty close to the time of flight obtained from the data that is about 35 ns while the time of flight from the Table 5.4 is larger by about 3 ns. The weighted average time of flight obtained from both calculations is $\approx$ 37.13 ns for protons, $\approx$ 44.98 ns for deuterons and $\approx$ 50.22 ns for tritons. The average time of flight for protons is larger by 2 ns while for deuterons and tritons the average time of flight agree with the time of flight from experiment. So, we studied the effect of 1 ns shift of the time of flight in the energy.

5.4 Effect of the Position Resolution on the Energy

The Veto Wall has a time resolution of 1 ns that is equivalent to a position resolution of 7 cm. We calculated the kinetic energy of the charged particles hitting the Veto Wall using the time of flight technique. The distance that a particle travels from the reaction center to the spot on the Veto Wall can be calculated using the information about the distance of the Veto Wall from the reaction center, the width of the Veto Wall bar and the height of the Neutron Wall bar. The overlapping of the Veto Wall bars

and the gap between the Neutron Wall bars were included in the calculations. Using that information we calculated the distance of travel for different spots on the Veto Wall which are the intersections of the Veto Wall bars and the Neutron Wall bars as (3,3),(3,12),(3,18),(12,3),(12,12),(12,18),(22,3),(22,12),(22,18). The first number in those pairs represents the Veto Wall bar and the second number represents the Neutron Wall bar. Those pairs were chosen so that we can evaluate the effect of the position resolution at every corner and in the center of the Veto Wall. The time of flight of the charged particles from the reaction center to these spots was calculated using the following formula:

$$t = \frac{d}{v} = \sqrt{\frac{m \cdot d^2}{2 \cdot E}}, \tag{5.3}$$

where t is the time of flight, m is the mass of the charged particles and E = $\frac{mv^2}{2}$ is the kinetic energy of the charged particles. If we assume the 7 cm position resolution in the

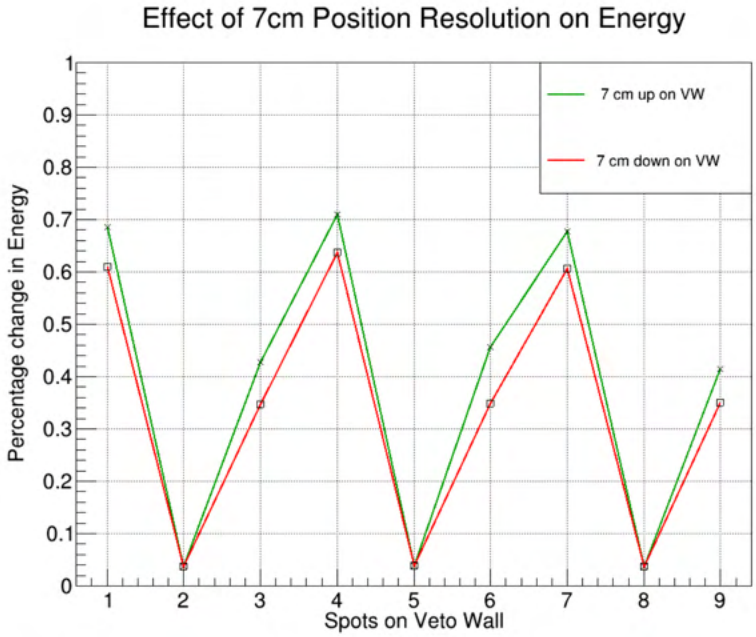

Figure 5.8: Effect of the Veto Wall resolution on energy calculated from the time of flight technique. Red line represents percentage change in the energy in moving 7 cm up from the hit position and blue line represents percent change in the energy when moving 7 cm down. This plot is done for protons. Deuterons and tritons give similar change in the energy. From this plot we can see the energy change is about 0.7 % atmost due to the position resolution effect on the distance of travel. This effect does not concern most in the energy calculation for the charged particles.

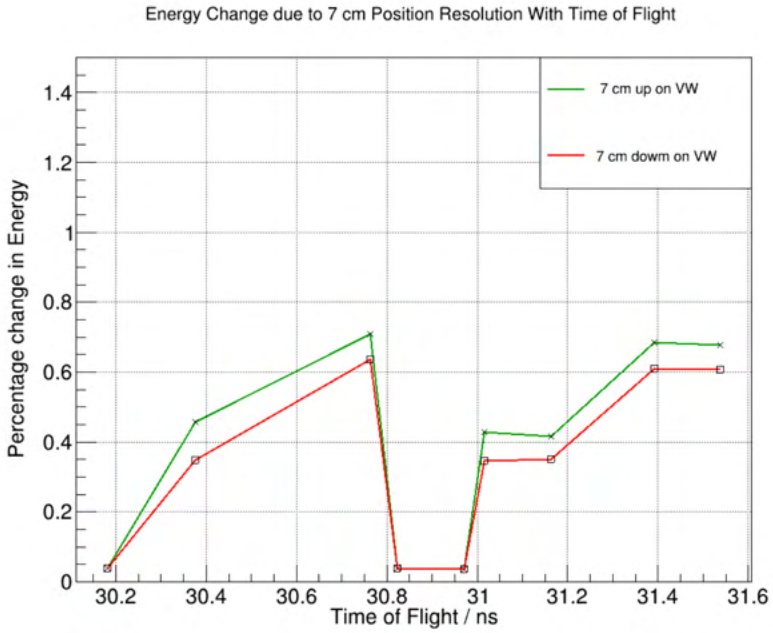

Figure 5.9: Energy change due to 7 cm position resolution versus the time of flight. Time of flight of 30.9 ns was used as reference.

Veto Wall then we can calculate the distance of travel for the spot that is 7 cm up or down from the original position. Using the time of flight and the newly calculated distance we calculate the energy of the particle and percentage change in the energy caused by the 7 cm position resolution. The time of flight is calculated using the punch through energy.

The red line in Figure 5.9 represents the effect of 7 cm position resolution down from the hit position along the Veto Wall while the green line is for the hit being 7 cm up from original position. Figure 5.9 shows that 7cm change in distance of travel of a particle has minimum effect in the time of flight which in-turn has low impact on the energy. We do not have to take into account such effect while calculating energy as it is very small.

5.5 Effect of 1 ns Change in the Time of Flight on the Energy

Since the energy of a particle is calculated using the time of flight measurements, we would like to estimate the effect of changing the time of flight by 1 ns on the energy

of a particle. To study such an impact we chose the same nine spots on the Veto Wall as in studies presented in the previous section. Then, we modified the time of flight by increasing and decreasing it by 1 ns. That allowed us to calculate the energy using the new time of flight and estimate the percentage change in the energy due to that change.

Figures 5.10, 5.11, 5.12 show percentage change in energy when the time of flight

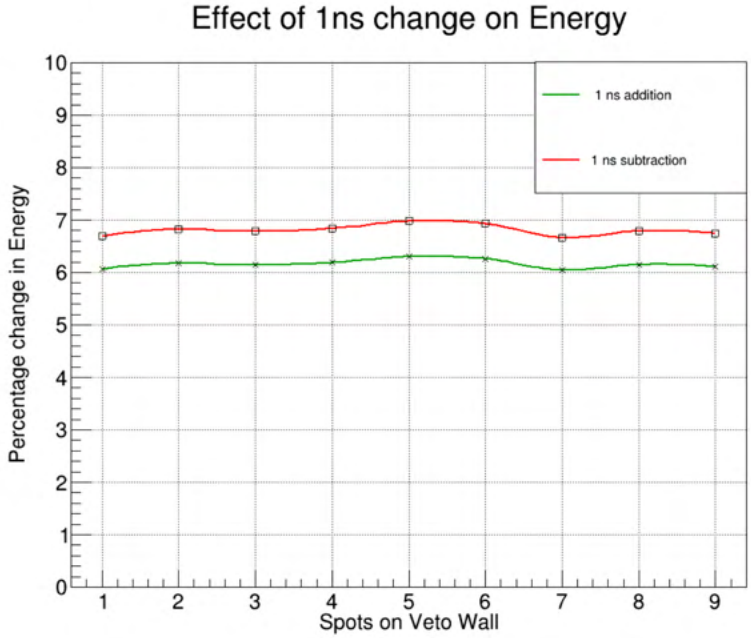

Figure 5.10: Effect of 1 ns shift on the energy for protons.

is either increased or decreased by 1 ns for protons, deuterons and tritons respectively. Green lines in those figures show the effect on energy from 1 ns addition on the time of flight while red lines show such effect from 1 ns subtraction on the time of flight. When the time of flight is more, the energy of the particle is less when they punch through that material. This result is supported by the relation between the energy and the time in equation 5.2. Figures 5.10, 5.11 and 5.12, show that protons are more affected by the energy resolution than deuterons and tritons due to the 1 ns shift in the time of flight. This is because protons are lighter and have higher velocities for the same time of flight.

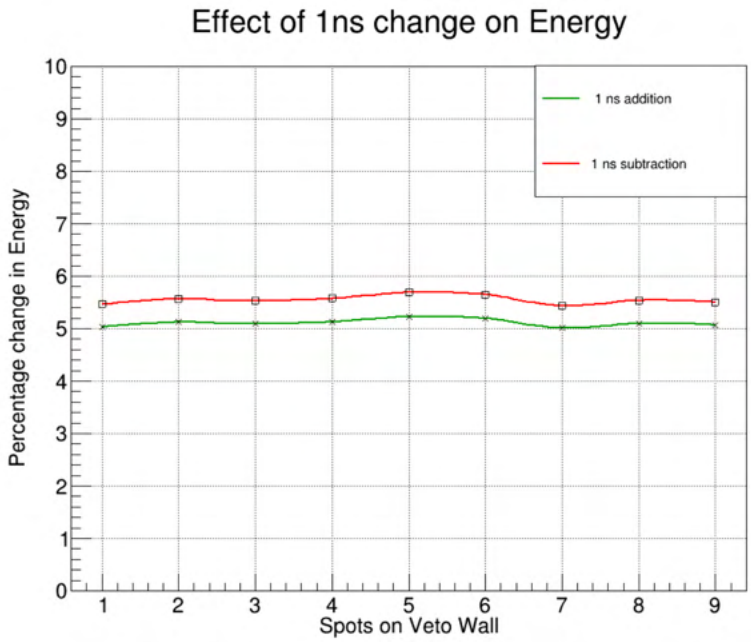

Figure 5.11: Effect of 1 ns shift on the energy for deuterons.

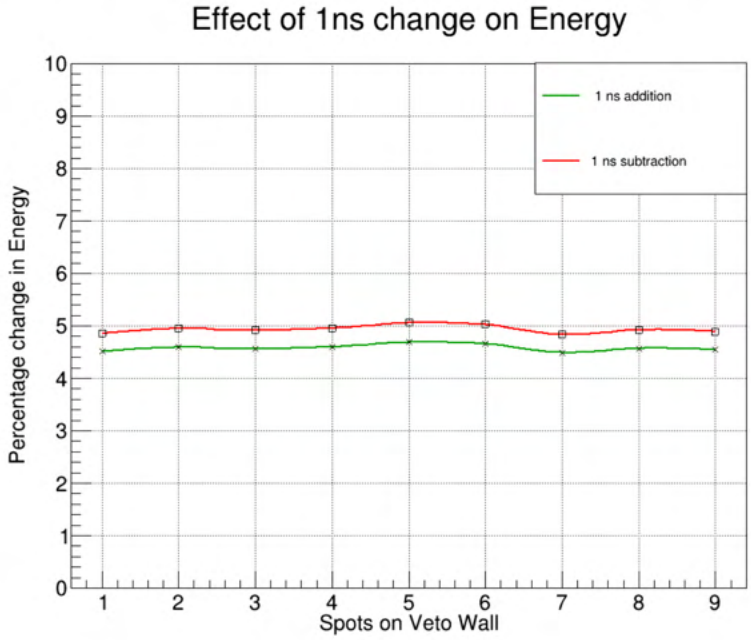

Figure 5.12: Effect of 1 ns shift on the energy for tritons.

5.6 Identification of Charged Particles in the Veto Wall

Charged particles deposit energy in the Veto Wall. Depending on their energy they can either punch through or stop in the scintillator. Those charged particles can be

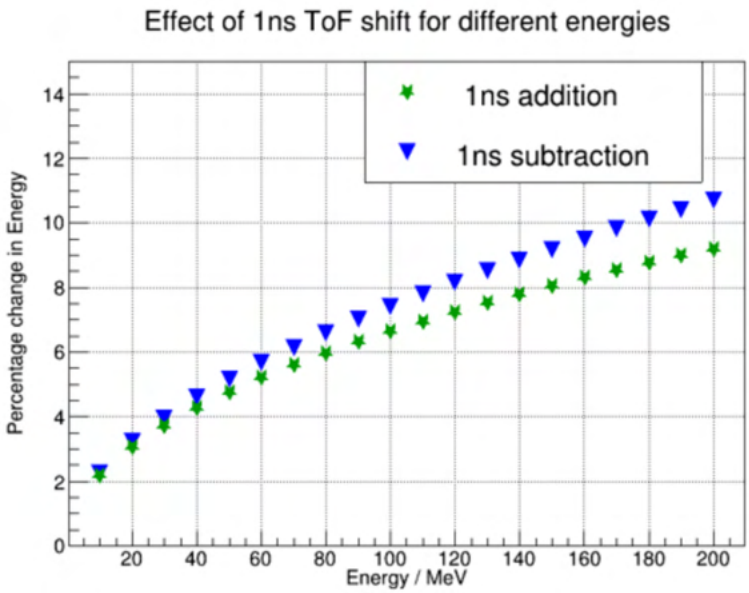

Figure 5.13: Effect of 1 ns shift on different energies for protons

identified based on the time of flight vs energy loss measurement technique, as shown in Figure 5.14. Three PID lines represent protons (P), deuterons (D) and tritons (T). Low

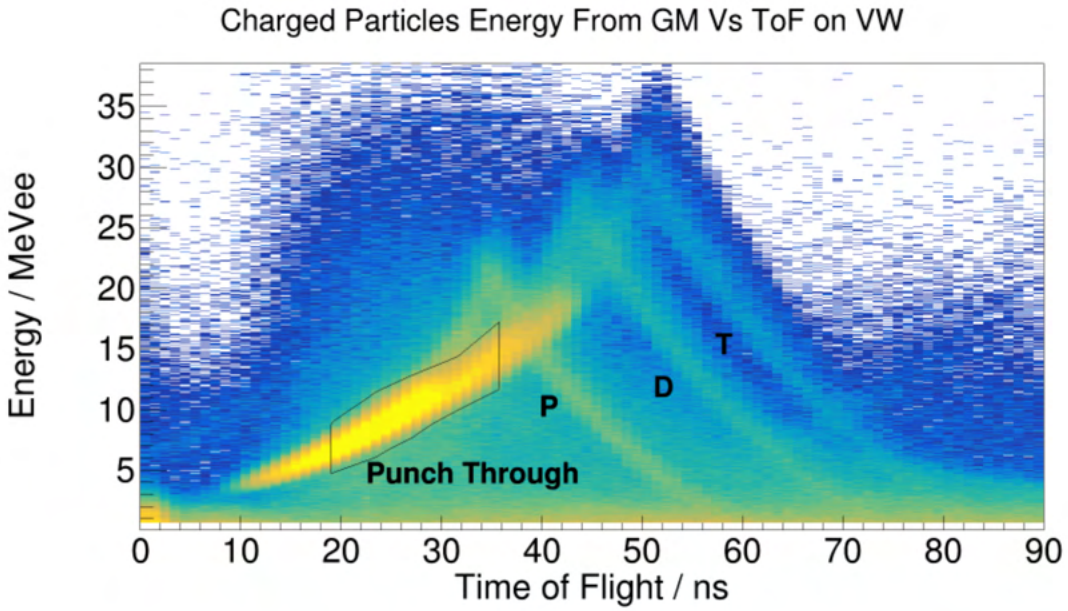

Figure 5.14: PIDs of different charged particles on the Veto Wall.

energetic particles are stopped at the Veto Wall losing all of their energies (longer time of flight) while high energetic charged particles only deposit some of their energies and pass through the detector (shorter time of flight). The yellow band in Figure 5.14, labeled as

"Punch Through", represents the charged particles punching through the detector. These particles hit the LANA where they can get further separated from each other as shown in Figure 5.15. Figure 5.14 was used to select the punch through area so we could

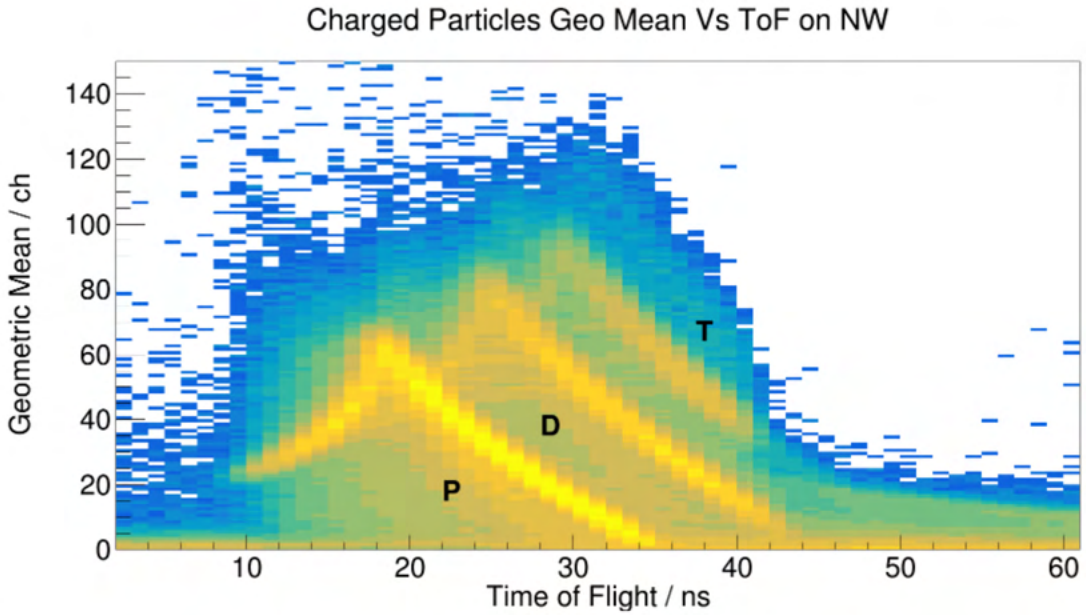

Figure 5.15: Particles seen in the LANA after passing through the punch through area in the Veto Wall.

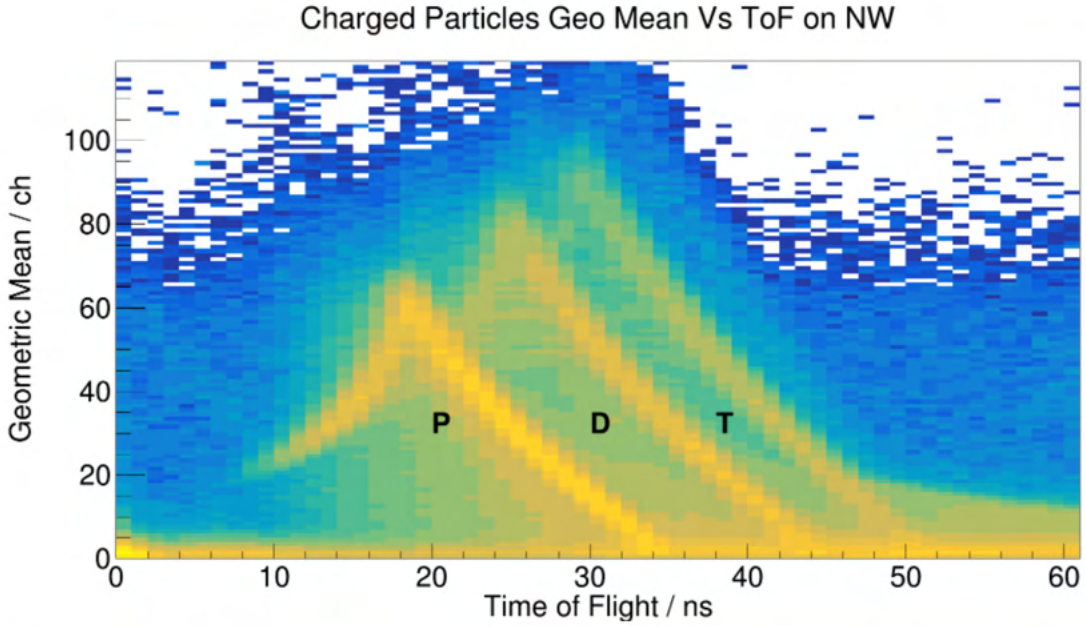

Figure 5.16: PIDs in the LANA obtained from the geometric mean and the time of flight.

obtained the spectra in the LANA only for those particles as shown in Figure 5.15. For

tritons, we can see a cut off near the tail area. This cut off is due to the punch through gate chosen in Figure 5.14. We can get punch through protons, deuterons and tritons in the Veto Wall. Figure 5.17 shows the separations of the punch through particles spectra

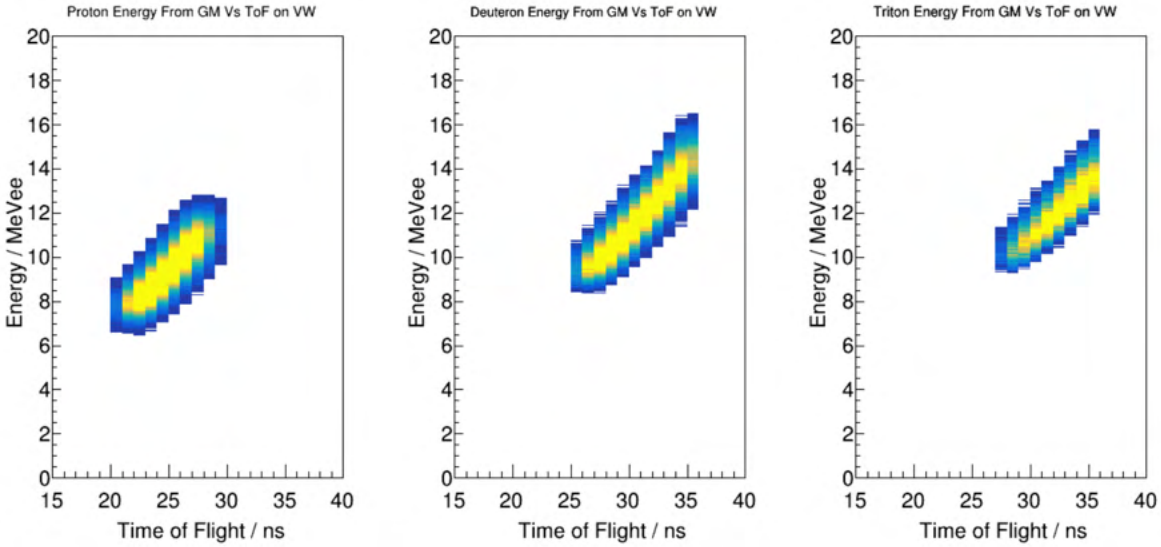

Figure 5.17: Punch through protons, deuterons and tritons as seen in the Veto Wall that are stopped in the Neutron Wall.

using gates on punch through area of Figure 5.14 and gated on stopped particles in the Neutron Wall B (Figure 5.16). Figure 5.17 shows the Veto Wall punch through protons (top panel), deuterons (middle panel) and tritons (bottom panel), that stopped in the Neutron Wall B.

5.7 Charged Particles Spectra and Their Ratios

The spectra of the charged particles deposited in the Veto Wall can be obtained from "P", "D" and "T" bands shown in Figure 5.14. Those charged particles are separated by making a gate around those bands. Energies of those particles are calculated by using the ToF measurement technique. The proton energies versus azimuthal angle (ϕ) and polar angle θ in the lab frame is plotted in Figure 5.19. Azimuthal angle is selected by making an appropriate cut in order to include the maximum acceptance of the particles in the Veto Wall. This selection is made using the Figure 5.18 which shows a plot of

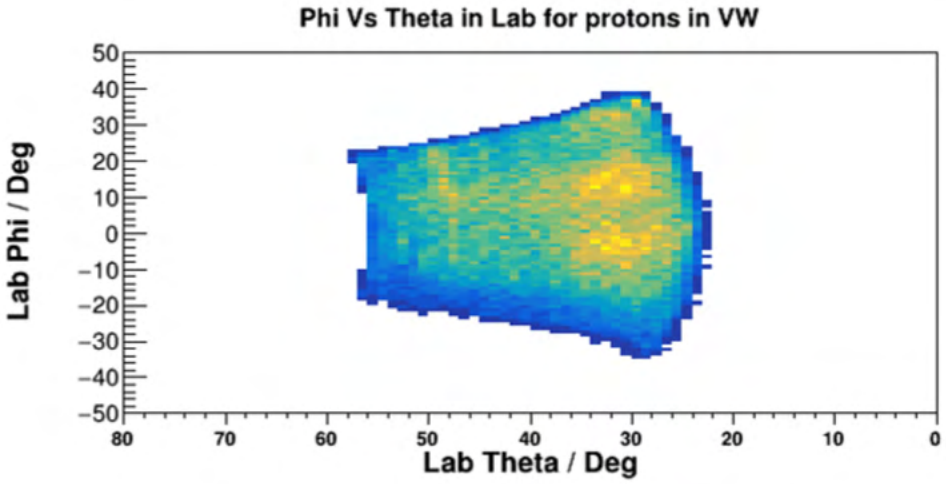

Figure 5.18: Polar angle θ vs azimutha angle ϕ in lab frame for the Veto Wall

polar angle (x-axis) vs azimuthal angle (y-axis) in lab frame. Our collisions happen in the lab frame and we have the limited acceptance in θ, ϕ and the energy due the small solid angle (0.37 sr) subtended by the Veto Wall at the collision center. The final spectra includes corrections on ϕ and θ that are not measured. θ is the angle with respect to the beam direction (Z- axis). Each particle is boosted from the lab frame to the center of mass frame. In the center of mass frame, the total momentum is zero. Typically the center of mass frame is used to compare the results from different experiments.

Figure 5.19 shows energy-theta histograms in the lab frame (top panel) and the center of mass frame (bottom panel). These plots were obtained after making a cut of 30^0 in the azimuthal angle (ϕ). Corners of the Veto Wall have smaller acceptance than its center. The cut in ϕ is made to select the region of maximum acceptance in Veto Wall. Using that cut, the acceptance for the full range in azimuthal angle for the Veto Wall can be calculated. Apart from the azimuthal angle cut, a gate on the energy-theta in lab was made to filter out the low counts due to inefficiencies on the edges of those distributions. The proton spectra can be constructed using the following equation:

$$\frac{dM}{dE \cdot d\Omega} = \frac{N(C)}{\Delta E \cdot 2\pi \int_{\theta_1}^{\theta_2} \sin\theta \; d\theta}, \tag{5.4}$$

In this differential multiplicity relation, N(C) is the number of particles normalized by the

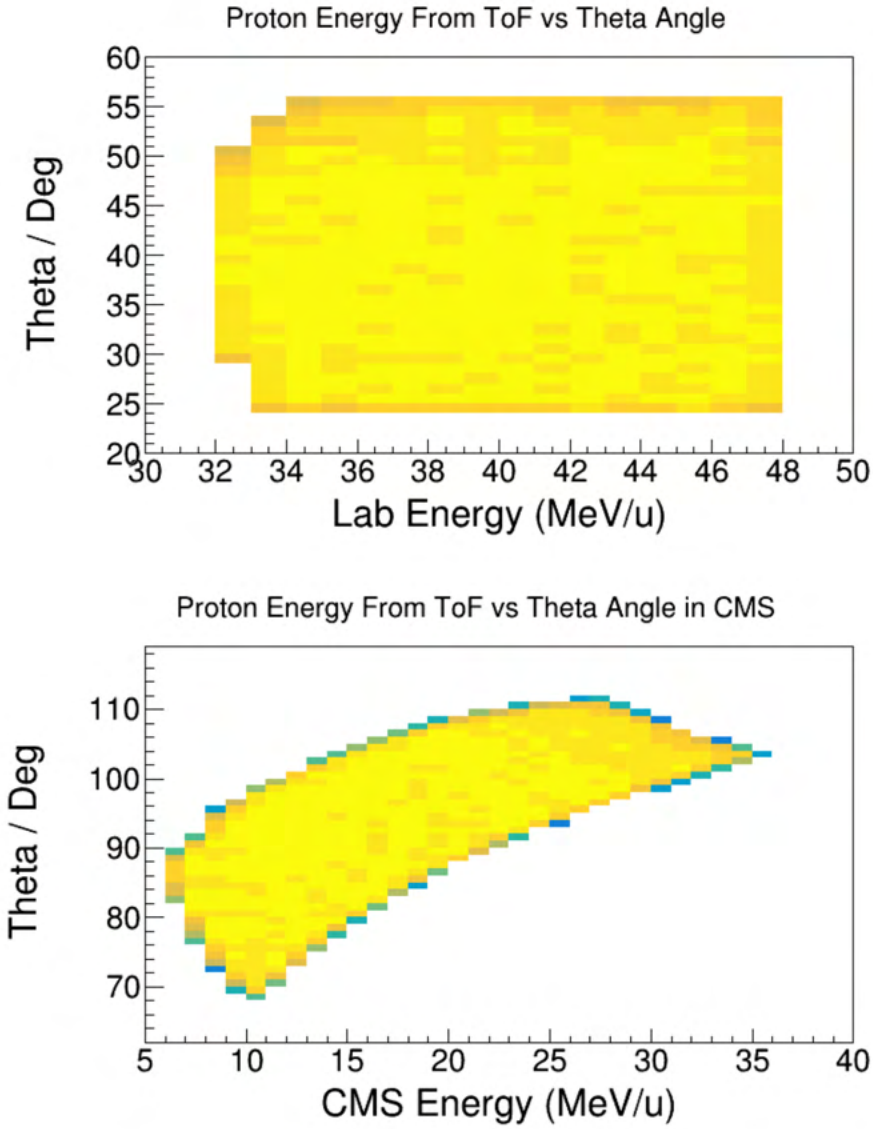

Figure 5.19: Energy vs theta angle in the lab frame (top panel) and in the center of mass frame(bottom panel for protons for the system ^{48}Ca on ^{64}Ni at 140 MeV/A.

total number of events after correcting for full coverage using the ϕ cut discussed earlier (2π factor), ΔE is the width of energy bin which is 1 MeV in our calculations, θ_1 and θ_2 are the lower and upper limits of theta coverage in each energy bin. The integration part of the Equation 5.4 accounts for the theta acceptance in the center of mass frame. Figure 5.20 shows proton spectra constructed in the lab and the center of mass frame for proton-rich (^{40}Ca on ^{58}Ni) and neutron-rich (^{48}Ca on ^{64}Ni) systems at energy 140 MeV/u. Using the same procedure, we constructed the deuteron spectra in the lab and

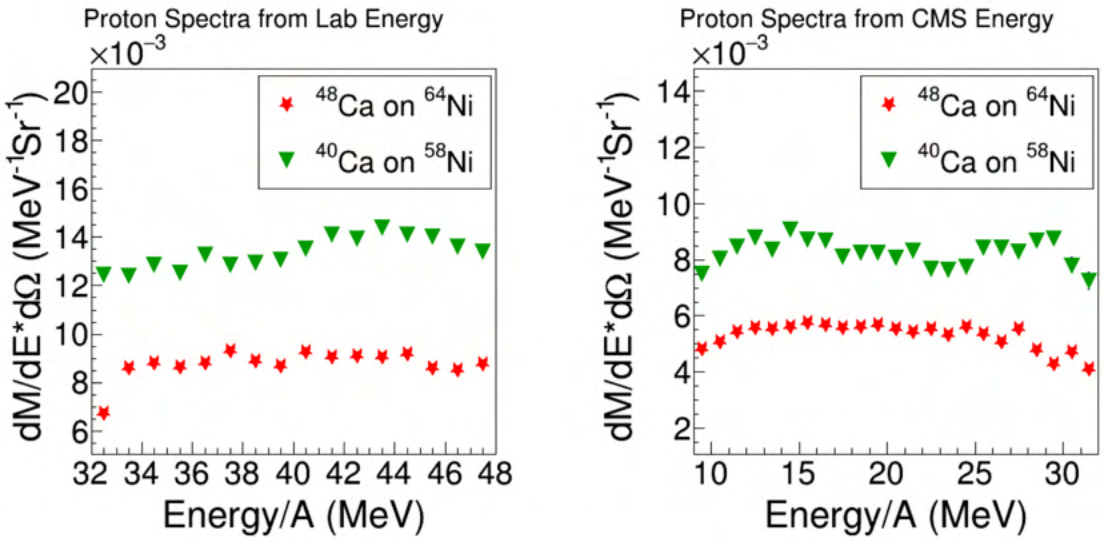

Figure 5.20: Proton spectra constructed in the lab and in the center of mass frames for ^{40}Ca on ^{58}Ni and ^{48}Ca on ^{64}Ni at 140 MeV/A. Only statistical errors are included in error bars.

the center of mass frame for the two systems. Figure 5.21 shows deuteron spectra.

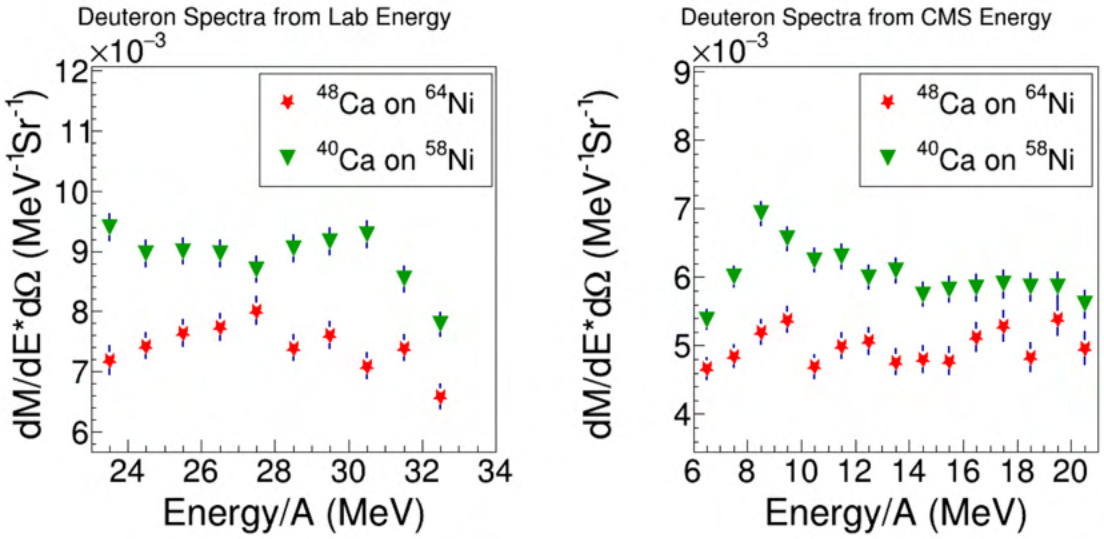

Figure 5.21: Deuteron spectra constructed in the lab and in the center of mass frames for ^{40}Ca on ^{58}Ni and ^{48}Ca on ^{64}Ni at 140 MeV/A. Only statistical errors are included in error bars.

We used the proton spectra, in the center of mass from neutron-rich ^{48}Ca on ^{64}Ni and proton-rich ^{40}Ca on ^{58}Ni systems at 140 MeV/A to construct the ratio of the Equation 5.6. This ratio is smaller than 1 because less protons are produced in n-rich collisions.

Its because more protons are used to construct the light clusters because of the increase in the number of neutrons. Results are shown in Figure 5.22. The isoscaling equation

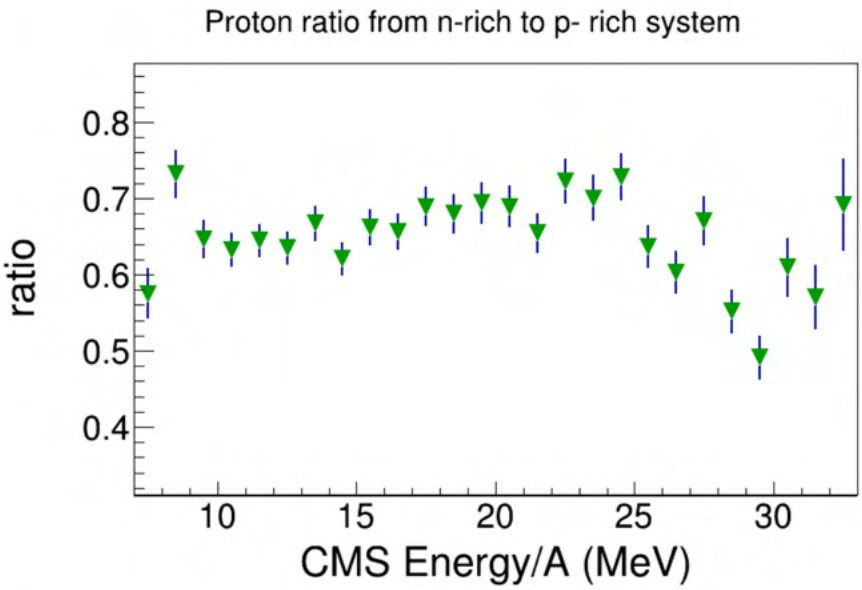

Figure 5.22: Ratio of protons from ^{48}Ca on ^{64}Ni and ^{40}Ca on ^{58}Ni systems at 140 MeV/A. Energy used here is the center of mass energy.

(Equation 2.7) describes the isotropic yields of the particles. Using the Equation 2.7 the yields of the neutrons and the charged particles are related as,

$$R_{21}(n) = C\exp(\alpha) \tag{5.5}$$

$$R_{21}(p) = C\exp(\beta) \tag{5.6}$$

$$R_{21}(d) = C\exp(\alpha+\beta) \tag{5.7}$$

$$R_{21}(t) = C\exp(2\alpha+\beta) \tag{5.8}$$

$$R_{21}(^3He) = C\exp(\alpha+2\beta) \tag{5.9}$$

where R is the yield, C is the normalizing constant and α, β are isoscaling parameters. If we assume that isoscaling works for our data, we can use these isocaling equations to construct the pseudo-neutrons, which are not real neutrons, then we can take those pseudo-neutrons to construct a double ratio of pseudo neutrons to protons. The ratio of

Equation 5.7 to the Equation 5.6 (deuteron to proton spectra) gives the ratio of pseudo neutrons. The Figure 5.23 shows a spectra of pseudo neutrons from ^{48}Ca on ^{64}Ni and ^{40}Ca on ^{58}Ni systems at 140 MeV/A. If the isoscaling works in our system the ratio for neutrons should agree with what we showed in the Figure 5.23. That comparison will help us understand the range of energies where isoscaling is a valid assumption of particle production.

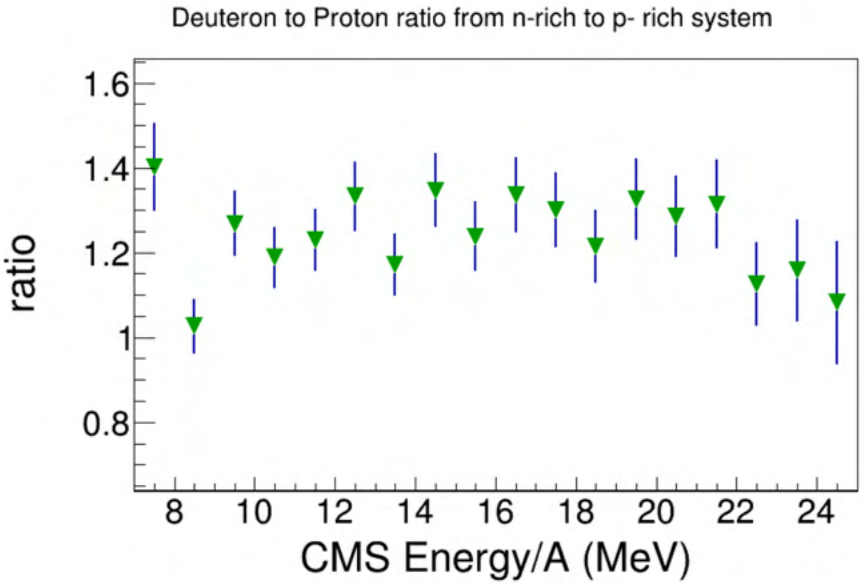

Figure 5.23: Construction of the pseudo neutrons from deuterons to protons ratio from ^{48}Ca on ^{64}Ni and ^{40}Ca on ^{58}Ni systems at 140 MeV/A

Chapter 6

Summary and Outlooks

The WMU Veto Wall was constructed and commissioned at Western Michigan University and used in experiment performed at the National Superconducting Cyclotron Laboratory. A radioactive gamma source ^{60}Co was used to test and calibrate the detectors. The position calibration was done by using the time difference between the signals received from the top and bottom PMTs as discussed in Section 4.3.2. Since a geometric mean of QDC signals from the top and the bottom PMTs depends on the position along the scintillator, the energy calibration is position dependent. For energy calibration we used the known value of energy deposited by the gammas from ^{60}Co (for example 1.04 MeV) and a pedestal from electronics (zero energy). The detailed procedure is discussed in Section 4.3.1.

The main purpose of the Veto Wall was to filter the charged particles from neutrons when used with the neutron detector LANA. Since neutrons do not interact with the Veto Wall alike charged particles, we can separate neutrons from the charged particles by gating on the multiplicity of the Veto Wall. A hit is considered in the Veto Wall if we get time signals, charge signals and the energy deposited in the Veto Wall is greater than a threshold value (0.67 MeVee). Charged particles must satisfy these conditions in order to be detected in the Veto Wall while neutrons will pass through the detector undetected. Neutrons are later separated from the gammas in LANA by using the pulse

shape discrimination. LANA scintillator produces prompt and delay fluorescence when attenuated by neutrons and gammas. The prompt decay produces the majority of light while delayed fluorescence depends on the type of particle causing it [104]. The variations in delayed fluorescence between the particles produce different time structure of the signals registered by the detector and it is utilized to separate neutrons from gammas which is called pulsed shaped discrimination. LANA efficiency corrections still have to be applied to the neutrons in order to obtained the calibrated neutron spectra.

Charged particles detected and identified by HiRA using Δ E vs E technique are subjected to efficiency correction to obtained the spectra. Protons and neutrons obtained from the experiment can be used to calculate a single ratio of neutrons to protons. Single ratios from neutron-rich systems and proton-rich systems are used to obtain a double ratio using Equation 2.6, that is sensitive to the symmetry energy. While waiting for the final neutron spectra, we can construct so-called pseudo-neutron spectra by relying on isoscaling of particles produced in heavy-ion collisions [105]. The ratio of pseudo-neutron is constructed by multiplying the ratio of t/^3He by the ratio of protons. Following equation show the construction of the ratio of pseudo-neutrons.

$$R_{21}(p) \cdot \frac{R_{21}(t)}{R_{21}(^3He)} = \exp(\alpha) = R(n) \tag{6.1}$$

which is analogous to Equation 5.5. Figure 6.1 shows preliminary results [106] from the collaboration which is a double ratio of pseudo-neutrons and protons as a function of the transverse momentum. The pseudo-neutron and proton ratio from neutron-rich (^{48}Ca on ^{64}Ni) and proton-rich (^{40}Ca on ^{58}Ni) systems were used. Pseudo-neutrons agree with real neutrons which was shown in [105]. In an absence of neutrons, the double ratio of pseudo-neutrons to protons along with results from theoretical model (Bayesian analysis was used in Figure 6.1) can be used to constraint the symmetry energy at higher densities. Parameters like offset S_0, slope L, scalar and vector masses m_s, m_v were varied within the ranges of (25,35), (30,120), (0.6, 1) and (0.6, 1.2) in the Bayesian posterior analysis and it was seen that m_s and m_v were strongly correlated. It provides a tight constraint

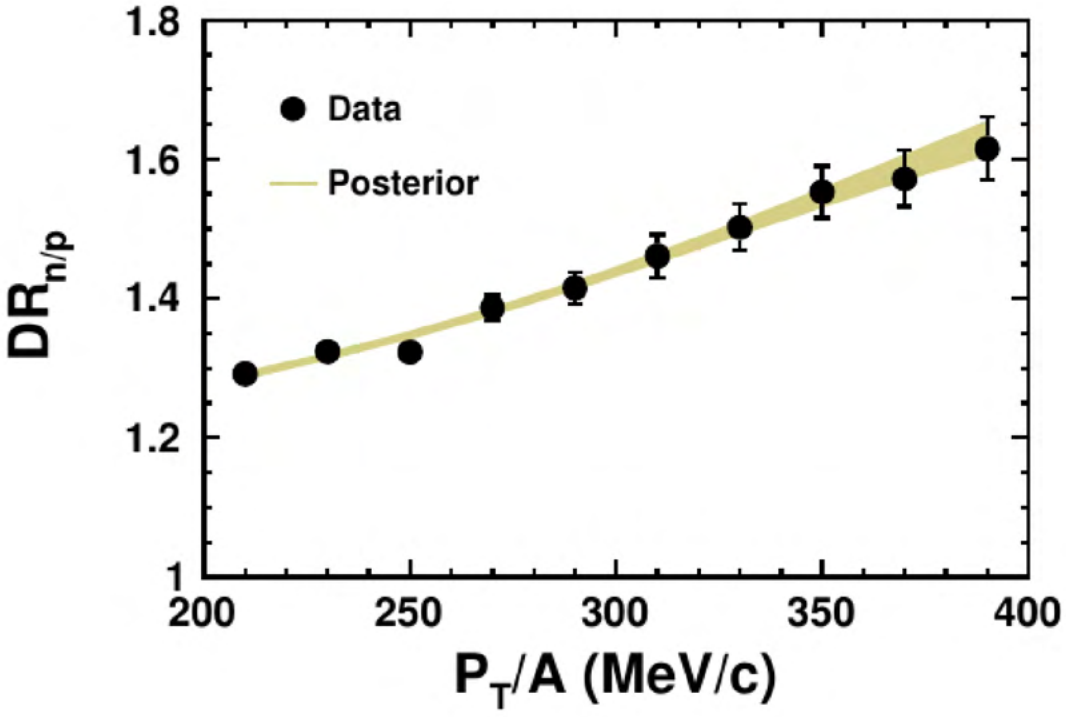

Figure 6.1: Double ratio of coalescence pseudo neutrons to protons from Ca +Ni systems. Black points are the data with error bars and the yellow band is the 1 σ confidence interval from the Bayesian posterior distribution

on the effective mass splitting which shows that data favors negative mass splitting with $\Delta m_p^* > \Delta m_n^*$ for asymmetry.

Beam of Calcium (40,48) isotopes at 56 MeV/u and 140 MeV/u and targets of Nickel(58,64) and Tin(112,124) were chosen in our experiment to access a larger range of nuclear densities than what was done previously. Moreover, the HiRA detector was upgraded to detect high energetic protons, deuterons and tritons. The Veto Wall was built using plastics scintillators to detect the charged particles precisely. These upgrades were meant to improved the proton and neutron spectra so that they can be used to constrain the symmetry energy at higher density. Neutron spectra analysis is ongoing while the charged particles spectra is almost final. We demonstrated that the performance of the Veto Wall is aiding in separating protons from neutrons. Once neutron analysis is done, protons and real neutron spectra can be used to construct a double ratio similar to that

shown in Figure 6.1. Theoretical calculations under similar conditions using transport models will be compared to the experimental neutrons to protons double ratio in order to constraint the density and the momentum dependence of the symmetry energy potential.

We used the Veto Wall to construct proton, deuteron and triton spectra that were stopped in the detector. We constructed the double ratio of pseudo neutrons and protons using the charged particles deposited in the detector. The HiRA and the LANA will be used to construct the double ratio of real neutrons (measured by the LANA) and protons (measured by the HiRA) that will be compared to theoretical models so that the mystery of the density and momentum dependence of the symmetry energy at higher densities can be unfold.

Bibliography

[1] Ganesan Srinivasan. The chandrasekhar limit. pages 79–94, 2014.

[2] Gordon Baym and Christopher Pethick. Physics of neutron stars. *Annual Review of Astronomy and Astrophysics*, 17(1):415–443, 1979.

[3] A. Hewish, S. J. Bell, J. D. H Pilkington, P. F. Scott, and R. A. Collins. Observation of a rapidly pulsating radio source. *Nature*, 217:709–713, 1968.

[4] Neutron star cross section. https://commons.wikimedia.org/wiki/File:Neutron_star_cross_section.svg. Accessed: 2022-04-15.

[5] The Editors of Encyclopaedia Britannica. nuclear model. *Encyclopedia Britannica*, Nov 2015.

[6] William D. Myers and Wladyslaw J. Swiatecki. Nuclear masses and deformations. *Nuclear Physics*, 81(1):1–60, 1966.

[7] Michael W. Kirson. Mutual influence of terms in a semi-empirical mass formula. *Nucl. Phys. A*, 798:29–60, 2008.

[8] Paweł Danielewicz. Surface symmetry energy. *Nuclear Physics A*, 727(3):233–268, 2003.

[9] C. J. Horowitz, E. F. Brown, Y. Kim, W. G. Lynch, R. Michaels, A. Ono, J. Piekarewicz, M. B. Tsang, and H. H. Wolter. A way forward in the study of the symmetry energy: experiment, theory, and observation. *J. Phys. G*, 41:093001, 2014.

[10] C. J. Horowitz and J. Piekarewicz. Neutron star structure and the neutron radius of ^{208}pb. *Phys. Rev. Lett.*, 86:5647–5650, Jun 2001.

[11] Micha A. Kilburn. *PROTON-PROTON CORRELATION FUNCTIONS AS A PROBE TO REACTION DYNAMICS.* PhD thesis, Michigan State University, 2011.

[12] J. Piekarewicz and M. Centelles. Incompressibility of neutron-rich matter. *Phys. Rev. C*, 79:054311, May 2009.

[13] C J Horowitz, E F Brown, Y Kim, W G Lynch, R Michaels, A Ono, J Piekarewicz, M B Tsang, and H H Wolter. A way forward in the study of the symmetry energy: experiment, theory, and observation. *Journal of Physics G: Nuclear and Particle Physics*, 41(9):093001, jul 2014.

[14] Bao-Jun Cai, Farrukh J. Fattoyev, Bao-An Li, and William G. Newton. Critical density and impact of $\Delta(1232)$ resonance formation in neutron stars. *Phys. Rev. C*, 92:015802, Jul 2015.

[15] J. M. Lattimer and M. Prakash. Neutron star structure and the equation of state. *Astrophys. J.*, 550:426, 2001.

[16] Alessandro Drago, Andrea Lavagno, Giuseppe Pagliara, and Daniele Pigato. Early appearance of Δ isobars in neutron stars. *Phys. Rev. C*, 90:065809, Dec 2014.

[17] Camille Ducoin, Jérôme Margueron, Constan ça Providência, and Isaac Vidaña. Core-crust transition in neutron stars: Predictivity of density developments. *Phys. Rev. C*, 83:045810, Apr 2011.

[18] James M. Lattimer and Madappa Prakash. The equation of state of hot, dense matter and neutron stars. *Physics Reports*, 621:127–164, 2016. Memorial Volume in Honor of Gerald E. Brown.

[19] K. Sumiyoshi, H. Suzuki, and H. Toki. Influence of the symmetry energy on the birth of neutron stars and supernova neutrinos. *Astron. Astrophys.*, 303:475, 1995.

[20] Tobias Fischer, Matthias Hempel, Irina Sagert, Yudai Suwa, and Jürgen Schaffner-Bielich. Symmetry energy impact in simulations of core-collapse supernovae. *Eur. Phys. J. A*, 50:46, 2014.

[21] N. Nikolov, N. Schunck, W. Nazarewicz, M. Bender, and J. Pei. Surface symmetry energy of nuclear energy density functionals. *Phys. Rev. C*, 83:034305, Mar 2011.

[22] Stephane Goriely, Andreas Bauswein, and H. Thomas Janka. R-Process Nucleosynthesis in Dynamically Ejected Matter of Neutron Star Mergers. *Astrophys. J. Lett.*, 738:L32, 2011.

[23] A. Bauswein, S. Goriely, and H. T. Janka. Systematics of dynamical mass ejection, nucleosynthesis, and radioactively powered electromagnetic signals from neutron-star mergers. *Astrophys. J.*, 773:78, 2013.

[24] Shinya Wanajo, Yuichiro Sekiguchi, Nobuya Nishimura, Kenta Kiuchi, Koutarou Kyutoku, and Masaru Shibata. Production of all the r-process nuclides in the dynamical ejecta of neutron star mergers. *Astrophys. J. Lett.*, 789:L39, 2014.

[25] Andrea Maselli, Leonardo Gualtieri, and Valeria Ferrari. Constraining the equation of state of nuclear matter with gravitational wave observations: Tidal deformability and tidal disruption. *Phys. Rev. D*, 88:104040, Nov 2013.

[26] A. Bauswein, N. Stergioulas, and H.-T. Janka. Revealing the high-density equation of state through binary neutron star mergers. *Phys. Rev. D*, 90:023002, Jul 2014.

[27] Paul D. Lasky, Brynmor Haskell, Vikram Ravi, Eric J. Howell, and David M. Coward. Nuclear equation of state from observations of short gamma-ray burst remnants. *Phys. Rev. D*, 89:047302, Feb 2014.

[28] Stephan Rosswog. The multi-messenger picture of compact binary mergers. *Int. J. Mod. Phys. D*, 24(05):1530012, 2015.

[29] B. P. Abbott et al. GW170817: Observation of Gravitational Waves from a Binary Neutron Star Inspiral. *Phys. Rev. Lett.*, 119(16):161101, 2017.

[30] Natsumi Ikeno, Akira Ono, Yasushi Nara, and Akira Ohnishi. Effects of Pauli blocking on pion production in central collisions of neutron-rich nuclei. *Phys. Rev. C*, 101(3):034607, 2020.

[31] Natsumi Ikeno, Akira Ono, Yasushi Nara, and Akira Ohnishi. Probing neutron-proton dynamics by pions. *Phys. Rev. C*, 93(4):044612, 2016. [Erratum: Phys.Rev.C 97, 069902 (2018)].

[32] Y. Nara, N. Otuka, A. Ohnishi, K. Niita, and S. Chiba. Study of relativistic nuclear collisions at AGS energies from p + Be to Au + Au with hadronic cascade model. *Phys. Rev. C*, 61:024901, 2000.

[33] Jun Su, Konstantin Cherevko, Wen-Jie Xie, and Feng-Shou Zhang. Non-isotropic and nonsingle explosion in central 129 Xe + 120 Sn collisions at 50–125 MeV/nucleon. *Phys. Rev. C*, 89(1):014619, 2014.

[34] Jun Su and Feng-Shou Zhang. Non-equilibrium and residual memory in momentum space of fragmenting sources in central heavy-ion collisions. *Phys. Rev. C*, 87(1):017602, 2013.

[35] Jun Su, Feng-Shou Zhang, and Bao-An Bian. Odd-even effect in heavy-ion collisions at intermediate energies. *Phys. Rev. C*, 83:014608, 2011.

[36] M. D. Cozma. The impact of energy conservation in transport models on the π^-/π^+ multiplicity ratio in heavy-ion collisions and the symmetry energy. *Phys. Lett. B*, 753:166–172, 2016.

[37] M. D. Cozma. Constraining the density dependence of the symmetry energy using the multiplicity and average p_T ratios of charged pions. *Phys. Rev. C*, 95(1):014601, 2017.

[38] Qingfeng Li, Caiwan Shen, Chenchen Guo, Yongjia Wang, Zhuxia Li, J. Lukasik, and W. Trautmann. Nonequilibrium dynamics in heavy-ion collisions at low energies available at the GSI Schwerionen Synchrotron. *Phys. Rev. C*, 83:044617, 2011.

[39] S. A. Bass et al. Microscopic models for ultrarelativistic heavy ion collisions. *Prog. Part. Nucl. Phys.*, 41:255–369, 1998.

[40] Pawel Danielewicz. Determination of the mean field momentum dependence using elliptic flow. *Nucl. Phys. A*, 673:375–410, 2000.

[41] Jun Hong and P. Danielewicz. Subthreshold pion production within a transport description of central Au + Au collisions. *Phys. Rev. C*, 90(2):024605, 2014.

[42] J. Weil et al. Particle production and equilibrium properties within a new hadron transport approach for heavy-ion collisions. *Phys. Rev. C*, 94(5):054905, 2016.

[43] Zhen Zhang and Che Ming Ko. Pion production in a transport model based on mean fields from chiral effective field theory. *Phys. Rev. C*, 98(5):054614, 2018.

[44] Akira Ono et al. Comparison of heavy-ion transport simulations: Collision integral with pions and Δ resonances in a box. *Phys. Rev. C*, 100(4):044617, 2019.

[45] Jun Xu et al. Understanding transport simulations of heavy-ion collisions at 100A and 400A MeV: Comparison of heavy-ion transport codes under controlled conditions. *Phys. Rev. C*, 93(4):044609, 2016.

[46] Ying-Xun Zhang et al. Comparison of heavy-ion transport simulations: Collision integral in a box. *Phys. Rev. C*, 97(3):034625, 2018.

[47] D. D. S. Coupland, W. G. Lynch, M. B. Tsang, P. Danielewicz, and Yingxun Zhang. Influence of transport variables on isospin transport ratios. *Phys. Rev. C*, 84:054603, Nov 2011.

[48] Akira Ono. Cluster correlations in multifragmentation. *Journal of Physics: Conference Series*, 420:012103, mar 2013.

[49] Akira Ono. Nuclear matter properties in fragmentation reactions. *Journal of Physics: Conference Series*, 436:012068, apr 2013.

[50] Yoshiko Kanada-En'yo, Masaaki Kimura, and Akira Ono. Antisymmetrized molecular dynamics and its applications to cluster phenomena. *Progress of Theoretical and Experimental Physics*, 2012(1), 08 2012. 01A202.

[51] K. A. Brueckner. Two-Body Forces and Nuclear Saturation. 3. Details of the Structure of the Nucleus. *Phys. Rev.*, 97:1353–1366, 1955.

[52] J. Estee et al. Probing the Symmetry Energy with the Spectral Pion Ratio. *Phys. Rev. Lett.*, 126(16):162701, 2021.

[53] J. Barney et al. The SπRIT time projection chamber. *Rev. Sci. Instrum.*, 92(6):063302, 2021.

[54] Bao-An Li, C. M. Ko, and Zhongzhou Ren. Equation of state of asymmetric nuclear matter and collisions of neutron-rich nuclei. *Phys. Rev. Lett.*, 78:1644–1647, Mar 1997.

[55] D. D. S. Coupland, M. Youngs, Z. Chajecki, W. G. Lynch, M. B. Tsang, Y. X. Zhang, M. A. Famiano, T. K. Ghosh, B. Giacherio, M. A. Kilburn, Jenny Lee, H. Liu, F. Lu, P. Morfouace, P. Russotto, A. Sanetullaev, R. H. Showalter, G. Verde, and J. Winkelbauer. Probing effective nucleon masses with heavy-ion collisions. *Phys. Rev. C*, 94:011601, Jul 2016.

[56] B. Alex Brown. Neutron radii in nuclei and the neutron equation of state. *Phys. Rev. Lett.*, 85:5296–5299, Dec 2000.

[57] M.B. Tsang, Z. Chajecki, D. Coupland, P. Danielewicz, F. Famiano, R. Hodges, M. Kilburn, F. Lu, W.G. Lynch, J. Winkelbauer, M. Youngs, and Y.X. Zhang. Constraints on the density dependence of the symmetry energy from heavy-ion collisions. *Progress in Particle and Nuclear Physics*, 66(2):400–404, 2011. Particle and Nuclear Astrophysics.

[58] P. Morfouace, C.Y. Tsang, Y. Zhang, W.G. Lynch, M.B. Tsang, D.D.S. Coupland, M. Youngs, Z. Chajecki, M.A. Famiano, T.K. Ghosh, G. Jhang, Jenny Lee, H. Liu, A. Sanetullaev, R. Showalter, and J. Winkelbauer. Constraining the symmetry energy with heavy-ion collisions and bayesian analyses. *Physics Letters B*, 799:135045, 2019.

[59] M. Di Toro, V. Baran, M. Colonna, and V. Greco. Probing the Nuclear Symmetry Energy with Heavy Ion Collisions. *J. Phys. G*, 37:083101, 2010.

[60] L. Shi and P. Danielewicz. Nuclear isospin diffusivity. *Phys. Rev. C*, 68:064604, Dec 2003.

[61] H. S. Xu, M. B. Tsang, T. X. Liu, X. D. Liu, W. G. Lynch, W. P. Tan, A. Vander Molen, G. Verde, A. Wagner, H. F. Xi, C. K. Gelbke, L. Beaulieu, B. Davin, Y. Larochelle, T. Lefort, R. T. de Souza, R. Yanez, V. E. Viola, R. J. Charity, and L. G. Sobotka. Isospin fractionation in nuclear multifragmentation. *Phys. Rev. Lett.*, 85:716–719, Jul 2000.

[62] L. Phair et al. Impact parameter filters for Ar-36 + Au-197 collisions at E / A = 50, 80, and 110 MeV. *Nucl. Phys. A*, 548:489–509, 1992.

[63] M. B. Tsang, W. A. Friedman, C. K. Gelbke, W. G. Lynch, G. Verde, and H. Xu. Isotopic scaling in nuclear reactions. *Phys. Rev. Lett.*, 86:5023–5026, 2001.

[64] M. B. Tsang et al. Isospin Diffusion and the Nuclear Symmetry Energy in Heavy Ion Reactions. *Phys. Rev. Lett.*, 92:062701, 2004.

[65] F. Rami et al. Isospin tracing: A Probe of nonequilibrium in central heavy ion collisions. *Phys. Rev. Lett.*, 84:1120–1123, 2000.

[66] Jean-Yves Ollitrault. Anisotropy as a signature of transverse collective flow. *Phys. Rev. D*, 46:229–245, Jul 1992.

[67] Xiao-Hua Fan, Gao-Chan Yong, and Wei Zuo. Probing the density dependence of the symmetry energy by nucleon flow. *Phys. Rev. C*, 97(3):034604, 2018.

[68] Experiment05049. https://groups.nscl.msu.edu/hira/05049/index.htm. Accessed: 2022-4-22.

[69] Z. Chajecki et al. in preparation.

[70] Experiment16042. https://groups.nscl.msu.edu/hira/16042/index.htm. Accessed: 2022-4-22.

[71] D.G. Sarantites, P.-F. Hua, M. Devlin, L.G. Sobotka, J. Elson, J.T. Hood, D.R. LaFosse, J.E. Sarantites, and M.R. Maier. "the microball" design, instrumentation and response characteristics of a 4-multidetector exit channel-selection device for spectroscopic and reaction mechanism studies with gammasphere. *Nuclear Instruments and Methods in Physics Research Section A: Accelerators, Spectrometers, Detectors and Associated Equipment*, 381(2):418–432, 1996.

[72] Kuan Zhu. *Measuring Neutrons in Heavy Ion Collisions.* PhD thesis, Michigan State University, 2020.

[73] M.S. Wallace, M.A. Famiano, M.-J. van Goethem, A.M. Rogers, W.G. Lynch, J. Clifford, F. Delaunay, J. Lee, S. Labostov, M. Mocko, L. Morris, A. Moroni, B.E. Nett, D.J. Oostdyk, R. Krishnasamy, M.B. Tsang, R.T. de Souza, S. Hudan, L.G. Sobotka, R.J. Charity, J. Elson, and G.L. Engel. The high resolution array

(hira) for rare isotope beam experiments. *Nuclear Instruments and Methods in Physics Research Section A: Accelerators, Spectrometers, Detectors and Associated Equipment*, 583(2):302–312, 2007.

[74] Sean Robert Sweany. *CONSTRAINING THE PROTON/NEUTRON EFFECTIVE MASS SPLITTING THROUGH HEAVY ION COLLISIONS*. PhD thesis, Michigan State University, 2020.

[75] D. Dell'Aquila et al. Non-linearity effects on the light-output calibration of light charged particles in CsI(Tl) scintillator crystals. *Nucl. Instrum. Meth. A*, 929:162–172, 2019.

[76] Experiment09042. https://groups.nscl.msu.edu/hira/09042/index.htm. Accessed: 2022-4-22.

[77] Micheal D. Youngs. *USING LIGHT EMITTED CLUSTERS AS A PROBE OF THE SYMMETRY ENERGY IN THE NUCLEAR EQUATION OF STATE*. PhD thesis, Michigan State University, 2013.

[78] P.D Zecher, A Galonsky, J.J Kruse, S.J Gaff, J Ottarson, J Wang, F Deák, Á Horváth, Á Kiss, Z Seres, K Ieki, Y Iwata, and H Schelin. A large-area, position-sensitive neutron detector with neutron/-ray discrimination capabilities. *Nuclear Instruments and Methods in Physics Research Section A: Accelerators, Spectrometers, Detectors and Associated Equipment*, 401(2):329–344, 1997.

[79] F. C. E. Teh et al. Value-Assigned Pulse Shape Discrimination for Neutron Detectors. *IEEE Trans. Nucl. Sci.*, 68(8):2294–2300, 2021.

[80] J. Scherzinger et al. The light-yield response of a NE-213 liquid-scintillator detector measured using 2–6 MeV tagged neutrons. *Nucl. Instrum. Meth. A*, 840:121–127, 2016.

[81] Rachel Hodges Showalter. *DETERMINATION OF DENSITY AND MOMENTUM DEPENDENCE OF NUCLEAR SYMMETRY POTENTIALS WITH ASYMMETRIC HEAVY ION REACTIONS*. PhD thesis, Michigan State University, 2015.

[82] Daniel David Schechtman Coupland. *PROBING THE NUCLEAR SYMMETRY ENERGY WITH HEAVY ION COLLISIONS*. PhD thesis, Michigan State University, 2013.

[83] A. Artikov, J. Budagov, I. Chirikov-Zorin, D. Chokheli, M. Lyablin, G. Bellettini, A. Menzione, S. Tokar, N. Giokaris, and A. Manousakis-Katsikakis. Properties of the Ukrainian polystyrene-based plastic scintillator UPS 923A. *Nucl. Instrum. Meth. A*, 555:125–131, 2005.

[84] S. Ashrafi and M. Ghahremani Gol. Energy calibration of thin plastic scintillators using compton scattered -rays. *Nuclear Instruments and Methods in Physics Research Section A: Accelerators, Spectrometers, Detectors and Associated Equipment*, 642(1):70–74, 2011.

[85] A.H. Tkaczyk, H. Saare, C. Ipbüker, F. Schulte, P. Mastinu, J. Paepen, B. Pedersen, P. Schillebeeckx, and G. Varasano. Characterization of ej-200 plastic scintillators as active background shield for cosmogenic radiation. *Nuclear Instruments and Methods in Physics Research Section A: Accelerators, Spectrometers, Detectors and Associated Equipment*, 882:96–104, 2018.

[86] Response of ej-200 plastic scintillator. https://eljentechnology.com/images/technical_library/EJ200_Resp.pdf. Accessed: 2022-4-22.

[87] Characteristics of eljen pvt based scintillator material. https://eljentechnology.com/images/technical_library/Structural_Properties_of_EJ-200.pdf. Accessed: 2022-4-22.

[88] Physical constants of plastic scintillators. https://eljentechnology.

com/images/technical_library/Physical_Constants_Plastic.pdf. Accessed: 2022-4-22.

[89] Ej-200 gamma attenuation coefficients. https://eljentechnology.com/images/technical_library/EJ200_Gamma_Coeff.pdf. Accessed: 2022-4-22.

[90] Light collection in plastic scintillator. https://eljentechnology.com/images/technical_library/Light_Collection_in_Plastic_Scintillator.pdf. Accessed: 2022-4-22.

[91] Photomultiplier tubes and assemblies. https://www.hamamatsu.com/content/dam/hamamatsu-photonics/sites/documents/99_SALES_LIBRARY/etd/High_energy_PMT_TPMZ0003E.pdf. Accessed: 2022-4-22.

[92] Operation manual. http://ikpe1101.ikp.kfa-juelich.de/manuals/LeCroy_1440/operation_manual/operation_manual.htm. Accessed: 2022-4-22.

[93] A. Belloni. Radiation effects on plastic scintillators for current and future hep experiments. https://indico.fnal.gov/event/18739/contributions/48811/attachments/30467/37475/181120_fnalrts.pdf, 2018.

[94] General purpose ej-200, ej-204, ej-208, ej-212. https://eljentechnology.com/products/plastic-scintillators/ej-200-ej-204-ej-208-ej-212. Accessed: 2022-06-01.

[95] 32 channel multievent qdc. https://www.caen.it/products/v792/. Accessed: 2022-5-15.

[96] Tdcs models. https://www.caen.it/subfamilies/tdcs/. Accessed: 2022-5-15.

[97] E.R. Siciliano, J.H. Ely, R.T. Kouzes, J.E. Schweppe, D.M. Strachan, and S.T. Yokuda. Energy calibration of gamma spectra in plastic scintillators using compton kinematics. *Nuclear Instruments and Methods in Physics Research Section A:*

Accelerators, Spectrometers, Detectors and Associated Equipment, 594(2):232–243, 2008.

[98] K. Sümmerer, W. Brüchle, D. J. Morrissey, M. Schädel, B. Szweryn, and Yang Weifan. Target fragmentation of au and th by 2.6 gev protons. *Phys. Rev. C*, 42:2546–2561, Dec 1990.

[99] J.P. Dufour, R. Del Moral, H. Emmermann, F. Hubert, D. Jean, C. Poinot, M.S. Pravikoff, A. Fleury, H. Delagrange, and K.-H. Schmidt. Projectile fragments isotopic separation: Application to the lise spectrometer at ganil. *Nuclear Instruments and Methods in Physics Research Section A: Accelerators, Spectrometers, Detectors and Associated Equipment*, 248(2):267–281, 1986.

[100] F. Hubert, R. Bimbot, and H. Gauvin. Range and stopping-power tables for 2.5–500 MeV/nucleon heavy ions in solids. *Atom. Data Nucl. Data Tabl.*, 46:1–213, 1990.

[101] L.C. Northcliffe and R.F. Schilling. Range and stopping-power tables for heavy ions. *Atomic Data and Nuclear Data Tables*, 7(3):233–463, 1970.

[102] D. Bazin, O. Tarasov, M. Lewitowicz, and O. Sorlin. The Program LISE: A Simulation of fragment separators. 2 2001.

[103] M.P. Kuchera, O.B. Tarasov, D. Bazin, B.M. Sherrill, and K.V. Tarasova. Plans for performance and model improvements in the lise++ software. *Nuclear Instruments and Methods in Physics Research Section B: Beam Interactions with Materials and Atoms*, 376:168–170, 2016. Proceedings of the XVIIth International Conference on Electromagnetic Isotope Separators and Related Topics (EMIS2015), Grand Rapids, MI, U.S.A., 11-15 May 2015.

[104] Glenn F Knoll. *Radiation detection and measurement*. John Wiley & Sons, 2010.

[105] Z. Chajecki et al. Scaling properties of light-cluster production. 2 2014.

[106] Private communication.